2018

Out-of-Field Dose to the Eye Lens and Cardiac Implantable Electronic Devices (CIEDs) during VMAT of the prostate

Tina C. Baradaran
University of Wollongong

Out-of-Field Dose to the Eye Lens and Cardiac Implantable Electronic Devices (CIEDs) during VMAT of the prostate

A thesis submitted in fulfilment of the
requirements for the award of the degree

Masters of Philosophy

from

UNIVERSITY OF WOLLONGONG

by

Tina C Baradaran
Bachelor of Medical and Radiation Physics
University of Wollongong, 2015

SCHOOL OF PHYSICS
2018

Abstract

Volumetric Modulated Arc Therapy (VMAT) is a new type of Intensity Modulated Radiation Therapy (IMRT) technique as it can deliver a more accurate shape of sculpted 3D dose distribution to the targeted tumour volume in a single 360° gantry rotation or multiple sub-arcs. This improvement, however, has not mitigated the problem of doses to normal tissues outside the treated volume. The out-of-field dose associated risks remains high clinical and scientific interests for investigations. A re-evaluation of the eye lens radio-sensitivity by the ICRP 2011 has resulted in a significant reduction of the threshold for lens opacities from 8 Gy to 0.5 Gy [1]. The objective of this thesis study is to investigate the out-of-field doses to critical structures such as eye lens and CIEDs (cardiac implantable electronic devices) such as pacemakers and ICDs during 6 MV VMAT treatment of the prostate.

In order to provide an accurate estimation of the out-of-field dose to the eye lens and CIEDs, the out-of-field dose distribution for a Varian iX 6 MV VMAT at St George Cancer Care Centre was extensively measured and examined while the individual out-of-field dose components (patient scatter, collimator scatter and head leakage) were carefully characterised as well. The out-of-field dose profiles with different field sizes and collimator angles were measured at depths of 5 mm, 15 mm and 37.5 mm, using an ionisation chamber within a motorised water tank, and compared with the previous studies in IMRT. The depth-dose measurements were made with a Roos parallel plate

chamber in solid water at distances of 52 cm and 76 cm from central axis. The dose to the eye lens and upper chest (typical location of a CIED) from clinical 6 MV VMAT treatment of the prostate were measured on an anthropomorphic phantom with a cylindrical chamber placed at a depth of 3 mm. This depth was chosen to match the depth of the most radio-sensitive region of the eye lens, which is at a depth of 2-4 mm [2] and a typical depth of the anterior surface of a CIED.

Our experimental results showed that at distances close to the field edge phantom scatter was a dominant source of out-of-field dose, while at distances greater than 20 cm head leakage was the dominant source of out-of-field dose. This result was seen across all the examined cases for different field sizes, collimator angles and depths of measurement.

Furthermore, using clinical prostate patient VMAT plans the maximum dose received by the eye lens was found to be 10.8 ± 0.3 cGy, and the maximum dose received to the chest was found to be 12.3 ± 0.4 cGy for the whole treatment. As expected, the doses to the eye lens and CIEDs are well below the recommended threshold doses of 50 cGy for the eye lens [1] and 200 cGy for limits of CIEDs [3]. These indicate that the VMAT patients receiving prostate treatment will not be at risk of cataracts or CIED failure as the out-of-field dose is minimal.

However, this work has shown that doses may be higher than predicted by most planning systems as they do not accurately model photon or electron leakage/scatter from the LINAC head.

This thesis is dedicated to my late grandmother.

Statement of Originality

This is to certify that the work described in this thesis is entirely my own, except where due reference is made in the text.

No work in this thesis has been submitted for a degree to any other university or institution.

Signed

Tina C Baradaran
September 5, 2018

Acknowledgments

It would not have been possible to write this thesis without the help and support of certain people, which I would like to mention here.

First and foremost I would like to thank my grandmother, for her unconditional love, for her wisdom and teaching me strength, in order to fulfill my goals. Thank you for being the light of my life.

To my mother, thank you for providing me with unfailing support and continuous encouragement throughout my years of undergraduate and postgraduate study and throughout the entire process of my life. For being there whenever I needed it, for supporting me financially and for always having confidence in me throughout my education. I greatly appreciate everything you have done

To my family, thank you for keeping me harmonious throughout my years of study at the University of Wollongong.

To my supervisors, Anna Ralston, Dr.Dean Cutajar, and Dr.Yujin Qi, thank you for your valuable time spent answering my questions, doing experiments and reading my thesis.

I would like to express my deep gratitude and thanks to my supervisor, Anna Ralston for imparting her knowledge and expertise and teaching me so many skills that will be of benefit to me in the field of Medical Physics.

I would also like to thank my supervisors, Dr. Dean Cutajar and Dr. Yujin Qi for your guidance and for steering me in the right direction whenever I needed it. Your guidance and supervision are much appreciated.

To the staff at SGCCC, thank you for making my time at St George Cancer Care Centre a memorable and great one.

I would also like to acknowledge Professor Anatoly Rozenfeld. His encouragement and support for the students of the Centre for Medical Radiation Physics (CMRP) to carry out projects and be able to contribute to the world of medical physics.

Contents

List of Figures

List of Tables

List of Abbreviations

3DCRT	Three-Dimensional Conformal Radiation Therapy
AAPM	American Association of Physicists in Medicine
CIED	Cardiac Implantable Electronic Device
EBRT	External Beam Radiation Therapy
FSD	Focus to Source Distance
ICD	Implantable Cardiac Defibrillator
ICRP	International Commission on Radiological Protection
IMRT	Intensity Modulated Radiation Therapy
MLC	Multi-Leaf Collimator
MU	Monitor Unit
OAR	Organ at Risk
PDD	Percentage Depth Dose
PTV	Planning Target Volume
SSD	Source-to-Surface Distance
VMAT	Volumetric Modulated Arc Therapy

Chapter 1

Introduction

Cancer is defined as the uncontrolled malignant growth of a group of cells caused by a series of changes in the genome. This disease is one of the leading cause of deaths in Australia. In 2014, cancer was the second most common cause of death in Australia, accounting for approximately 3 of every 10 deaths [4]. In 2013, there were 44,108 deaths from cancer in Australia of these deaths, 24,972 were male and 19,136 female [5]. This placed cancer fourth to the leading rates of mortality amongst patients in Australia. Globally, more than one in three people will develop cancer during their lifetime and about one in four will die from the disease [6].

According to the Australian Institute of Health and Welfare (AIHW), cancer mortality amongst the Australian population is decreasing, however, cancer incidence rates are steadily increasing. The report, Cancer mortality trends and projections: 2014-2025 [7] showed that in 2012, a total of 122,093 new cases of cancer were diagnosed in Australia, at a rate of 485 new cancer cases per 100,000 persons. A recent report by AIHW, Cancer in Australia 2017 [5] stated that the number of new cases expected to be diagnosed in 2017 is estimated to be 134,000 (excluding basal and squamous cell carcinoma of the skin, as these cancers are not notifiable diseases and hence are not reported to cancer

registries). This increasing trend is attributed to Australias aging population, improved diagnostic technology in the ability to diagnose smaller volume tumours and increased public awareness of cancer prevalence. A combination of these has led to more patients presenting for diagnosis. The report predicted that this number is estimated to increase with age, with additional diagnoses per year.

Prostate cancer is the most commonly diagnosed cancer in males in Australia and the third most common cause of cancer death. It is more common in older men, with 63% of cases diagnosed in men over 65 years of age [8]. In 2013, 19,233 new cases of prostate cancer were diagnosed in Australia. This represented 30% of all cancers diagnosed in Australian men. The risk of being diagnosed with prostate cancer by the age of 85 is 1 in 5 men [8]. In 2013, there were 3,112 deaths caused by prostate cancer, accounting for 13% of all cancer deaths in Australian men [8].

Treatment options for prostate cancer include surgery, chemotherapy, hormone therapy, radiation therapy, or a combination of these. Radiation therapy includes options such as high or low dose rate (HDR or LDR) brachytherapy, or external beam options such as 3D conformal radiation therapy (3DCRT), intensity modulated radiation therapy (IMRT), volumetric modulated arc therapy (VMAT) and Helical TomoTherapy® techniques. The types of radiation therapy of concern in this study is external beam radiation therapy.

The principle goal of radiation therapy is to maximise the dose delivered to a well-defined treatment volume, while minimising the dose to surrounding healthy tissues and organs, with the aim of eradicating the disease, prolonging the life and/or improvement of the quality of life of the patient. However, external beam radiation therapy also brings an unavoidable out-of-field dose to the patient. Although it may be relatively small, it

could cause a significant radiobiological effect to the critical organs/tissues such as the eye lens and heart outside the treatment site. Arising from the components within the accelerator, head leakage and collimator scatter are predominantly the main sources of external radiation which result in the out-of-field dose deposition in the patient. It is of great importance to accurately predict and estimate the out-of-field doses for the treatment planning.

Intensity Modulated Radiation Therapy (IMRT) and Volumetric Modulated Arc Therapy (VMAT) have become extremely popular in radiotherapy. This popularity has generated the attention to determine the out-of-field radiation dose as opposed to conventional therapy, since the dose has significantly been amplified due to the increased number of monitor units needed for IMRT and VMAT treatments.

From the epidemiological studies on Chernobyl clean-up workers, interventional radiology and cardiology physicians and bomb survivors eye lens doses have received a lot of attention as some showed that the threshold dose for cataract induction could be lower than the assumed value of 8 Gy. This resulted in the need for a detailed re-evaluation of the eye lens radio-sensitivity and an associated reliable dose assessment. For this reason, the International Commission on Radiological Protection ICRP 2011 [1] reviewed epidemiological evidence for the late effects of radiation induced damage. The ICRP 2011 then issued a Statement on Tissue Reaction containing a series of recommendations including a revision of the eye lens limit that lowers the threshold for eye lens opacities from the previous 8 Gy to 0.5 Gy [1].

EviQ Cancer Treatments Online [3] have also made their own recommendations on action thresholds for Cardiac Implantable Electronic Devices (CIEDs). Their recommendation includes a revision of the CIED limit which suggests that the risk of device

failure is low if the total dose to the device is less than 2 Gy and it may be appropriate to accept a total dose of 2-10 Gy to the device. There is a significant risk that CIEDs malfunction due to neutrons generated by x-ray beams of energies 10 MV or greater. Therefore, if the device is likely to receive a dose of $>$10 Gy then the risk of failure is significant and replanning of the treatment should be performed to reduce the dose to the CIED [3].

To develop an accurate and comprehensive out-of-field risk model for cancer patients, there are many challenges involved. Currently there are a few options available to determine the out-of-field dose which includes measuring the dose to the patient. These measurements are time consuming and yield only the dose to the specific measured points. They are specific to the particular treatment and patient examined. Most treatment planning systems do not accurately model photon or electron leakage/scatter from the LINAC head. Alternatively, estimates of the dose have been made by the AAPM Task Group 36 report on fetal doses [9]. The estimates are unfortunately associated with large uncertainties. Thus, a more thorough study is needed to establish the out-of-field dose from radiotherapy treatments. This study aims to develop a better understanding of components of out-of-field dose and make an accurate determination of the doses to the sensitive cells of the eye lens and for patients with CIEDs (including pacemakers and ICDs), for patients undergoing VMAT of the prostate.

1.1 Research Scope and Aims of this Thesis

The research scope of this project addresses the underestimation of the treatment planning systems in determining out-of-field dose. The aims of this thesis are divided into the following objectives:

- Develop a better understanding of the contributing factors that result in dose to the eye lens and chest region (for patients with CIEDs) during prostate treatment.

- Develop a method of measuring the individual out-of-field dose components (patient scatter, collimator scatter and head leakage) in a phantom.

- Make an evaluation of the doses to the eye lens and chest region (for patients with CIEDs) for patients undergoing VMAT of the prostate at St George Hospital and determine if these doses are within the ICRP and EviQ limits.

1.2 Thesis Structure

This thesis consists of 7 chapters that will endeavour to accomplish the aforementioned project aims and the specific objectives.

Following this introduction, Chapter 2 aims to provide a background into the out-of-field dose in External Beam Radiotherapy, specifically for the treatment of prostate cancer. It focuses on the importance of minimising the out-of-field dose to the sensitive cells of the eye lens and CIEDs in the chest region and reviews past approaches to measuring out-of-field dose found in the literature for different treatment options.

Chapter 3 begins by distinguishing the experimental principles associated with the use of ionisation chambers in measurements. A detailed uncertainty analysis is completed to account for the type A and type B uncertainties in the upcoming experiments.

Chapter 4 investigates the depth-dose measurements of out-of-field dose measured with a Roos chamber. It begins by examining the quantification of the couch scatter and looks at increasing the depth of measurement for different field sizes.

Chapter 5 outlines the characterisation of the out-of-field dose components and looks at the relative contributions of each of the sources. It begins by dose profile measurements and continues with depth-dose measurements at different combinations of collimator angle, field size and depth inside a PTW motorised water tank.

Chapter 6 reveals out-of-field doses for clinical VMAT treatments in patients undergoing VMAT of the prostate. A method of calculating the dose given to patients who undergo treatment was established for measuring the dose to the sensitive region of the eye lens and CIEDs on the chest.

Chapter 7 concludes this thesis by providing a summary of the overall outcomes and provides recommendations for future research in out-of-field dose.

Chapter 2

Literature Review

This chapter aims to provide a background into the out-of-field dose for External Beam Radiotherapy, specifically for the treatment of prostate cancer. It starts with an overview of the common treatment options available for prostate therapy. It then examines the major sources of out-of-field dose and the importance of minimising this dose to the sensitive cells of the eye lens and to the chest for patients with CIEDs (including pacemakers and ICDs). Moreover, it reviews the current and past proposed approaches to measuring out-of-field dose found in the literature for different treatment options.

2.1 Prostate Cancer and Treatment Options

The prostate gland is an organ that is made up of glandular, fibrous, and muscular elements, and is an important part of the male reproductive system. Located immediately below the bladder, the prostate is situated in front of the bowel, encapsulating the urethra. Its foremost function is to secrete fluids that protect and augment sperm. A healthy prostate is approximately the dimensions of a walnut.

Prostate cancer is a disease where the cells in the prostate gland become abnormal and grow uncontrollably to form tumours. Cancerous cells in the prostate are not lethal on their own, however, they are capable of metastasising; spreading to other parts of the body via the blood or lymph system creating new tumours. Benign tumours do not spread, although they may interfere with adjoining organs and constituents, causing problems or discomfort. The causes of prostate cancer are not clearly known, however it is known that age is an important factor. It is estimated that by the age of 85, 1 in 5 Australian males will be diagnosed with prostate cancer.

Patients with localised prostate cancer have the following options for management, depending on the severity of their case. For low severity patients, no initial treatment can be recommended with active surveillance typically performed by a general practitioner (GP). Patients with carcinoma of the prostate can be given the option of the surgical removal of the entire prostate, better known as radical prostatectomy (nerve-sparing surgical procedure). In general, surgery is an option if the tumour is confined to the prostate gland with no extension through the capsule or into the seminal vesicles.

Patients may also be administered chemotherapy for the systemic treatment of cancer. It can be delivered via injection (intravenous, intra-arterial or intrathecal), orally, or for some types of cancer, by cavity insertion. Hormone therapy (androgen deprivation therapy) is another treatment option which involves the use of hormones such as leutinising hormone-releasing agonist or antagonist to reduce the production of testosterone. It is rarely used as a monotherapy for prostate cancer due to its ineffectiveness on its own, but rather as an adjuvant therapy to radical prostatectomy or radiation therapy, to shrink the target.

Another modality recommended for the treatment of prostate cancer is radiation ther-

apy. Radiation therapy of the prostate includes options such as high or low dose rate (HDR or LDR) brachytherapy which can be delivered internally, or external beam (EBRT) options such as 3D conformal radiation therapy (3DCRT), intensity modulated radiation therapy (IMRT), volumetric modulated arc therapy (VMAT) and Helical TomoTherapy®. The selection of a particular procedure or a combination of procedures depends on the established prognostic factors such as stage, grade and pre-treatment prostate specific antigen (PSA) concentration, as well as the availability of such treatments.There is no single effective treatment of prostate cancer as the best treatment option is often highly patient specific.

2.2 Brachytherapy

Brachytherapy to the prostate is an invasive procedure involving sealed radioactive sources being inserted inside or adjacent to the region requiring treatment. This type of radiation aims to achieve highly localised dose distributions to spare normal tissue whilst treating the tumour. With this mode of therapy, a high radiation dose can be delivered locally to the tumour with a rapid dose fall-off in the surrounding normal tissue. Prostate brachytherapy is an interstitial form of therapy. Brachytherapy radiation sources are introduced via catheters, needles or applicators placed within the treatment region. Brachytherapy implants are used for early stage cancers, either alone or in conjunction with external beam radiation therapy.

2.3 External Beam Radiation Therapy

EBRT is a non-invasive treatment that uses high energy x-rays (usually 6-18 MV) to deliver dose to the patient, most commonly with a linear accelerator. Previously, a four-field box technique was used to deliver treatment to the prostate, seminal vesicles and lymph nodes, with generally 45 Gy prescribed to the whole treatment field, and the prostate itself boosted to 70 Gy or more. Commonly today Three-Dimensional Conformal Radiation Therapy (3D-CRT), Intensity Modulated Radiation Therapy (IMRT), Volumetric modulated arc therapy (VMAT) and TomoTherapy® are the techniques used.

Three-Dimensional Conformal Radiation Therapy (3D-CRT) has been commonly used in the past since it uses Multi-Leaf Collimators (MLCs) to conform or shape the prescription dose volume of the prostate and other affected areas to the PTV, while at the same time keeping the dose to specified organs at risk below their tolerance dose. 3D-CRT is based on 3D target localisation, 3D treatment planning, and 3D dose delivery techniques. Target localisation is accomplished through anatomical and functional imaging: CT, MRI, single photon emission computed tomography (SPECT), PET and ultrasound. Treatment planning is accomplished either with standard forward planning techniques, which configure uniform intensity beams shaped to the geometrical projection of the target or for further developed conformal radiotherapy techniques with inverse planning, which in addition to beam shaping, utilises intensity modulated beams to enhance target dose homogeneity and spare organs at risk. Dose delivery techniques range from the use of standard regular and uniform coplanar beams to intensity modulated non-coplanar beams created with MLCs.

The concept of 3D conformal dose distribution has a major limitation which involves

limited knowledge on the extent of the tumour. Despite the modern advances in imaging, the clinical target volume (CTV) is often not fully discernible and imaging techniques do not reveal the CTV. Due to the invasive capacity of the disease, only the gross tumour volume (GTV) is imaged, which may result in the entire tumour being missed or underdosed [10]. Hence, 3D-CRT is not a new modality of treatment and is not proven to be better than other well-tested forms of conventional radiation therapy.
IMRT is an advanced form of 3D-CRT which involves the treatment of the patient from a number of different directions. This is the same as 3D-CRT, which is also delivered from multiple angles and is optimised to deliver a high dose to the target volume and acceptably low dose to the surrounding normal structures. IMRT treatments generally deliver doses of 2-2.5 Gy per fraction, for a total of 75-85 Gy over 30-36 days [11]. Most Australian men with localised prostate cancer receive conventionally fractionated treatment. This treatment consists of 1.8-2 Gy per fraction, for a total of 74 Gy in 37 fractions [12].

IMRT treatments are delivered in static or dynamic mode. Static IMRT often referred to as the step and shoot mode, where the intensity modulated fields are delivered with a sequence of small segments or subfields, each subfield with a uniform intensity. This is where the beam is only turned on when the MLC leaves are stationary in each of the prescribed subfield positions during dose delivery. Dynamic IMRT is often referred to as the sliding window mode, where the intensity modulated fields are delivered in a dynamic manner with the MLC leaves moving during delivery. For a fixed gantry position, the opening shaped by each pair of opposing MLC leaves is swept across the target volume under computer control with the radiation beam turned on to create the desired fluence map.

Furthermore, IMRT has been shown to have a steep dose gradient outside target bound-

aries. This steep gradient has a great advantage near the edge of the treatment field, however, far from the treatment field, this advantage is lost. This is due to the fact that near the treatment field IMRT can provide a more conformal treatment, which decreases the volume of tissue receiving high doses. However, far from the treatment field, with the presence of modulation, a higher amount of monitor units and greater beam on time leads to increased head leakage and therefore higher doses farther from the treatment field [13] compared to 3D conformal treatments.

TomoTherapy® is an alternative option used to deliver EBRT. TomoTherapy® involves the use of multiple rotations of a narrow fan beam with a continually changing one-dimensional profile delivering dose to the patient. The process of dose delivery involves multiple binary MLCs (i.e. either in the open or closed state operating in the superior/inferior direction of the patient) forming a one-dimensional profile that constantly changes. Combining the one-dimensional profile with the beam rotation, intensity modulation in two dimensions is produced. The patient is also transported through the field as the beam is rotated, leading to a helical delivery. The combination of the one dimensional profile and the helical delivery leads to the two dimensions. TomoTherapy® can deliver treatment with a sequence of rotational modulated beams (known as serial TomoTherapy®), with each rotation at a fixed couch position or as a beam following a helical trajectory relative to the patient. Furthermore, advantages of TomoTherapy® include its proficiency in generating very complex, high intensity modulated dose distributions due to its greater number of degrees of freedom and that it has the ability to treat large volumes in a single treatment delivery.

Volumetric modulated arc therapy (VMAT), another option for EBRT, it is a unique form of IMRT optimisation that allows the radiation dose to be delivered in more than one rotation of up to 360 degrees, using either a constant dose rate or variable dose rate

during rotation. This technique is similar to TomoTherapy® in that a full 360 rotation of beam directions are available, however, it is fundamentally different in that the dose is delivered to the entire planning target volume (PTV) in a single source rotation and the patient is static. The modulated field in VMAT is achieved by varying dose rate, MLC aperture and orientation, and gantry angle, with the beam, switched on continuously for efficient treatment.

A study by Palma et al. (2008) [14] discussed the use of VMAT in comparison with IMRT and 3D-CRT for the treatment of prostate cancer. VMAT, IMRT, and 3D-CRT plans were created for 10 computed tomography data sets. The parameters evaluated were dose to organs at risk, equivalent uniform doses, dose homogeneity and conformity and monitor units required for delivery of 2 Gy per fraction. Both IMRT and VMAT techniques resulted in lower doses to normal critical structures than 3D-CRT. The lowest dose to organs at risk and most favourably equivalent uniform doses were achieved with VMAT which was significantly better than IMRT. The VMAT plans required fewer monitor units than IMRT and 3D-CRT [14]. Fewer monitor units are particularly advantageous in reducing the out-of-field, scattered and leakage doses.

A study by Wolff et al. (2009) [15] compared VMAT to serial TomoTherapy®, step-and-shoot IMRT and 3D-CRT for treatment of prostate cancer. Based on CT datasets of 9 patients treated for prostate cancer step-and-shoot IMRT, serial tomography (MIMiC), 3D-CRT and VMAT were compared in regards to plan quality and treatment efficiency. All the approaches showed improved quality when compared to 3D-CRT treatments, with serial Tomotherapy®, providing the best OAR sparing and VMAT being the most efficient treatment option in the comparison, reducing treatment time to 1.8-3.7 minutes and MU to $<$400 MU for a 2 Gy fraction [15].

A study by Tsai et al. (2011) [16] compared step-and-shoot IMRT, helical TomoTherapy®, and VMAT, in terms of treatment and dosimetry for prostate cancer. Three plans for each treatment delivery method were completed for twelve patients. The study found that the mean required MUs were 309.7 for VMAT, 336.1 for step-and-shoot and 3368 for TomoTherapy®. The advantage of lower MUs is a less scattered dose to the body. The treatment time required was lowest for VMAT at 2.6 minutes, with step-and-shoot IMRT and TomoTherapy® taking 3.8 minutes [16]. Less treatment time is advantageous in terms of potentially reducing intrafractional movement [17] and reducing out-of-field, scattered and leakage doses [18]. Although Helical TomoTherapy® can have treatment times longer than treatment times using a conventional linear accelerator. When comparing to RapidArc (Varians implementation of VMAT), a typical prostate treatment time using TomoTherapy® requires a treatment time of 4-7 minutes, whereas RapidArc takes only 1.5 minutes. This treatment time is only for simple cases [19,20]. Despite the longer treatment times, the greater amount of shielding involved in the TomoTherapy® system minimises radiation leakage that could be detrimental to patients [18].

Another study by Davidson et al. (2011) [21] assessed the role of VMAT relative to IMRT and Helical TomoTherapy® in the management of localised, locally advanced and post-operative prostate cancer. Twenty-five prostate cancer patients were selected for this study to quantify the differences in treatment delivery and dosimetry between the various treatment modalities. This study showed that VMAT provided the most improvement in efficiency of delivery resulting in reduction in treatment times over IMRT and Helical TomoTherapy®. VMAT also required much fewer monitor units than IMRT over all treatment volumes, with the reduction per fraction ranging from 100-423 MU from the smallest to largest volumes [21]. The study clearly demonstrated that VMAT offers the potential to deliver treatment plans of equal quality with more efficiency and fewer MUs than IMRT or Helical TomoTherapy® in all simple and complex volumes

involved in prostate cancer radiotherapy.

Overall, for prostate treatments, the number of MUs have been reported to be 16-39% lower for VMAT than for step-and-shoot IMRT [15,21,22]and 42-68% lower than for sliding window IMRT [14, 22, 23]. For single arc therapy, the leakage radiation is lower, hence the out-of-field doses are slightly lower for VMAT than for step-and-shoot IMRT [22]as shown in Figure 2.2. Near the treatment field, where internal patient scatter dominates, there is no difference between VMAT and other IMRT modalities.

Conclusively, VMAT has been reported to deliver similar dose distributions to IMRT while using fewer monitor units (MUs). When scatter and leakage are the major contributors to dose at points outside of the field edge, VMAT has the potential to reduce out-of-field doses by using fewer MUs. Most standards require that the linac head leakage dose be less than 0.1% of the useful (primary) beam dose [24]. However, the magnitude of the combined scatter and leakage dose varies with beam energy, field size and the distance from the field edge, and therefore, accurate estimation of out-of-field dose requires measurements and calculations performed under clinically realistic conditions.

The photon dose equivalent as a function of distance from central axis for 6 MV and 10 MV beam on a Varian and Siemens delivery system for IMRT treatment of prostate is shown in Figure 2.1 [25]. Dose as a function of distance from central axis for 6 MV beam delivery on a Siemens delivery system for IMRT and VMAT treatment of the prostate is shown in Figure 2.2 [22]. In Figure 2.1, close to the field edge, there is minimal difference in out-of-field dose for 6 MV and 10 MV IMRT treatment. In Figure 2.2, close to the field edge there is no difference in out-of-field dose for IMRT and VMAT treatments. For both Figures 2.1 and 2.2, further away from the field edge at distances greater than 20 cm the out-of-field dose increases and this becomes of great concern.

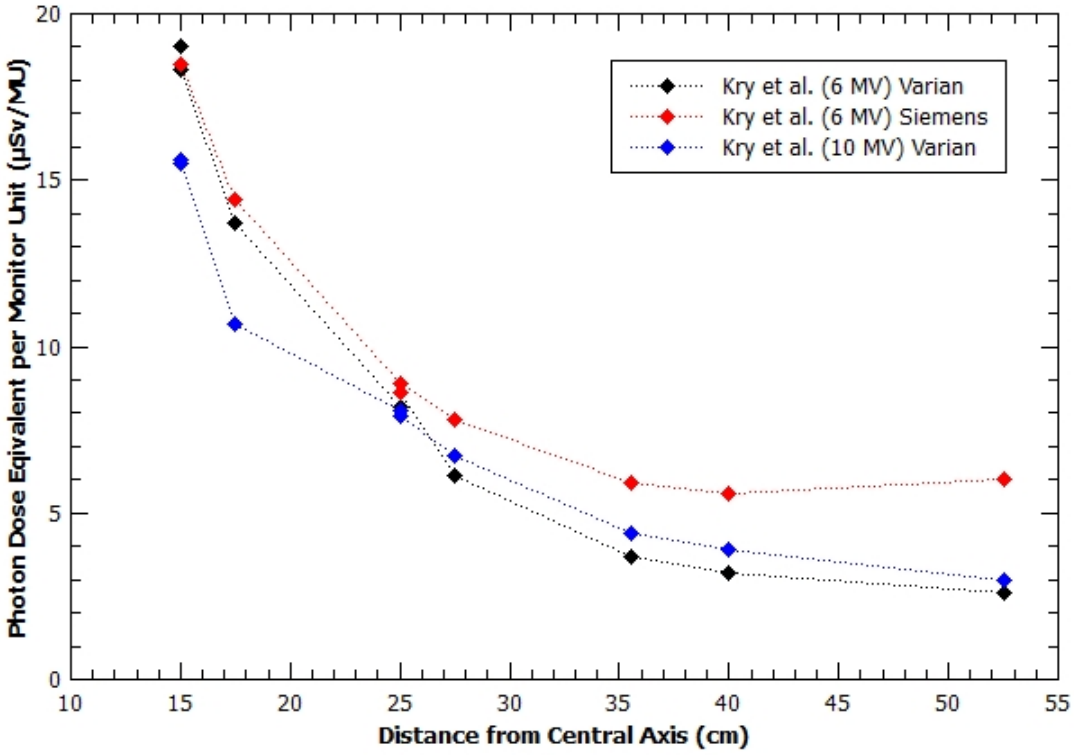

Figure 2.1 Photon Dose Equivalent as a function of Distance from Central Axis for IMRT of the prostate Kry et al. (2005b) [25].

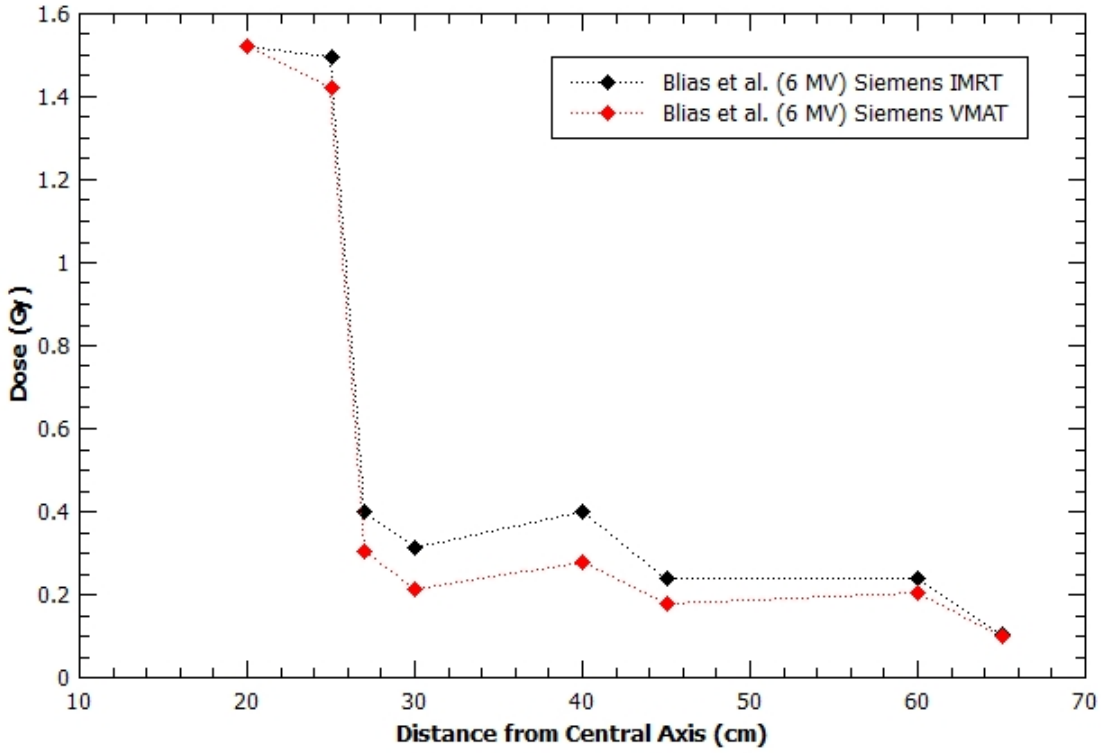

Figure 2.2 Dose as a function of Distance from Central Axis for IMRT and VMAT of the prostate Blais et al. (2012) [22]

2.4 Linear Accelerators

A linear accelerator (LINAC) is currently the most standard device used for external beam radiation treatments for patients with cancer. A clinical linear accelerator uses high frequency electromagnetic waves to accelerate electrons to high energies, generating photons. A typical modern high energy LINAC can provide 6, 10 and 18 MV photon energies and 6, 9, 12, 16 and 22 MeV electron energies. Some linear accelerators provide x-rays only in the low mega-voltage range (4 or 6 MV), while others provide both x-rays and electrons at various megavoltage energies. For the treatment of superficial

tumours a high-energy electron beam is used. For the treatment of deep-seated tumours the high-energy electron beam can be made to strike a target to produce high energy x-rays with penetrating characteristics.

Within a LINAC electrons are accelerated linearly in an accelerating waveguide to a high velocity using energy from high-power microwaves which are delivered to the accelerating structure in the form of short duration pulses (5 microseconds duration) from the klystron or magnetron through a transmission microwave waveguide. An electron gun injects low-energy electrons at one end of the accelerating waveguide. The electrons are accelerated along the guide to speeds approaching the speed of light. The electrons then enter a bending magnet assembly whereby they are redirected toward the centre of the beams gantry axis of rotation known as isocentre. When the LINAC is operated in x-ray mode, the electron beam hits a target and x-rays are produced by the bremsstrahlung production process. When the LINAC is used in electron mode, the electrons are made to strike a scattering foil prior to exiting the LINAC. A detailed schematic showing the LINAC waveguide and beam path with beam monitoring and collimation systems is shown in Figure 2.3. Figure 2.3 shows the main components of the LINAC that are housed in the gantry. Also shown are the connections and relationships among the various LINAC components.

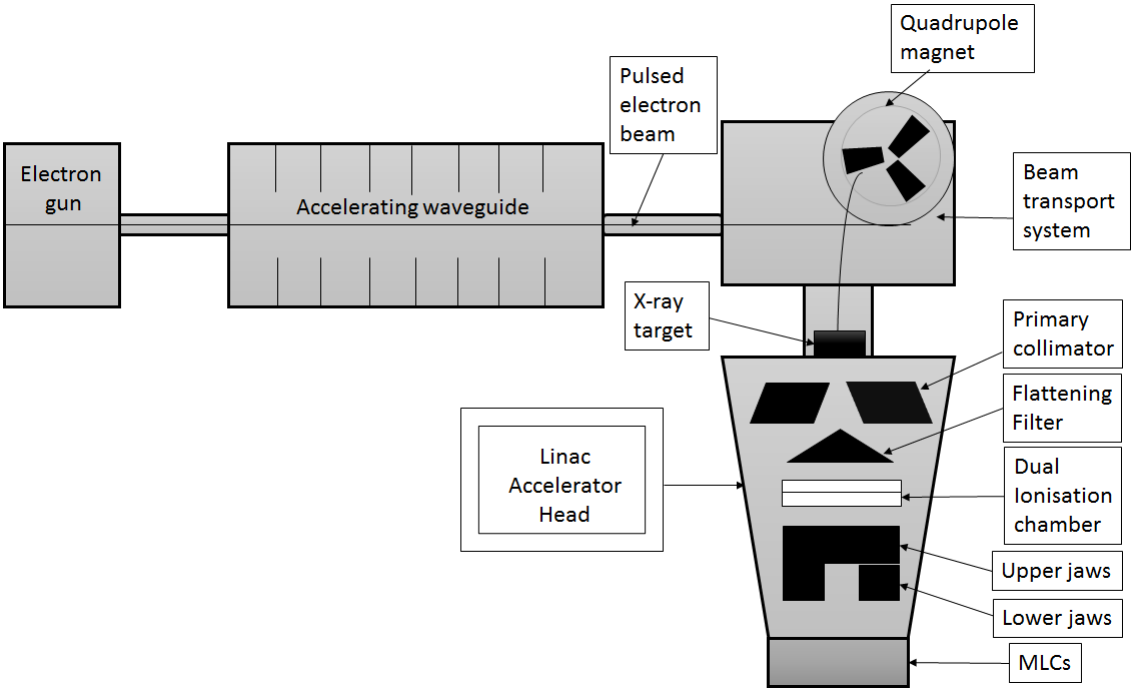

Figure 2.3 Schematic drawing of the internal components of a medical linear accelerator, adapted from [24].

2.4.1 Linear Accelerator Head

A LINAC treatment head contains numerous mechanisms that influence the production, shaping, confining and monitoring of the clinical photon and electron beams. Electrons originating in the electron gun are accelerated in the accelerating waveguide to the desired kinetic energy to be transported, in the form of a pencil beam, through the beam transport system into the LINAC treatment head, where the clinical photon and electron beams are produced [24].

The major components found in a typical LINAC include: several retractable x-ray targets, primary collimators, flattening filters and electron scattering foils (also called

scattering filters), dual transmission ionisation chambers, adjustable secondary collimators (upper and lower jaws), a field defining light with a range finder and multi-leaf collimators (MLCs).

A clinical photon beam is accomplished with three collimator devices: a primary collimator, secondary movable beam defining collimators (upper and lower jaws) and multi-leaf collimators (MLCs). In expansion to the primary and secondary collimators, clinical electron beams require electron beam applicators (cones) for beam collimation.

The primary collimator characterises the largest available round field size and is a conical opening machined into a tungsten protecting block, with the sides of the conical opening projecting on to edges of the target on one side of the block and on to the flattening filter on the opposite end. The thickness of the protecting block is typically intended to attenuate the average primary x-ray beam intensity to under 0.1% of the underlying value (three tenth-value layers (TVLs)). As per the International Electro-technical Commission (IEC) suggestions, the maximum leakage should not surpass 0.2% of the open beam value [24].

The secondary beam defining collimators are made of four blocks, two shaping the upper and two shaping the lower jaws of the collimator. The secondary collimators are able to provide rectangular or square field sizes of up to 40 cm x 40 cm, at the linac isocentre. Modern LINACs can also include independent (asymmetric) jaws that are able to provide asymmetric fields [24].

Multi-Leaf Collimator (MLCs) provide additional conformal shaping of the radiotherapy treatment beams. Using an MLC, the fluence profile of the beam is modulated through the use of multiple smaller segments or by the use of a sliding window, whereby

the MLC leaves move across the portal in an ever changing sequence, irradiating only a portion of the field at any moment in time. The number of MLCs in commercial LINAC machines is approximately 120 leaves (60 pairs) covering fields sizes of up to 40 cm x 40 cm and requiring 120 individually computer controlled motors and control circuits. Since the introduction of MLCs, they have become invaluable in supplying intensity modulated fields in IMRT and/or VMAT [24].

Therefore, treatments that involve a linear accelerator use multiple mechanisms that influence the shaping, confining and monitoring of the clinical photon and electron beams, with heterogeneous fluence profiles to produce complex isodose distributions, improve target coverage and simultaneously avoid organs at risk.

2.5 Sources and Characteristics of Out-of-Field Dose

The longer beam-on times and longer monitor units required for IMRT and VMAT treatments results in three unintended sources of radiation (2.4):

1. Patient scatter, scatter of the primary treatment beam outside the treatment area once it has entered the patient;
2. Collimator scatter, scatter of radiation in the head of the accelerator, which exits the accelerator through the treatment field opening but strikes the patient outside the treatment field; and
3. Head leakage, radiation that penetrates through the accelerator head shielding and strikes the patient away from the treatment field [13].

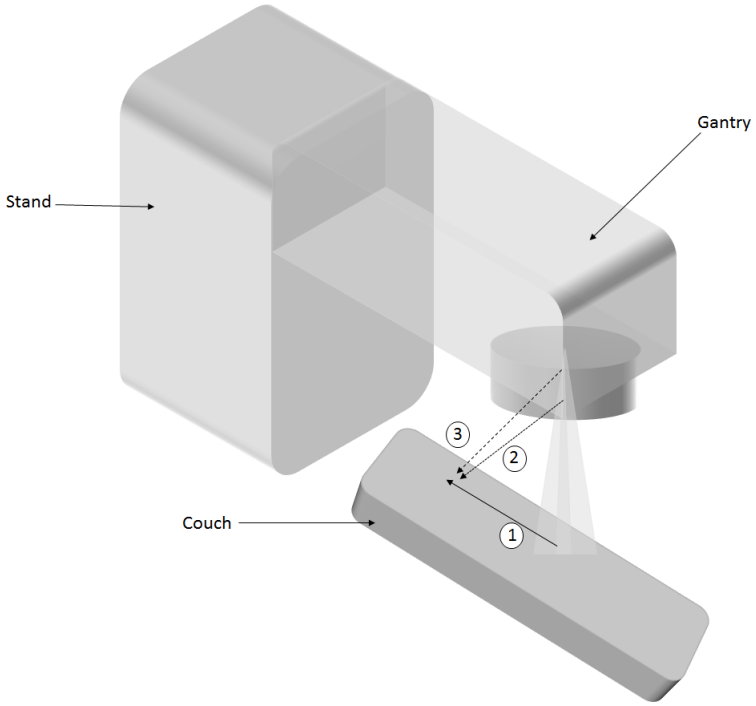

Figure 2.4 Sources of out-of-field dose from a medical linear accelerator: (1) patient scatter, (2) secondary collimator scatter; and (3) head leakage.

The total dose outside the treatment field is affected by the distance from the field edge. In an IMRT treatment, the fall-off in dose considerably depends on the objectives and quality of the treatment plan [13]. The dose outside the treatment field also depends on field size, increasing with increasing field size as larger irradiated volumes produce more patient scatter. This field-size dependence is most pronounced close to the field edge, where patient scattered radiation is the most important component of the out-of-field dose. Away from the field edge, there is no field size dependence.

For modulated treatments, the dose outside the treatment field also depends on beam modulation. The dose increases with increasing modulation as more head leakage is

generated as the number of monitor units (MU) increases to deliver the modulated fields. Beyond 20 cm from the field edge, head leakage radiation that penetrates through the accelerator head shielding and collimator scatter radiation in the head of the accelerator, which exits the accelerator through the treatment field opening and strikes the patient outside the treatment field, becomes the most important component of the out-of-field dose. The dose modulation dependence is the most noticeable, away from the field edge, whereas very near the field edge there is no modulation dependence. Differences among accelerator head models as a result of variations in head shielding designs and beam energy spectra can also cause out-of-field dose to differ slightly.

In contrast, out-of-field dose varies minimally with depth in the patient, however, there is an exception to this depth independence near the surface of the patient. The dose at the surface is highly elevated by electrons from the accelerator head; this dose elevation is maximal at the surface and decreases with depth until d_{max} and then remains relatively constant at all depths below that [26].

Therefore, patient scatter has been reported to be the dominant source of radiation dose outside the field for approximately 0-10 cm from the field edge and at distances greater than 20 cm, head leakage and collimator scatter radiation dominates [13]. Due to the contributions of patient and collimator scatter, the energy spectrum is softer outside the treatment field than within. This means that the mean energy inside the treatment field at d_{max} for a 6 MV photon beam is approximately 1.6 MeV (for a Varian accelerator) and the average energy of the photon spectrum outside of the treatment field is typically between 0.2 and 0.6 MeV [27].

2.5.1 MLC and Collimator Orientation

Leakage through the MLCs consists of transmission through the leaves and leakage between the leaves. The presence of MLCs offers additional head shielding to the LINAC and reduces the overall head leakage and collimator scatter reaching the patient. With Varian LINACs the presence of MLCs has the potential to reduce the out-of-field dose by strategically orienting their location. If the MLC leaves open along the axis of the patient (as opposed to across the patient axis), the leaves continue to shield the patient, reducing the dose by 6% to >50% depending on the distance from field edge [26]. In order to reduce out-of-field dose, jaws and MLCs should be as close as possible. This is not feasible with the treatment of patients as the orientation of jaws and MLCs varies with differing treatment sites.

2.6 Critical Out-of-Field Regions in Prostate Radiation Therapy

2.6.1 Eye Lens: Cataracts

Cataracts lead to the loss of transparency of the eye lens, which can progress slowly to cause vision loss and may eventually lead to blindness. Cataracts are the most common eye disease and the most common cause of visual impairment in the world. A report by AIHW, *Cataracts in nearly one third of older Australians* [28] stated that in 2004, almost 1.5 million Australians aged 55 or over suffered from untreated cataracts, which represents 31% of that population. Age-specific rates for cataracts increase with age for both men and women and are over 70% for men and women aged 80 or more. Prevalence rates are higher amongst women than men [28].

Within years after the discovery of X-rays, severe adverse effects to the eye from radiation were reported and cataract formation was seen to be one of the earliest effects observed among atomic bomb survivors. The subcapsular lens epithelium, particularly where it differentiates to lens fibres, is highly susceptible to radiation damage. The development of radiation-induced cataracts is dependent on radiation dose, dose rate and age of the lens, and is a known late effect from radiation therapy [29]. As a result of epidemiological studies on Chernobyl clean-up workers, interventional radiology and atomic bomb survivors [29,30], the threshold for cataract induction was suggested to be lower than previously assumed. As a result, the need for a detailed re-evaluation of the eye lens radiosensitivity and an associated reliable dose assessment was essential. The Statement on Tissue Reaction was released by the ICRP, which pertained to the acceptable recommendation for the revision of the eye lens limit, lowered the annual limit of radiation dose from 150 mSv to 20 mSv [1].

In a recent study by Behrens et al. (2009) [2], the depth of the sensitive region of the eye lens was found to be between 2.8 mm and 3.8 mm, with a mean value of 3.4 mm [2]. This means that since the sensitive region of the eye lens where radiation becomes of critical concern is between 2.8-3.8 mm, low penetrating radiation such as electrons are able to deposit dose resulting in a risk of developing a cataract [2]. A detailed diagram of the eye lens, particularly the radio-sensitive region, is illustrated in Figure 2.5.

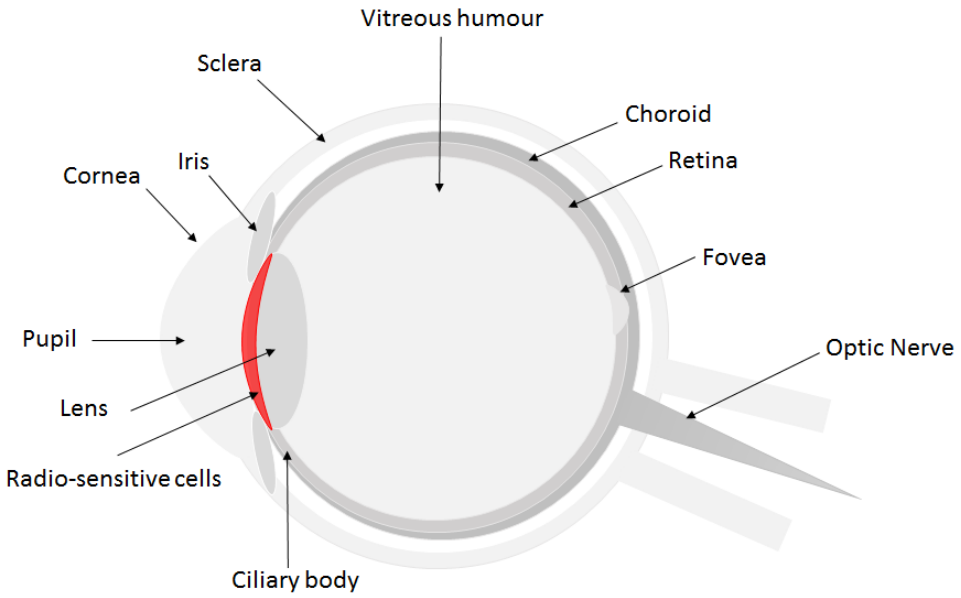

Figure 2.5 Diagram of the eye representing the radio-sensitive region of the lens.

2.6.2 Chest: Cardiac Implantable Electronic Devices (CIEDs) such as: Pacemakers and Implantable Cardiac Defibrillators (ICDs)

Cardiac Implantable Electronic Devices (CIEDs), such as pacemakers and implantable cardiac defibrillators (ICDs), are implanted subcutaneously overlying the pectoral muscles or occasionally implanted in the abdominal wall of patients with arrhythmia. CIEDs are located at depths of 5-30 mm below the skin surface [31, 32]. A pacemaker helps control abnormal heart rhythms using electrical pulses to prompt the heart to beat at a normal rate. An ICD monitors heart rhythms of patients who are at risk of sudden cardiac arrest (SCA) and is designed to deliver an electrical shock to the heart when the heart rate becomes dangerously fast, or fibrillates. The ICD can be programmed to provide therapy when required. Most new ICDs can now act as both a pacemaker and defibrillator.

Cardiac Implantable Electronic Devices (CIEDs) are sensitive to relatively low levels of radiation, as documented in AAPM Report TG-34 [33] and EviQ guidelines [3]. Pacemakers and ICDs may be affected by radiotherapy to the lung, breast, chest wall, head and neck, skin and for lymphomas. Implantable electronic devices, if exposed to excessive cumulative doses, can malfunction as a result of a build-up of electrical charge and for this reason, it is imperative to be aware of the dose assessment to these devices. Dose malfunctions can also occur from other mechanisms, such as dose rate effects (which have a complicated mechanism but have been observed at very low doses) [34].

There is a significant risk that CIEDs malfunction due to neutrons generated by x-ray beams of energies 10 MV or greater. Such neutrons have been documented to cause CIED malfunction when the device was 1.4 meters from the beam edge. The increased risk of using high energy photon beams applies to the treatment of any part of the body. Some earlier studies in the literature used $>$10 MV beams to estimate the dose sensitivity of CIEDs and may have overestimated the effect of dose due to unrecognised neutron effects [3].

There are no universal guidelines specifying radiation dose limits to cardiac implantable electronic devices (CIEDs) such as pacemakers and ICDs sensitive to ionising radiation. Although it is widely accepted that accumulatively doses above 2 Gy for pacemakers and 1 Gy for ICDs should be avoided and they should not be placed in the direct path of the radiation beam. Damage caused by neutrons is much greater than that caused by photons. Unwanted neutron contamination is only produced for photon beam energies greater than 10 MV. Therefore, considerable published observational (in-vivo) data suggests that the majority of radiation therapy associated CIED malfunctions are due to neutron exposure (from photons $\geq$10 MV) [35]. There is uncertainty in the safe levels of radiation exposure for CIEDs, however since the release of the 2017 HRS Interna-

tional expert consensus statement, the risk of failure of the device is low, as there is no evidence of damage up to 5 Gy [35]. It is also recommended that patients with CIEDs be treated with photon beams of 10 MV or lower to avoid the risk of malfunction. Out-of-field doses measured for prostate patients to the chest will be well under this limit unless the device is within a few centimeters of the field edge.

2.7 Dosimeters for Out-of-Field Dose Measurements

2.7.1 Solid State Dosimeters

Common types of radiation detectors used in dosimetry are diode, diamond, MOSFET, TLD, ionisation chambers and radiochromic film. The measurement of dose outside the treatment field poses many unique challenges. Due to the radiation field being different from inside the treatment field, the dose outside the treatment field is difficult to detect as signals for most detectors are extremely low. On the basis of that, specific implications of the size, sensitivity, accuracy, cost, and workload need to be considered for each separate dosimeter before being selected as suitable for out-of-field measurements. An ideal radiation dosimeter for out-of-field dose measurements would be able to detect such low signals with stability. Ideally, a radiation dosimeter would have a number of favourable features such as being stable, linear with dose, linear with dose rate, energy independent, independent of radiation type, direction independent, have direct read-out capabilities and require minimal correction.

Diode detectors allow for real-time readout, have small sensitive volumes, high spatial resolution and are mechanically rugged such that handling will not influence its high

sensitivity. A disadvantage that makes diodes unsuitable for out-of-field measurements is their energy dependence at low energies. Diodes show variation in dose response with temperature, dependence of signal on the dose rate, angular dependence, and energy dependence [24].

Diamond detectors are solid-state detectors with a small sensitive volume (<0.01 cc). Diamond detectors have a low atomic number (Z = 6) which is close to the effective atomic number of water ($Z_{eff} = 7.4$), as a result they have negligible energy dependence and are useful across a wide range of field sizes. A study by Rodriguez et al. (2007) [36] measured the current of a diamond detector in air at 100 cm from a Co-60 source in a 10 cm x 10 cm field to be 5.5 nA at a bias voltage of 150 V. On the other hand, with the same setup, the current measured with an ionisation chamber was found to be 0.39 nA at a bias voltage of -300 V. This study showed that the sensitivity of a diamond detector is higher than an ionisation chamber [36]. The main drawbacks of diamond detectors is their lack of immediate availability, to their manufacturing difficulty and higher cost compared to ionisation chambers and diodes.

The Metal oxide silicon semiconductor field effect transistor (MOSFET) detector is a miniature silicon transistor. MOSFETs are capable of real-time measurements, possess high spatial resolution, small in size and are based on the measurement of the threshold voltage, which is a linear function of absorbed dose. Ionising radiation penetrating the oxide generates charge that is permanently trapped, thus causing a change in threshold voltage (an electrical characteristic of the device). The integrated dose may be measured during or after irradiation. MOSFETs have a limited lifespan. They can be exposed with no applied voltage and can be implanted interstitially. MOSFETs have been previously used for out-of-field measurements by Wang and Xu (2008) [37], their advantages include its small size, immediate readout, ease of use and linear response for

large dose ranges. The disadvantages of MOSFETs include low sensitivity and angular dependence due to their asymmetric design.

Thermoluminescent detectors (TLDs) are relative dosimeters that have sufficient sensitivity for low-dose applications. These detectors are small in size and are available in various forms for in-vivo measurements. Disadvantages that make TLDs unsuitable for out-of-field measurements are their energy dependence and lack of real-time measurement capability. TLDs have a long and time consuming readout and calibration time. According to Rosenfeld (2002) [38], the over layer of a TLD is too thick to be able to obtain measurements at shallow depths. A study conducted by Kry et al. (2006) [26] measured out-of-field dose with thermoluminescent dosimeters (Harshaw, TLD-100), where the TLDs were placed in slots at specific depths in the phantom. The TLDs were read out by the Radiological Physics Centre (RPC, Houston TX). The RPC TLD analysis technique included multiplicative correction factors to be applied to the raw dose to account for the fading, non-linearity and energy dependence of the TLDs [26]. Thus, the use of TLDs is deemed unsuitable in this study for the out-of-field measurements due to the lack of instant readout and time consuming correction factors required to be applied to the raw dose.

Radiochromic film is used as a radiation detector by changing colour after exposure to ionising radiation. This occurs when the photo monomer molecules in the film, which are colourless, undergo a chemical change due to the energy transfer from the incoming photons/particles. This colour change is what is measured to determine optical density, which is ultimately a function of the dose deposited [39]. Film is commonly used for surface measurements, for example for patients receiving radiation therapy to the breast, which is associated with acute and late skin toxicity [40]. EBT Gafchromic film has been previously used to measure doses outside the treatment field by Chiu-Tsao et

al. (2009) [41] and Van den Heuvel et al. (2012) [42]. Gafchromic is relatively insensitive and the uncertainties associated with the very low doses being measured in this study (in the order of 10 cGy) make film unsuitable.

Based on the dosimeter characteristics discussed above it was deduced that neither of the solid state dosimeters were found to be suitable for measuring out-of-field dose. Therefore it was decided to use ionisation chambers in our study of out-of-field dose.

Table 2.1 summarises the suitability of the most commonly used dosimeters in terms of size, sensitivity, accuracy, cost, and applications of the dosimeter.

2.7.2 Ionisation Chambers

An ionisation chamber is a gas filled cavity encompassed by a conductive external wall with a central collecting electrode. The wall and the collecting electrode are isolated with a high quality insulator to lessen the leakage current when a polarising voltage is connected to the chamber. A guard electrode is normally given in the chamber to further diminish chamber leakage. The guard electrode intercepts the leakage current and allows it to flow to ground, bypassing the collecting electrode. It additionally guarantees enhanced field uniformity in the active or sensitive volume of the chamber, with resulting advantages in charge collection.

An ionisation chamber is a capacitor in which leakage current is induced through the action of the radiation beam. The current that is induced in the chamber is very small and must be measured by a highly sensitive current measuring device such as an electrometer. Electrometers are able to measure small currents, of the order of 10^{-9} Amperes or less [24]. An electrometer utilised as a part of conjunction with an ionisation chamber is a high gain, negative feedback, operational amplifier with a standard resistor or a stan-

dard capacitor in the feedback path to quantify the chamber current or charge gathered over a fixed time interval [24]. The power supply in an ionisation chamber/electrometer circuits is either a stand-alone unit or forms an integral part of the electrometer. It is therefore important that the magnitude and polarity of the voltage delivered by the power supply can be readily changed so that the ion efficiency of the chamber could be determined for a particular radiation beam.

Ionisation chambers can vary in size, active volume, and shape. Ionisation chambers are produced by various manufacturers with varying sizes and active volumes ranging from 0.1 cm^3 to 1.0 cm^3. Ionisation chambers can be either cylindrical or parallel plate. A different ionisation chamber is used for a different task such as:

- Medium Volume (0.6 cm^3) cylindrical ionisation chambers are used for measuring dose and dose rates at reference points in a phantom for megavoltage photon beams and electron beams above 10 MeV in order to obtain a reasonable signal and good signal to noise ratio.
- Small volume (0.1-0.125 cm^3) cylindrical ionisation chambers are used for fine point dose measurements, PDDs and beam profiles for photon beams and for electron beams in order to obtain good spatial resolution.
- Parallel plate ionisation chambers, incorporating a thin polarizing electrode window and a small electrode separation (typically 1 mm, for better spatial resolution) are used to measure surface dose and doses in the build-up region for photon beams.

2.7.2.1 Cylindrical Ionisation Chambers

The most popular cylindrical ionisation chamber is the 0.6 cm^3 chamber designed by Farmer, for beam calibration in radiotherapy dosimetry. A cross section schematic dia-

gram of a cylindrical Farmer type ionisation chamber is shown in Figure 2.6.

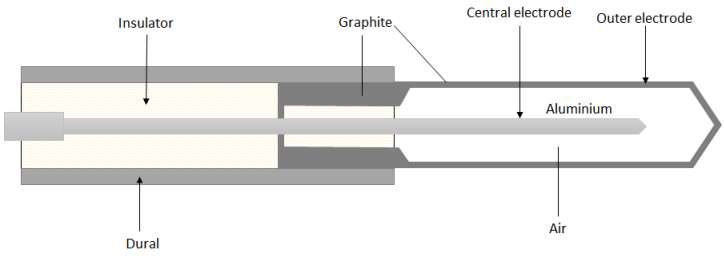

Figure 2.6 Cross section schematic of a Cylindrical Farmer type ionisation chamber, adapted from [24].

Cylindrical chambers are produced by several manufacturers, with active volumes between 0.1 cm^3 and 1.0 cm^3. They usually have an internal length no greater than 25 mm and an internal diameter no greater than 7 mm. The central electrode can be made of aluminium or graphite. The wall material is of a low atomic number (i.e. tissue or air equivalent), with the thickness less than 0.1 g/cm^2. A chamber is equipped with a build-up cap with a thickness of approximately 0.5 g/cm^2 for calibration free in air using Cobalt-60 radiation [24].

2.7.2.2 Parallel-plate Ionisation Chambers

Parallel-plate ionisation chambers are comprised of two plane walls, one serving as an entry window and polarising electrode and the other as the back wall and collecting electrode, in addition to a guard ring system. The back wall is typically a block of conducting plastic or non-conducting material (usually Perspex or polystyrene) with a thin conducting layer of graphite forming the collecting electrode and the guard ring system on top [24]. A schematic diagram of the top view and side view of a parallel-plate ionisation chamber is shown in Figure 2.7 and Figure 2.8. The parallel-plate chamber is recommended for dosimetry of electron beams with energies below 10 MeV. It is also

used for surface and depth dose measurements in the build-up region of megavoltage photon beams [24].

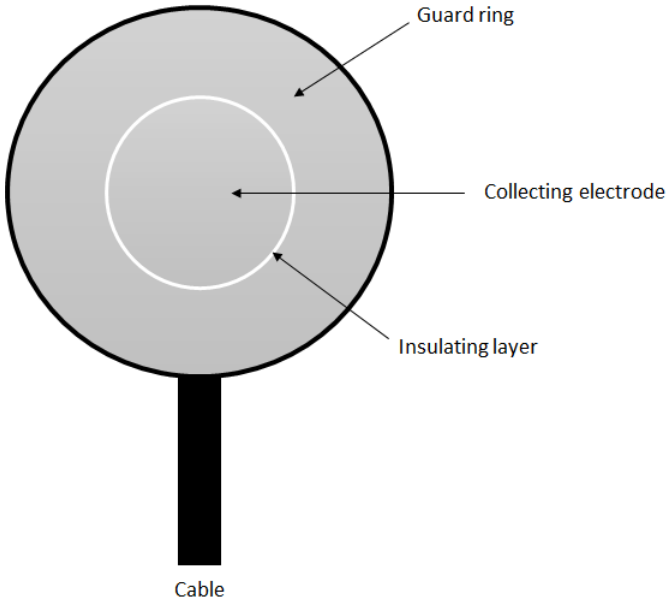

Figure 2.7 Schematic diagram of Parallel-plate ionisation chamber.

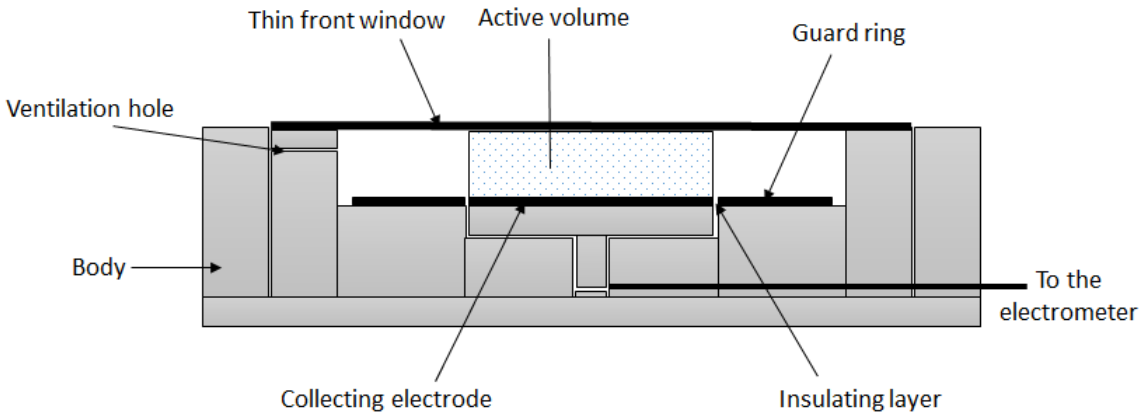

Figure 2.8 Cross section schematic of a parallel-plate ionisation chamber, adapted from [24].

2.7.2.3 Comparison between cylindrical and parallel plate ionisation chambers

Desirable characteristics of cylindrical and parallel plate ionisation chambers are their low energy dependence, low dose rate dependence and high sensitivity. Their small size and portability for easy placement is convenient and their ability for instant readout allows the dose delivered to be monitored while not needing to undergo procedures such as annealing, unlike thermoluminescent dosimeters (TLDs).

Less desirable characteristics of cylindrical ionisation chambers include its asymmetrical design and stem since the dose response will vary with the incident angle of radiation to its cylindrical axis. This is particularly noticeable at superficial and orthovoltage radiation energies. Other less desirable characteristics of ionisation chambers include requiring connecting cables for the set-up of the device and a high voltage supply required for the low signal readings.

Ionisation chambers have been used previously to measure out-of-field dose. In a study by Ruben et al. (2011) [43], a Farmer-type FC65-P cylindrical ionisation chamber (IBA Dosimetry GmbH, Schwarzenbruck, Germany) was used to measure out-of-field dose. In another study by Kry et al. (2006) [26], a RK CC04 cylindrical chamber (Scanditronix-Wellhofer) was used to measure out-of-field dose. Ruben et al. (2011) and Kry et al. (2006) found that ionisation chambers were useful dosimeters for their out-of-field measurements, due to their small size, high precision, high sensitivity, minimal energy dependence and real-time measurement capability [26,43]. Therefore, based on the characteristics discussed above, cylindrical ionisation chambers were concluded to be the most suitable dosimeters for measurement of out-of-field dose.

Dosimeter	Size	Sensitivity	Accuracy	Important Applications
Diode	Very small size: 1-2 mm diameter, thickness 0.06 mm	High sensitivity and high spatial resolution	Instant readout and easy to use	High accuracy for in-vivo dosimetry, electron scanning and small field photon dosimetry.
Diamond	Very small size, circular, microdiamond detector: 2.2 mm diameter, thickness 0.001 mm (0.004 mm)	High sensitivity	Atomic number close to water, real-time measurement, may require pre-irradiation	Water tank measurements and small field dosimetry with high accuracy.
MOSFET	Very small size: 0.2 mm diameter, thickness 0.001 mm	Medium sensitivity	Instant readout, robust and easy to use	Water tank measurements (penumbra, electrons), in-vivo dosimetry, and small field dosimetry and detector arrays.
TLD	Small size 3 mm x 3 mm x 1 mm	Medium sensitivity	Accurate results require care, readout calibration must be done with care	In-vivo dosimetry, measurements in anthropomorphic phantom and slab phantoms, inter-comparisons between centres, personal dosimetry, point dose measurements.
GAF(film)	Variable sizes, very high spatial resolution	Low sensitivity	Processing is difficult to control	Measurements in solid and anthropomorphic phantoms, qualitative dosimetry QA, portal imaging, IMRT, QA and for high dose measurements.
Cylindrical Ionisation Chamber	Farmer chamber: 25 mm length by 7 mm diameter (0.6 cm^3). Semi-flex chamber: 6.5 mm length by 5.5 mm diameter (0.125 cm^3)	Medium sensitivity, depending on the size of the active volume	High precision and instant readout	Calibration, output factor measurements, water tank measurements, acquisition of data for planning, QA, absolute dose point in IMRT verification.
Parallel-Plate Ionisation Chamber	Roos chamber: active volume 15 mm diameter and 2 mm depth (0.35 cm^3)	Medium sensitivity, depending on the size of the active volume	High precision and instant readout	High accuracy in surface dose measurements, with thin window and characterising electron beams.

Table 2.1
Summary of dosimeters in terms of size, sensitivity, accuracy, and important applications

2.8 Current Research Status of Out-of-Field Dose

Radiotherapy treatment planning systems (TPS) are not commissioned or designed for out-of-field dose calculations [44]. Although TPS can display the dose at points far from the treatment field, they are not utilised for calculating the out-of-field dose as extensive discrepancies have been reported between measured doses and those calculated from photon-beam planning systems [45–48]. Photon-beam planning systems have been reported to underestimate the true out-of-field dose [42, 45, 48]. The error in the planning system is due to the underestimation and non-consideration of patient scatter and head leakage and substantial underestimation of collimator scatter [48]. Therefore, most planning systems do not accurately model photon or electron leakage/scatter from the LINAC head.

Previously, there have been numerous studies completed on out-of-field dose to fetus and OARs. Numerous options and variations of treatment sites have been looked at using 3D-conformal radiotherapy and IMRT. Several analytical and Monte Carlo models have been developed for the calculation of out-of-field dose.

2.8.1 Analytical Models for Estimating Out-of-Field Dose

There are several different analytical models available for the calculation of out-of-field dose. Report of AAPM Radiation Therapy Committee Task Group No.36 [9] used data from the fetal dose from radiotherapy with photon beams in combination with mathematical phantoms to determine the out-of-field dose to different organs in a patient. Another study by Van Der Giessen (2001) [49] developed a software program called Peridose. This software was developed to calculate the dose outside the primary beam in radiation therapy. The program allowed the easy calculation of the peripheral dose in patients who were treated with megavoltage photon radiation. Within its constraints and

limits, this program allowed a fairly accurate estimation of the dose at any point outside the treatment area [49].

Furthermore, a study by Stovall et al. (2006) [50] developed an analytical model to be used for dose calculations. Three techniques were used to estimate doses from external beam radiation therapy: (1) calculations in three dimensional mathematical computer models, (2) measurement in anthropomorphic phantoms and (3) calculation using a three-dimensional treatment planning computer. The study described and compared these methods of dose estimation and discussed uncertainties in estimated organ doses and potential for future improvement. Exponential expressions for out-of-field dose as a function of distance from central axis and depth for both conventional and IMRT treatments have been proposed by Kry et al. (2005) [25] and Taddei et al. (2013) [51], however the accuracy of such simple expressions was found to be relatively poor and limited to conventional fields. Generally, the currently available analytical models are all limited to conventional fields and do not consider more sophisticated delivery techniques such as IMRT and VMAT.

2.8.2 Monte Carlo Methods for Estimating Out-of-Field Dose

Monte Carlo methods are very precise methods for calculating out-of-field dose with a well-accepted model. Monte Carlo calculations differ from analytical models as they use the interaction models of particles to predict the path of radiation on a particle by particle basis, giving an overall result of a radiation beam after many iterations. An accurate Monte Carlo model should include the intricate details of the LINAC head geometry to ensure that leakage radiation, collimator scattered radiation, and scattered radiation during high-energy photon therapy are appropriately modeled.

Monte Carlo codes that have been used to estimate out-of-field dose include MCNP5/MCNPX

code which was developed by Hughes et al. (1997) [52, 53], Geant4 code which was developed by Agostinelli et al. (2003) [54] and EGSnrc code which was developed by Kawrakow et al. (2000) [55]. Geant4 code is superior in terms of the physics modeling as it can track heavy ions as well as geometry definitions in 3 dimensions and even 4 dimensions. EGSnrc code tracks solely photons and electrons and is well suited for many radiotherapy applications as it has been validated for out-of-field dose applications more widely than any other photon/electron Monte Carlo codes. The main difference between these codes is the variations in the physics modeling, cross section data, transport mechanisms and the logistics of the model. Each code is unique and possess several advantages for its use.

A study by Kry et al. (2006) [26] developed a Monte Carlo model to calculate the out-of-field dose. The Monte Carlo code used was MCNPX where simulations of the out-of-field dose were made. Measurements were obtained in this study to validate the Monte Carlo model. The study found that the average local difference between the out-of-field doses calculated by the model compared to these measured was only 16%. This included a range of low doses, at distances in greater than 50 cm from the central axis of the treatment field. The out-of-field dose was seen to vary with field size and distance from the central axis. The Monte Carlo model developed by Kry et al. (2006) [26] was found to adequately represent a typical Varian 2100 accelerator operated at 6 MV.

Another study by Kry et al. (2007) [56] developed a Monte Carlo model to calculate the out-of-field dose from high energy photon therapy. In this study Kry et al. (2007) expanded and validated their previous Monte Carlo model for high energy 18 MV photon therapy, including both photons and neutrons. Simulations of out-of-field high energy photon doses were compared with measurements. The average local difference between the calculated and measured photon dose was 17%, including a range of low doses. The

out-of-field photon dose was seen to vary with field size and distance from the edge of the field. The average difference between the calculated and measured neutron fluence was 19% and agreed well with observed neutron spectra. On the other hand, the neutron dose changed little with field size or distance from the central axis. Neutrons were the dominant component of the out-of-field dose equivalent for shallow depths and large distances from the edge of the treatment field. This Monte Carlo model was found to be useful for both physicists and clinicians when assessing out-of-field doses and potential risks.

A study by Bednarz and Xu (2009) [57] developed a Monte Carlo model to calculate the in-field and out-of-field dose. This model was developed to understand and better measure non-target doses due to scatter and leakage radiation from medical accelerators. MCNPX code was used to develop the Monte Carlo model which defined over 100 accelerator components. Out-of-field doses were calculated and compared to measured data for both beam energies for field sizes of 4 cm x 4 cm, 10 cm x 10 cm and 20 cm x 20 cm. For all the field sizes considered in this study, the average local difference between calculated and measured dose for 6 MV and 18 MV beams was 14% and 16% respectively. The study further determined a method for calculating neutron contamination in the 18 MV model by comparing the calculated in-air neutron fluence with reported calculations and measurements. The average difference between calculated and measured neutron fluence was 20%. As one of the most detailed accelerator models, this Monte Carlo model has been combined with anatomically realistic computational patient phantoms into a computational framework to calculate non-target organ dose to patients from various treatment plans.

Overall, the Monte Carlo models developed by Kry et al. [26, 56], Bednarz and Xu [57] have shown good agreement with measurements beyond 50 cm from the field edge.

Simpler models that include only beam-line components have been used by Joosten et al. (2011) [46] and Almberg et al. (2012) [58]. The study by Joosten et al. (2011) [46] developed a simple Monte Carlo for both open and wedged fields that were validated with dose profiles measured in a water tank up to 30 cm from central axis. It was found that differences between measured and calculated doses were comparable to other more complex models and never exceeded 50%. The study by Almberg et al. (2012) [58] developed a simple Monte Carlo model using the EGSnrc code, where photon simulations and dose calculations in a water tank were made. The study found that the out-of-field dose for regions up to 20 cm from central axis will reduce by 10%-30% compared to the linear accelerator operating with a flattening filter. The two simple models developed by Joosten et al. [46] and Almberg et al. [58] have been noted to be capable of accounting for the patient scatter outside the treatment field, however, they do not allow for proper modeling of head leakage and collimator scatter. For beam-line models, good accuracy can be achieved out to approximately 15 cm from the field edge beyond this accuracy becomes increasingly poorer.

To develop a model that will predict the doses to the organs of interest and perform the calculations for the region is a difficult process that requires a lot of time and effort. This model may also only be useful for only one region of interest as it complicated to consider other regions and sites. There are techniques to minimise non-target dose by using others forms of treatment, changing MLC and collimator orientation, using low energy treatment options and providing patient shielding.

Chapter 3

Experimental Challenges and Principles of Measuring Out-of-Field Dose

The measurement of out-of-field dose presents many challenges, which are related to choice of the detector. The choice of an ionisation chamber for measurements was based on the high sensitivity, high signal to noise ratio and high spatial resolution of the chamber, for dose profile and depth-dose measurements. The first challenge in out-of-field dose measurements was the extremely low signal out-of-field. A Roos chamber was used for near surface depth dose measurements since the 0.6 cm^3 ionisation chamber could not measure depths as low as 1 mm. A waterproof 0.6 cm^3 cylindrical chamber was used inside a water tank for dose profile and depth-dose measurements since it has a larger volume and therefore higher sensitivity than the Roos chamber. Long scanning times and stray radiation reaching the cable was another challenge. The difficulty associated with setting up the water tank and fitting the water tank close to the gantry and out of the primary beam was a challenge. The implications of these challenges with dose profile and depth-dose measurements with a cylindrical ionisation chamber and a Roos parallel plate ionisation chamber resulted in a need for a detailed uncertainty analysis.

An uncertainty associated with a measurement is a parameter that characterises the dispersion of the values and can be separated into two components based on the origin of the sources of uncertainty, namely a random component (type A) and a systematic component (type B) [59].

3.1 Experimental Uncertainties: Type A Uncertainties

Type A uncertainties are attributed to random errors. The method of Type A uncertainties is based on statistical analysis of a series of observations, it is the standard deviation based on the short-term reproducibility. Type A uncertainties are able to be picked up by repeated measurements. One way of reducing the effect of randomness is to take a large number of readings and calculate the average. Statistically, this is reducing the standard deviation of the mean by increasing the sample size. Random uncertainty can never be eliminated completely, therefore a statistical model can be used to estimate them [60].

3.2 Experimental Uncertainties: Type B Uncertainties

Type B uncertainties are attributed to systematic errors. The method of type B uncertainties is not based on a statistical analysis of a series of observations, it is an uncertainty estimate due to all other factors which are difficult to quantify. Therefore, the sources of measurement uncertainties that cannot be estimated by repeated measurements are called type B uncertainties. These include not only unknown influences on the measurement process but also little known effects of influence quantities such as variations in pressure, temperature, etc. In this case, type B uncertainties could include setup reproducibility and accuracy, spectral changes under varying conditions, uncertain electron/photon mix at shallow depths, stability of the electrometer response, for example

drift in dark current during measurements (especially because of the low dose rate leading to low current pA instead of the usual nA, in spite of frequent zeroing of the electrometer), changes in temperature and pressure between calibration and measurement conditions, linac output variation with time (due to very long beam on times), chamber characteristics such as stem effect or poor venting and positioning uncertainties. Improving the quality of equipment can reduce the systematic uncertainty, however, it can never be completely eliminated [60].

3.3 Combination of Type A and Type B Uncertainties

The combination of type A and type B uncertainties gives the total expanded uncertainties as type A and type B uncertainties are both estimated standard deviations. The combination of type A and type B uncertainties is given by combining the variances, such that if u_A and u_B are the type A and type B standard uncertainties of a quantity, respectively, the combined standard uncertainty of that quantity is:

$$u_c = \sqrt{u_A^2 + u_B^2}$$

The addition of type A and type B uncertainties in quadrature results in the total uncertainty [59]. This has been performed for each chapter in this study.

3.4 Uncertainty Estimate for Measurements

An error analysis was completed for this study which consists of experiments within solid water blocks, within liquid water tanks and on an anthropomorphic phantom.

Depth dose measurements in solid water involved recording the dose at the surface. The type A and type B uncertainties within the experiment were accounted for in the

error analysis. The type A uncertainties were random errors which were accounted for by taking the standard deviation of the point dose measurements.

Type B uncertainties within the experiment were systematic errors which included the reproducibility of the set-up. Uncertainties may have resulted from the very low output signals measuring the out-of-field dose. Measurements were taken with a Roos chamber since it had a good spatial resolution in the depth direction and a good signal to noise ratio. A Roos chamber also has a small inherent effective depth of measurement.

Characteristics that were necessary for the depth dose measurements in solid water were a detector that had a good spatial resolution in the depth direction. Hence, a Roos chamber was used with a very long integration time in solid water, with only 1 mm of inherent material. This was essential in order to have an accurate characterization of the near surface dose. Therefore, the uncertainties for the solid water measurements were calculated by the addition of type A and type B uncertainties in quadrature, which results in the total uncertainty for each individual graph.

For the dose profile and depth dose measurements and the VMAT patient plan scans, type A and type B uncertainties were accounted for in the error analysis. The type A uncertainties within the experiments were random uncertainties which were extremely small and therefore insignificant to be recorded. For the depth dose measurements, a waterproof 0.6 cm^3 cylindrical chamber was selected for measurements since it had a high sensitivity and a good signal to noise ratio.

Initially, a 0.125 cm^3 cylindrical and Roos chamber were used for the water tank scans however, this was very challenging due to the low signal measuring a current of pA. The 0.125 cm^3 cylindrical and Roos chamber had a very low signal to noise ratio and there-

fore were not useful for the water tank scans. Hence, a 0.6 cm^3 cylindrical chamber was used instead with 1 second integration time in each position compared to the normal 0.1 second integration time in-field. The very long integration times in the water tank resulted in each scan being up to 20 minutes long, this may have contributed to error, as this increases the amount of stray radiation reaching the cables.

Therefore, the uncertainty estimate for the dose profile and depth-dose measurements were determined from the addition of type A and type B uncertainties in quadrature, which resulted in the total uncertainty for each of the measurements. The type B uncertainties were determined to be 3% for one standard deviation (6% to within 95% confidence interval), which contributed to the total uncertainty for each of the measurements.

For the anthropomorphic phantom VMAT measurements, a 0.6 cm^3 cylindrical chamber was used because of its minimal angular dependence around the azimuth and a good signal to noise ratio. The disadvantage of this chamber is that its geometry is not good for near surface measurements. To determine how much build-up material was needed to get the right effective depth, a comparison of the Roos and 0.6 cm^3 cylindrical chamber at shallow depths was done to compare the near surface dose. The comparison showed reasonable agreement, which was sufficient for the purposes of the anthropomorphic phantom VMAT measurements.

To compare the results with the surface dose the electron density of the wax material was used to calculate the water equivalent depth in wax. Water equivalent depth was determined using the effective atomic number ($\overline{Z}$). Effective atomic number ($\overline{Z}$) is the atomic number of an element with which photons interact with the same way as with the given composite material. The interaction of photons, with the photoelectric effect is highly dependent on the atomic number (Z) of an absorbing material. Therefore,

the effective atomic number ($\overline{Z}$) is considered for photoelectric interactions. Mayneord defined the effective atomic number of a compound as below [10]:

$$\overline{Z} = (a_1 Z_1^{2.94} + a_2 Z_2^{2.94} + a_3 Z_3^{2.94} + ... + a_n Z_n^{2.94})^{1/2.94}$$

Where $a_1, a_2, a_3, ..., a_n$ are the fractional contributions of each elements to the total number of electrons in the substance.

Example 1. Calculation of Effective $\overline{Z}$ for Wax: $C_{25}H_{52}$

Total number of electrons in Wax = (1 $\times$ 52) + (6 $\times$ 25) = 202

$$\overline{Z}_{wax} = \left(\frac{1 \times 52}{202} \times 1^{2.94} + \frac{6 \times 25}{202} \times 6^{2.94} \right)^{1/2.94} = 5.43$$

Water Equivalent Depth:

Using the electron density (ρ) of the wax material, the water equivalent depth in wax was calculated. This is shown below:

$$Depth_{Eff} = depth \times \frac{\rho_{wax}}{\rho_{water}} \times \frac{\overline{Z}_{wax}}{\overline{Z}_{water}}$$

$$Depth_{Eff} = depth \times \frac{0.92}{1} \times \frac{5.43}{7.42}$$

Therefore, the uncertainty estimate for the anthropomorphic phantom VMAT measurements were determined from the addition of type A and type B uncertainties in quadrature, which resulted in the total uncertainty for each of the measurements.

	Type of quantity or procedure	**Uncertainty Type A or Type B**	**Uncertainty (%)**
1	Random Errors (point dose measurements)	Type A	$<1\%$
2	Reproducibility of setup	Type B	3%
3	Spectral changes in photon component	Type B	2%
4	Electron/photon mix at shallow depths	Type B	3%
5	Signal to noise ratio due to low signal and long integration times causing drift in dark current	Type B	4%
6	Changes in temperature and/or pressure	Type B	1%
	Total Uncertainty	$\sqrt{\sum \textbf{Uncertainty}^2}$	**6**$\%$

Table 3.1
Estimated combined Type A and Type B uncertainty to (1σ) for dose profile, depth-dose and anthropomorphic phantom VMAT measurements using an ionisation chamber.

The type A and type B uncertainties have been explicitly separated and listed Table 3.1. The calculation for the 6% uncertainty has been explained in the last row of the table and this value has been referenced where relevant.

Chapter 4

Depth-Dose Measurements of Out-of-Field Radiation

As the beam is incident on a patient (or phantom), the absorbed dose in the patient varies with depth. This variation depends on many conditions: beam energy, field size, distance from source and beam collimation system. The calculation of the out-of-field dose in the patient involves considerations in regard to these parameters and others as they affect depth dose distribution. Hence, an essential part in the dose calculation system is to establish depth dose variation away from the central axis of the beam.

In this chapter, depth-dose measurements at extremely shallow depths will be investigated, since the sensitive region of the eye lens is as shallow as 2.8 - 3.8 mm [2] and CIEDs are inserted just beneath the skin at depths between 5 - 10 mm. The aim of this chapter is to investigate the dose at shallow depths, with varying field sizes and to investigate the suitability of the parallel plate chamber for characterization of out-of-field measurements.

4.1 Materials

Dose measurements near the surface require good spatial resolution in the depth direction, therefore a parallel plate chamber must be used. For this reason we used the ROOS ionisation chamber. A PTW UNIDOS® Electrometer was set at low range, current mode and a bias voltage of 150 V to record the charge in nC range. Solid water sheets were used as scatter material for the detectors. Ainsworth dental wax with a density of 0.92g/cm^3 was used as additional build up material for the detectors.

4.2 Methodology

4.2.1 Part I: Calibration of the Photon Beam

The first part of the experiment involved calibrating the output of the photon beam with the Roos ionisation chamber, in solid water. In order to generate the calibration coefficients for the Varian Clinac iX linear accelerator, a 6 MV beam was applied. The Varian Clinac iX linear accelerator was set to reference conditions: gantry angle 0°, collimator angle 0°, FSD = 100 cm, 10 cm x 10 cm field size and MLCs retracted. The Roos chamber was connected to a power supply, set at a voltage of 150 V, with a PTW UNIDOS® T10001-11678 electrometer measuring the capacitor charging current. The Roos chamber was placed at isocentre and 100 MU was delivered to the chamber in solid water at an effective depth of d_{max} = 15 mm. The chamber calibration coefficients were essential to convert the reading measurements from charge (pC) to dose (μGy/MU) in non-reference conditions.

4.2.2 Part II: Quantification of couch scatter

Due to the very low signal from head leakage and collimator scatter, it was essential to minimise any scatter coming from objects in the primary radiation field, therefore there should be no material directly in the path of the beam for these measurements. In order to place the detectors at clinically relevant positions to measure the dose at the eye lens and the upper chest, it was necessary to place the detectors and their associated solid water phantoms out of field and at the appropriate locations between the gantry and the edge of the beam. This could be achieved by having the couch out of the primary field i.e. fully retracted or rotated to 90° and offset towards the gantry, but it was more convenient to have the phantoms supported on the gantry end of the couch while the couch was still at 0° and therefore in the primary beam. For the latter case, it was important to examine the extent of the contribution of scattered dose coming from the couch as there was a risk of the couch generating in-field scatter. To test this, out of field measurements were performed in solid water with the couch in-field (couch angle 0°). The measurements were then repeated without the couch in the field (couch angle 90°). Measurements were taken at gantry angle 0° and 180°, with the collimator at 90° at four different field sizes of 2 cm x 2 cm, 5 cm x 5 cm, 10 cm x 10 cm and 20 cm x 20 cm. The MLCs were kept at 40 cm x 40 cm at all times.

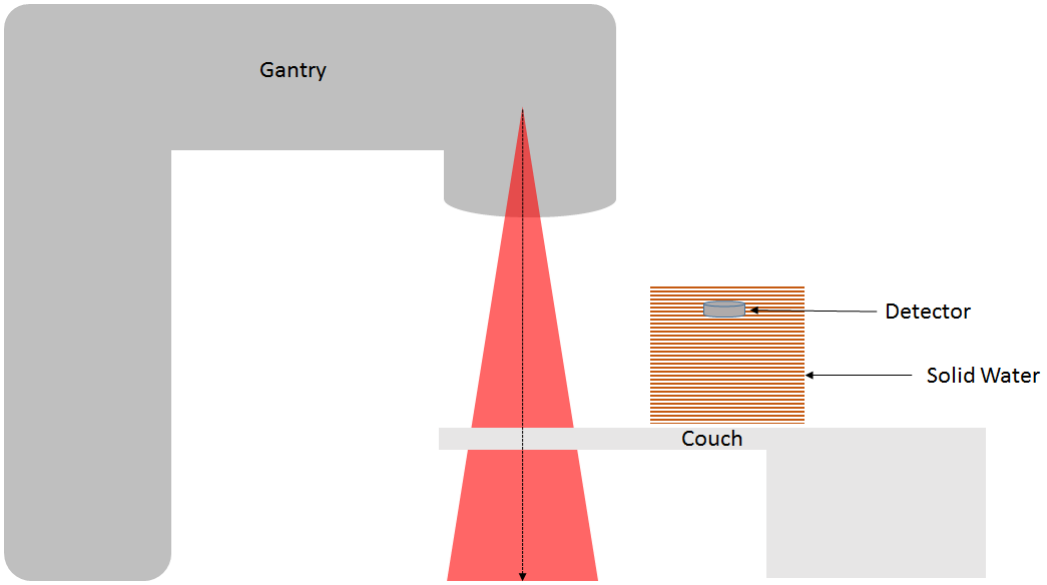

Figure 4.1 Quantification of couch scatter: couch in primary field

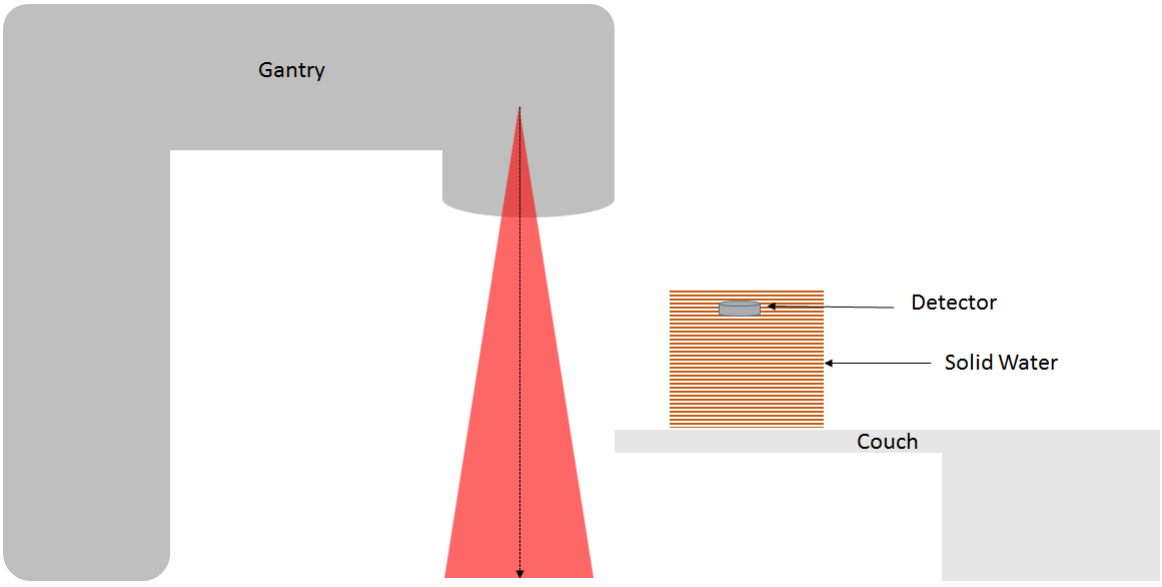

Figure 4.2 Quantification of couch scatter: couch out of primary field

4.2.3 Part III: Depth Dose Measurements with Roos Chambers

Measurements for the out-of-field depth dose were performed using two Roos parallel plate ionisation chambers. The Roos chambers and their associated solid water phantoms were placed out of field and at their appropriate locations between the gantry and the edge of the beam to simulate prostate treatments. One of the chambers was placed at 76 cm from central axis which represented the location of the eye lens and the other was placed 52 cm from central axis which represented the location of chest where the CIED would be situated on a patient.

Due to there being only one slab of solid water with a cavity for the Roos chamber, this cavity was used to place the chamber at the location of the chest. For the location of the eye lens, a cavity was made in a gelatin slab to fit the Roos chamber. It was vital for the gelatin to be shaped accordingly, as a lack of side scatter would result in incorrect measurements. Each Roos chamber has a front window of 1 mm PMMA, which is equivalent to 1.3 mm of water. Additional layers of wax were added on top of the chambers to increase the depth of measurement for each separate configuration. The out-of-field measurements were taken at gantry zero, at three different field sizes: 0.5 cm x 0.5 cm, 10 cm x 10 cm and 20 cm x 20 cm. The MLCs were retracted at 40 cm x 40 cm at all times. The position of the Roos chambers can be seen in Figure 4.3 and Figure 4.4.

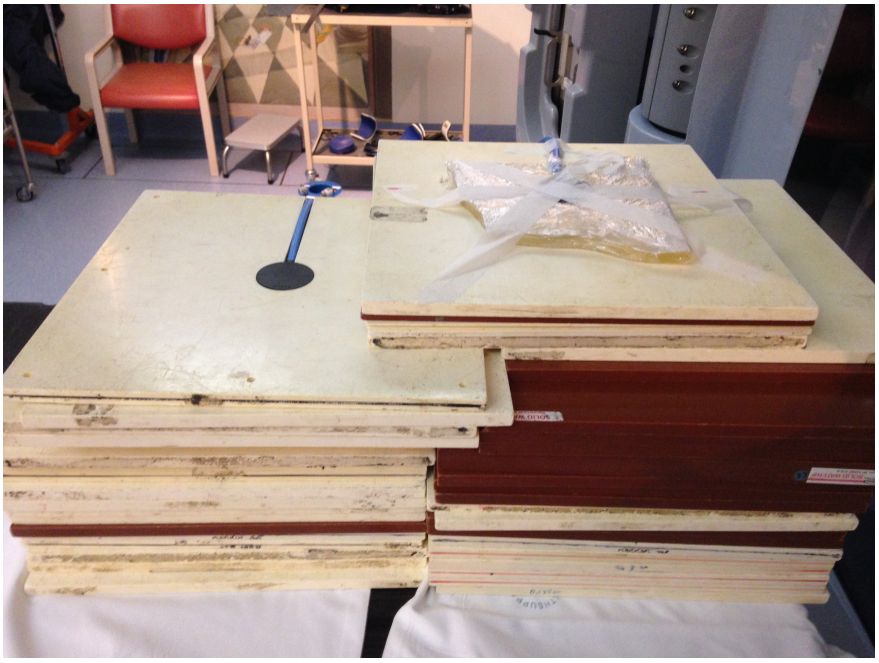

Figure 4.3 Experimental set-up of Roos chambers

Figure 4.4 Experimental set-up of Roos chambers in relation the gantry

4.3 Results

4.3.1 Part II: Quantification of couch scatter

Table 4.1 below quantifies the contribution of the couch scatter by having the couch in the primary field or out of the primary field for varying field sizes. The readings below show the percentage of increase or decrease between the average readings.

Field size	**Gantry Angle**	**Couch in Primary Field (pC)**	**Couch out of Primary Field (pC)**	**%Difference**
2cm x 2cm	0°	4.69±0.14	4.71±0.14	+0.3%
5cm x 5cm	0°	4.84±0.15	4.91±0.15	+1.6%
10cm x 10cm	0°	5.69±0.18	5.91±0.18	+3.9%
20cm x 20cm	0°	9.76±0.29	9.96±0.30	+2.4%
2cm x 2cm	180°	1.22±0.04	1.15±0.03	−5.7%
5cm x 5cm	180°	1.72±0.05	1.63±0.06	−5.2%
10cm x 10cm	180°	3.46±0.10	3.37±0.10	−2.5%
20cm x 20cm	180°	10.59±0.32	10.47±0.31	−1.1%

Table 4.1 Quantification of couch scatter. Average difference = 0.8%

By examining the quantification of the couch scatter, having the couch in the primary field or out of the primary field shows a small change in the readings. As the average difference in the readings is less than 1%, it can be concluded that the contribution to the scattered dose is small. Therefore, it is acceptable to have the couch either in the primary field or out of the primary field. The small discrepancies are most likely due to random errors in replicating the set up with and without the couch.

4.3.2 Part III: Depth Dose Measurements with Roos Chamber

Out-of-field depth dose measurements, using a Roos chamber, with varying field sizes: 0.5 cm x 0.5 cm, 10 cm x 10 cm and 20 cm x 20 cm at the location of the eye lens are

show in Figure 4.5 and at the location of the location of the chest Figure 4.6.

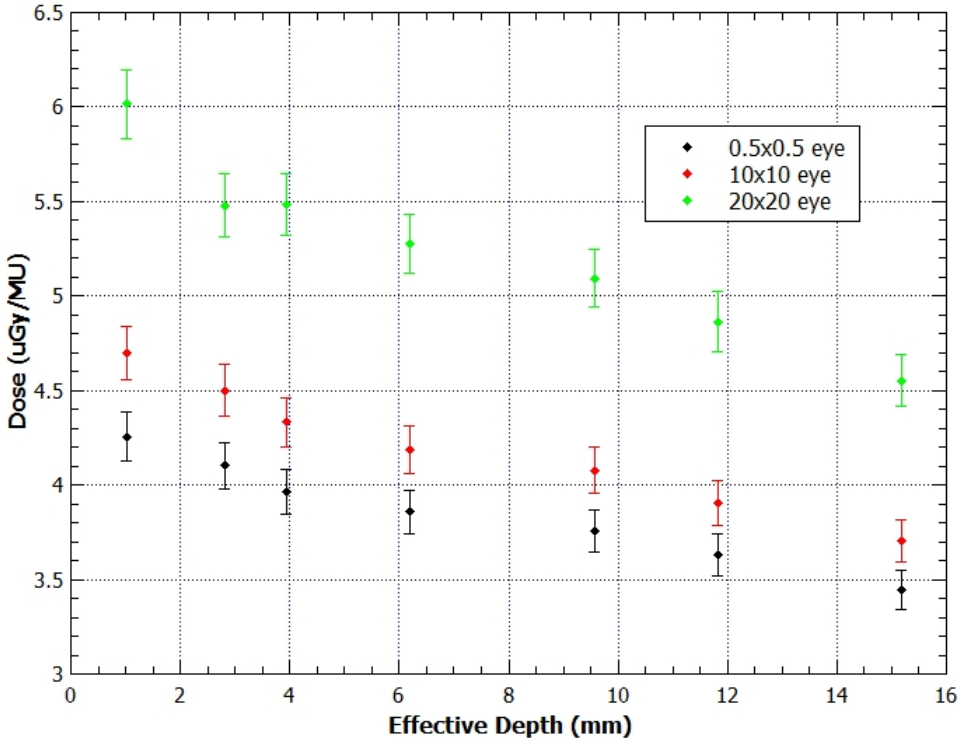

Figure 4.5 Out-of-Field Depth Dose using Roos chamber, at the location of the eye lens, with 0.5 cm x 0.5 cm, 10 cm x 10 cm and 20 cm x 20 cm field sizes.

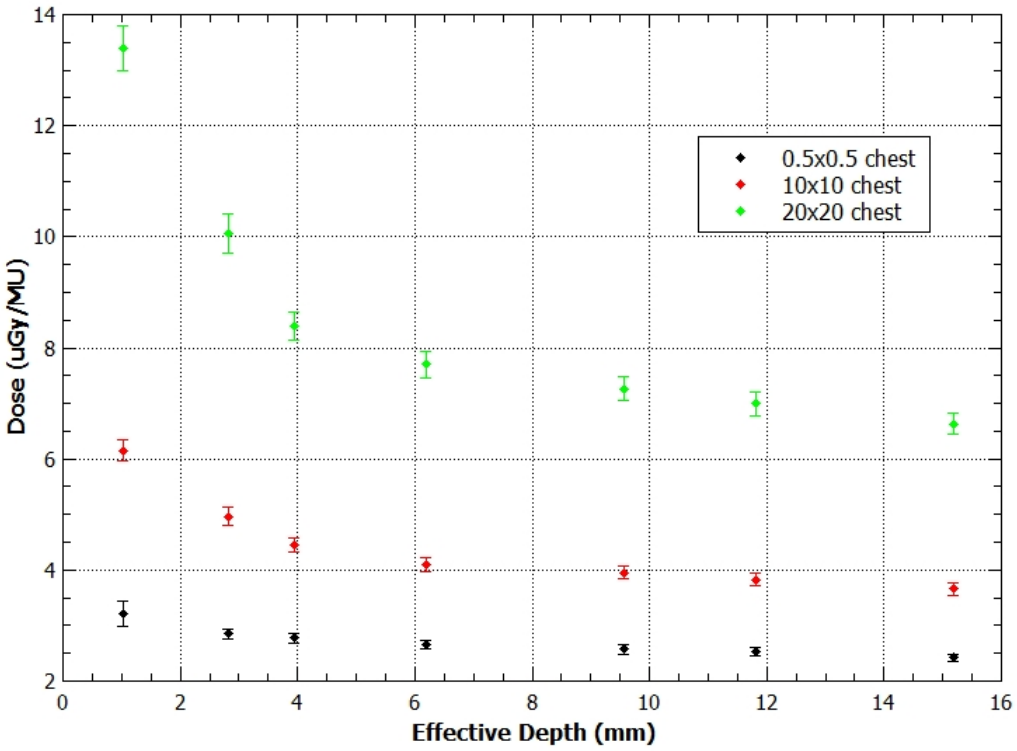

Figure 4.6 Out-of-Field Depth Dose using Roos chamber, at the location of the chest, with 0.5 cm x 0.5 cm, 10 cm x 10 cm and 20 cm x 20 cm field sizes.

Both Figure 4.5 and 4.6 show the larger the field size the greater the out-of-field dose. The dose is seen to be greatest at the shallowest region 1 mm and then it is seen to be decreasing slightly as the effective depth of measurement increases.

Figures 4.7, 4.8 and 4.9 compare the out-of-field depth dose, using a Roos chamber, with the same field size, at the location of the eye lens and chest.

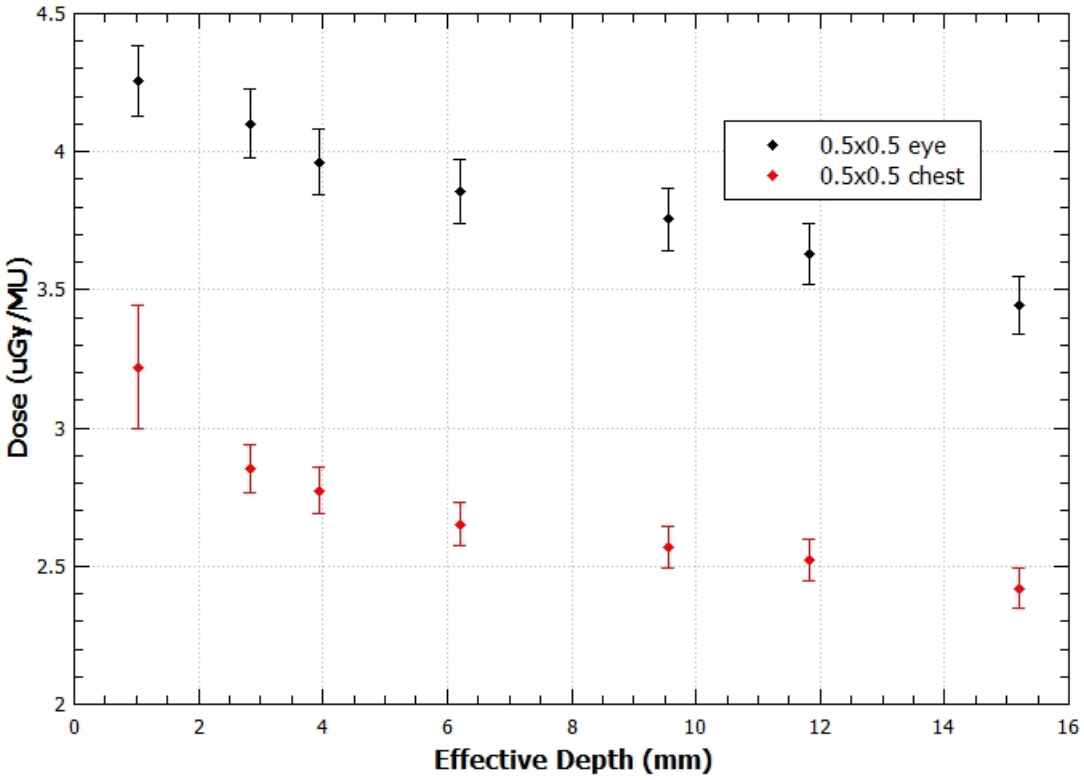

Figure 4.7 Out-of-Field Depth dose using Roos chamber, at the location of the eye lens and chest with 0.5 cm x 0.5 cm field size.

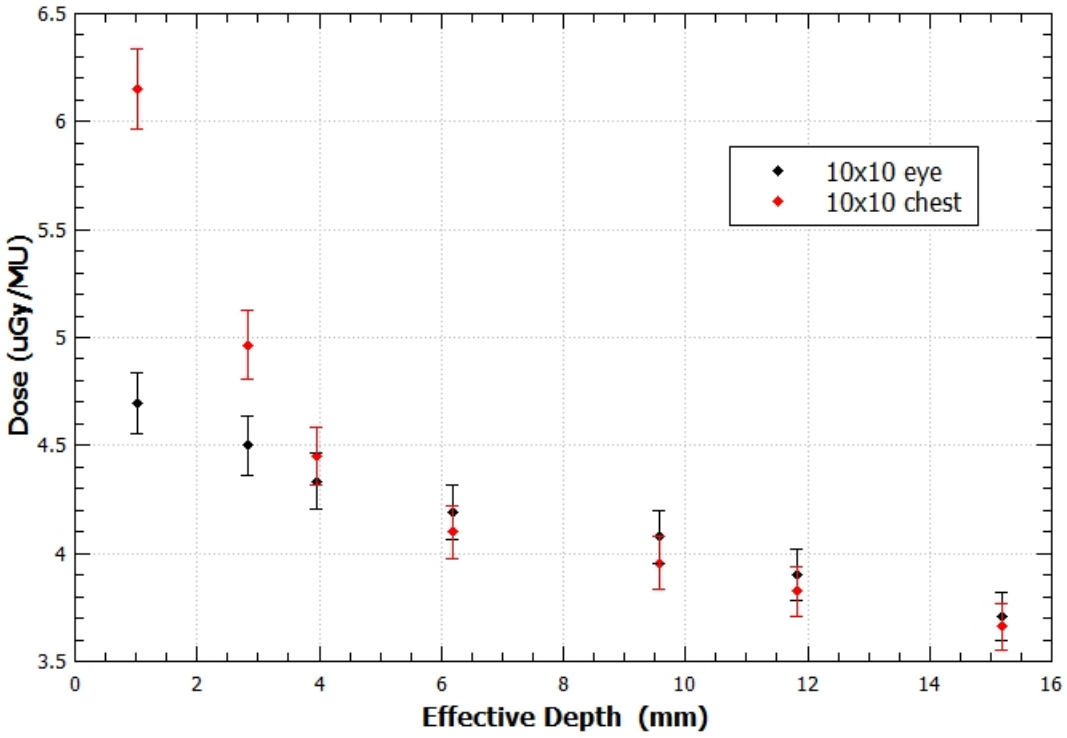

Figure 4.8 Out-of-Field Depth dose using Roos chamber, at the location of the eye lens and chest with 10 cm x 10 cm field size.

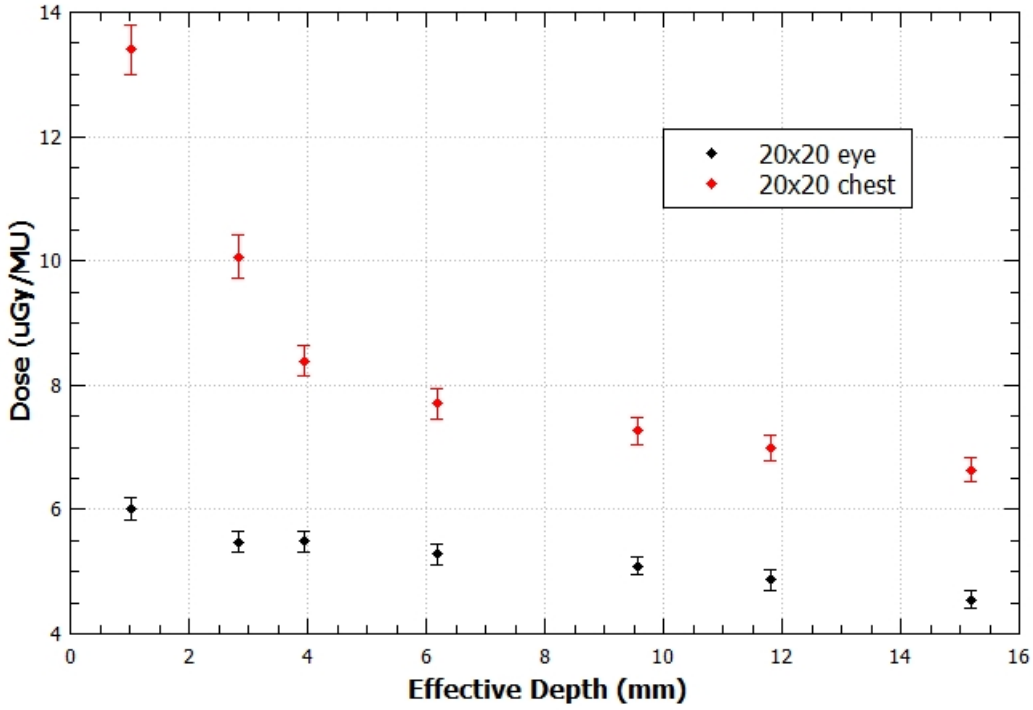

Figure 4.9 Out-of-Field Depth dose using Roos chamber, at the location of the eye lens and chest with 20 cm x 20 cm field size.

4.4 Discussion/Conclusion

Firstly, the quantification of the couch scatter was examined for a gantry angle of 0° and 180°, with field sizes of 2cm x 2cm, 5cm x 5cm, 10cm x 10cm and 20cm x 20cm. It was concluded that having the couch in the primary field or out of the primary field had minimal effect on the scattered dose. The average difference of 0.8% is minimal, but the individual differences between the same field sizes are not. Small discrepancies were due to systematic errors in replicating the set up with and without the couch, as well as possible changes in testing conditions i.e. pressure, temperature.

The out-of-field depth dose measurements, with the Roos chamber in solid water at the location of the eye lens and chest, with the field size of 0.5cm x 0.5cm, 10cm x 10cm and 20cm x 20cm were examined. The depth dose curves showed the dose to be greater near the surface. For the smaller field size of 0.5cm x 0.5cm the dose to the eye lens was greater than the dose to the chest. For the 10cm x 10cm field size, the dose to the chest was greater than the dose to the eye lens until 6 mm where the dose to the eye lens became greater than the dose to the chest. The cross over in the dose distribution is likely due to there being more attenuation of the beam by the shielding components in the LINAC head in the direction of the chest, combined with a higher surface dose from the scattered electrons or low energy photons at the chest. For the larger 20cm x 20cm field size, the dose to the chest was significantly greater than the dose to the eye lens. This was primarily due to the larger area of jaw surface that can scatter radiation outside the primary beam, thus increasing the out-of-field dose. Overall, the depth dose curves displayed the dose to be greater for larger field sizes such as 20cm x 20cm and 10cm x 10cm, with a decreasing trend as the effective depth of measurement increases.

In conclusion, the Roos chamber was able to successfully measure the low signal (pC)

dose at shallow depths, with varying field sizes. The Roos chamber had a good spatial resolution in the depth direction, which was found to be precise and effective at measuring the out-of-field dose.

Chapter 5

Characterisation of Out-of-Field Dose Components

The measurement of non-target photon dose outside the treatment field poses many unique challenges as the radiation is different outside the treatment field. Based on the characteristics of the radiation field outside the target volume, general measurement considerations are warranted. The aim of this chapter is to characterise the out-of-field dose components and to examine the relative contributions of leakage and the two components of scatter.

5.1 Materials

Dose profile and depth dose measurements were taken in 60 cm x 50 cm x 40.8 cm motorised water tank, which was accompanied with a PTW MP3 system software, connected to a PTW UNIDOS® Electrometer, with MEPHYSTO® mc^2 software. The MEPHYSTO® mc^2 software scan parameters were set to obtain optimal results. The scans were taken on low range setting, SSD of 90 cm, gantry 0°, speed 10mm/s, steps starting from 2 mm at around 170 mm from central axis up until 300 mm from central

axis, to obtain optimal precision and 20 mm steps at 300 mm up until around 750 mm from central axis. A dwell time of 1 sec was set at each position which had to be much longer than for the in-field measurements (generally 0.1 s).

Out-of-field dose profile and depth dose measurements required a detector with a high sensitivity and minimal angular dependence for measuring very low dose in pC. A 0.6 cm^3 waterproof cylindrical ionisation chamber (PTW FREIBURG, TM31010) was used to obtain dose profile and depth dose measurements. The dose profile and depth dose measurements were recorded with the water tank electrometer which can only provide relative ionisation values. In order to be able to convert the profiles and depth dose measurements to dose/MU, they were normalised using point dose measurements carried out in solid water with a detector/electrometer combination whose sensitivity was determined through exposure under reference conditions. A PTW UNIDOS® Electrometer was set at low range, current mode and a bias voltage of 150 V to record the charge in pC. Solid water sheets were used as build-up material for the detectors. An anthropomorphic pelvis phantom was used as scatter material for the dose profile and depth dose measurements.

5.2 Methodology

5.2.1 Part I: Calibration of the Photon Beam

The first part of the experiment involved calibrating the output of the photon beam with the 0.6 cm^3 ionisation chamber, in solid water. In order to generate the calibration coefficients for the Varian Clinac iX linear accelerator, a 6 MV beam was applied. The Varian Clinac iX linear accelerator was set to reference conditions: gantry angle 0°, collimator angle 0°, Focus to Source Distance = 100 cm, 10 cm x 10 cm field size

and MLCs retracted. The 0.6 cm^3 cylindrical ionisation chamber (PTW FREIBURG, TM31010) was connected to a power supply, set at a voltage of 150 V, with a PTW UNIDOS® T10001-11678 electrometer measuring the capacitor charging current. The 0.6 cm^3 cylindrical ionisation chamber was placed at isocentre and 100 MU was delivered to the chamber in solid water at an effective depth of d_{max} = 15 mm. The chamber calibration coefficients were essential to convert the reading measurements from charge (pC) to dose (cGy/MU) in non-reference conditions.

5.2.2 Part II: Comparison with Kry et al. (2006) Out-of-field Dose Profile Measurement

The aim of this section was to obtain out-of-field dose profiles that would reproduce the setup of Kry et al.(2006) [26] to verify our measurement methods. To reproduce the setup of Kry et al. (2006), out-of-field dose profile measurements were taken with a 0.6 cm^3 waterproof ionisation chamber (PTW FREIBURG, TM31010) inside a water tank. The dose profile measurements were performed at gantry angle of 0°, collimator angle 0° and 100 cm SSD. The chamber was positioned at a depth of 37.5 mm and 112.5 mm, 15 cm away from central axis up until 70 cm, with each subsequent dose measurement. Solid water sheets were placed under the beam to provide phantom scatter. The dose profile measurements were compared to the results of Kry et al.(2006) [26]. Experimental set-up can be seen in Figure 5.1.

Figure 5.1 Experimental set-up of out-of-field dose measurements, for comparison with the results of Kry et al. (2006) [26]

5.2.3 Part III: Clinically Relevant Out-of-Field Measurements

In this section, the water tank was positioned on the gantry side of the isocentre in order to represent the most realistic positioning of the patient with the head of the patient close to the gantry side. The out-of-field scans were taken with a waterproof 0.6 cm^3 ionisation chamber (PTW FREIBURG, TM31010) inside the water tank, 20 cm away from central axis up until 70 cm, at depths of 5 mm, 15 mm and 37.5 mm with each subsequent dose measurement. The source to water surface distance was set to 90 cm SSD.The following conditions were set as the reference conditions for all experiments:

1. Gantry at 0°
2. Collimator at 0°

3. Field Size: 10 cm x 10 cm

4. MLC Field Size: 10 cm x 10 cm

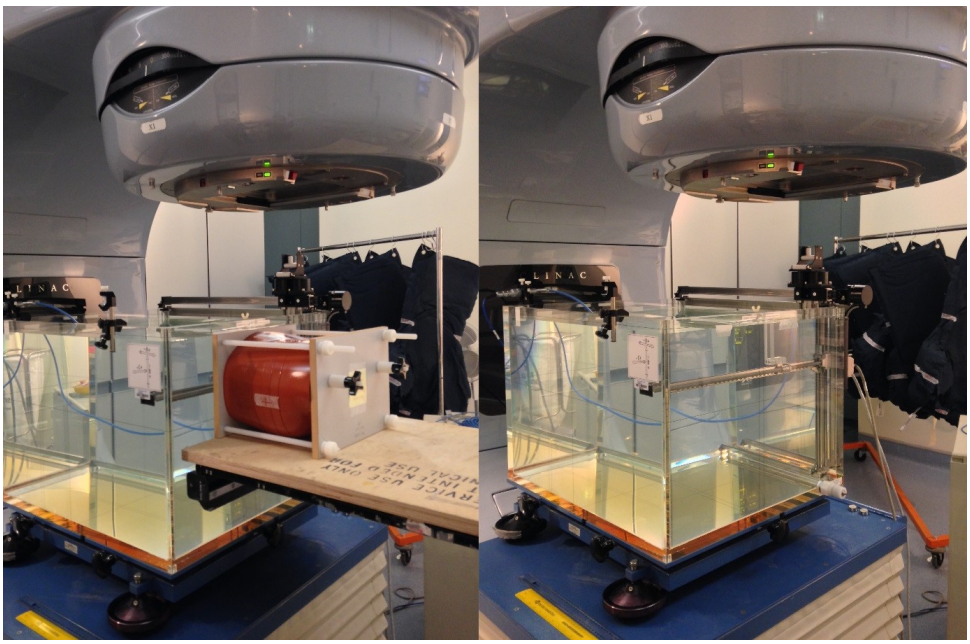

Figure 5.2 Experimental set-up of the out-of-field dose measurements, inside the water tank with/out the phantom scatter

To separate the individual dose contributions of head leakage (HL), collimator scatter (CS) and internal patient scatter (PS) the following experiments were performed.

5.2.3.1 Experiment 1: Total dose including Head Leakage (HL) + Collimator Scatter (CS) + Patient Scatter (PS)

The total dose of the scattered radiation from head leakage (HL), collimator scatter (CS) and internal patient scatter (PS), was obtained by performing clinically relevant scans at a gantry angle of 0°, at collimator angle 0°, 45° and 270°, field size of 10 cm x 10 cm and MLC field size of 3 cm x 3 cm, 6 cm x 6 cm and 10 cm x 10 cm.

An anthropomorphic pelvis phantom was placed directly under the treatment beam to provide phantom scatter. Separate scans were performed for each set of conditions, to compare the different collimator angles and MLC field sizes, at varying depths, with the presence of phantom scatter.

$$Total\ Dose = HL + CS + PS$$

5.2.3.2 Experiment 2: Head Leakage (HL) + Collimator Scatter (CS)

To measure the contribution of scattered radiation from head leakage and collimator scatter alone, the pelvic phantom was removed from isocentre, out of the treatment beam. The water tank was positioned relative to the isocentre. The beam did not pass through or interact with the water in the tank and therefore this eliminated the contribution of phantom scatter. The scans were performed at a gantry angle of 0°, at collimator angle 0°, 45° and 270°, field size of 10 cm x 10 cm and MLC field size of 10 cm x 10 cm. Separate scans were performed for each set of conditions, to compare the different collimator angles, at varying depths, without the presence of phantom scatter. The resultant scans only represented head leakage and collimator scatter.

5.2.3.3 Experiment 3: Phantom Scatter (PS)

To determine the contribution of phantom scatter, the scattered radiation from head leakage and collimator scatter was subtracted from the total dose of scattered radiation. The scans performed at a gantry of 0°, 45° and 270°, with field size of 10 cm x 10 cm and MLC field size of 10 cm x 10 cm, without the phantom scatter were subtracted from the scans with the phantom scatter. From this a higher uncertainty is created than the measurements alone. The addition of the uncertainty from the total dose of scattered radiation and the uncertainty in the scattered radiation from the head leakage and the collimator scatter, in quadrature gives the total uncertainty for the phantom

scatter. Therefore, the total uncertainty of the phantom scatter equals to 4.2% for one standard deviation (8.5% to within 95% confidence interval).

5.2.4 Part IV: Calibration of Dose Profiles and Depth Dose Measurements

To calibrate the dose profiles and depth dose curves, point dose measurements (Gy/MU) with a Roos chamber were taken to obtain the absolute dose measurements. The Roos chamber was positioned at the reference point of depth 5 mm and at a distance of 500 mm away from central axis, and it was connected to a UNIDOS® electrometer. One profile per set of conditions at depth = 15 mm and PDDs for all conditions (field size, MLCs, with/out phantom scatter) were obtained. Figure 5.3 and Figure 5.4 below show the positioning of the Roos chamber inside the water tank with and without the presence of phantom material.

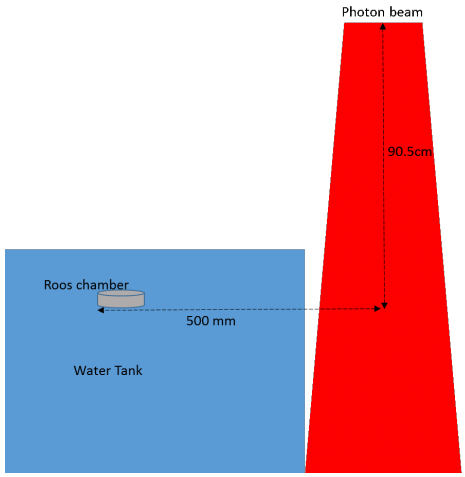

Figure 5.3 Roos chamber in solid water at depth 5 mm

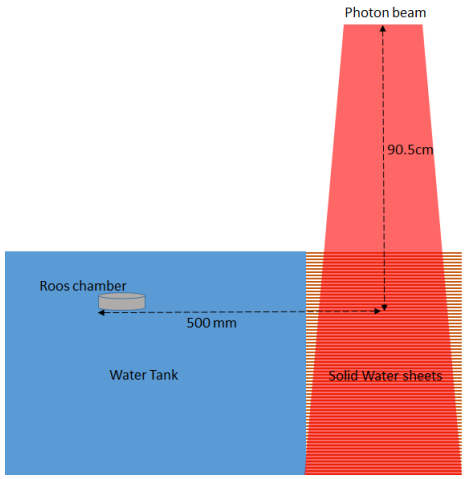

Figure 5.4 Roos chamber in solid water at depth 5 mm, with the presence of phantom scatter

5.3 Results

5.3.1 Comparison between Measurements and Kry et al. (2006)

Figure 5.5 below shows the out-of-field dose profiles from a 6 MV photon beam as a function of distance from the central axis, at depths of 3.75 cm and 11.25 cm. This figure combines the out-of-field dose measurements with the measured and Monte Carlo simulations from Kry et. al. (2006) [26]. The experimental results were normalised to obtain the absolute dose in μGy/MU. The absolute dose results showed good agreement with Kry's et al. (2006) measured and simulated Monte Carlo out-of-field doses. This agreement with published data verified that the measurements methods were appropriate.

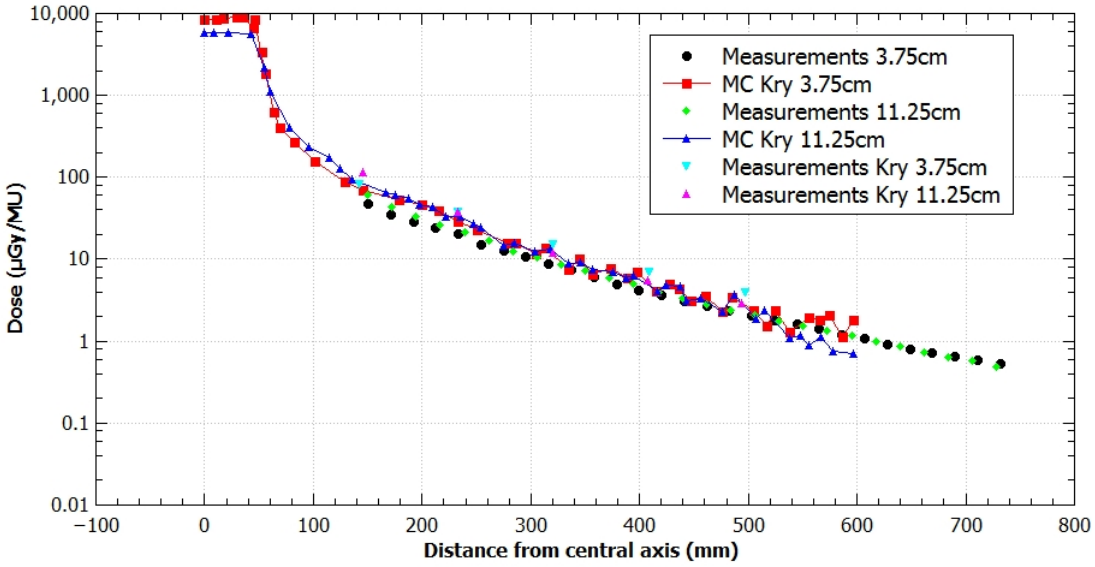

Figure 5.5 Out-of-field dose profile from 6 MV photon beam measurements as a function of distance from the central axis, at depths of 3.75 cm and 11.25 cm, compared to both measurements and Monte Carlo simulations from Kry et al. (2006) [26].

From the dose profile the out-of-field dose at 3.75 cm and 11.25 cm depth were superimposed at all distances from the central axis. Figure 5.5 shows how the radiation is of high energy and is able to travel large distances. As the distance from the central axis increases the dose decreases.

5.3.2 Separated Components: Head Leakage, Collimator Scatter and Phantom Scatter

Clinically relevant scans were taken at a gantry angle of 0°, at collimator angle 0°, 45° and 270°, with a field size of 10 cm x 10 cm and MLC size of 10 cm x 10 cm, with and without phantom scatter.

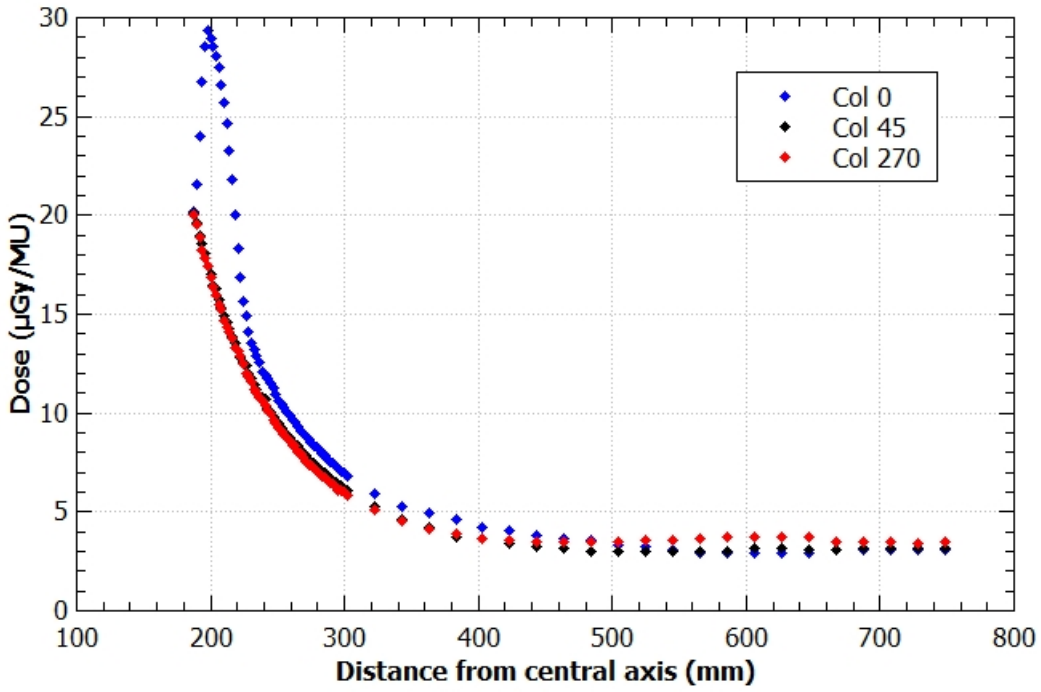

Figure 5.6 Total Scatter Contribution at depth 1.5 cm, Field size 10 cm x 10 cm, MLCs 10 cm x 10 cm. Maximum uncertainty 6% (95% confidence interval)

The total scattered radiation from head leakage, collimator scatter and phantom scatter, is demonstrated in Figure 5.6. It can be seen that the total dose is greatest at reference conditions.

The separated scatter components at collimator 0°, 45° and 270°, at depth 1.5 cm, MLC size 10 cm x 10 cm, field size 10 cm x 10 cm are shown in Figures 5.7, 5.8 and 5.9 below.

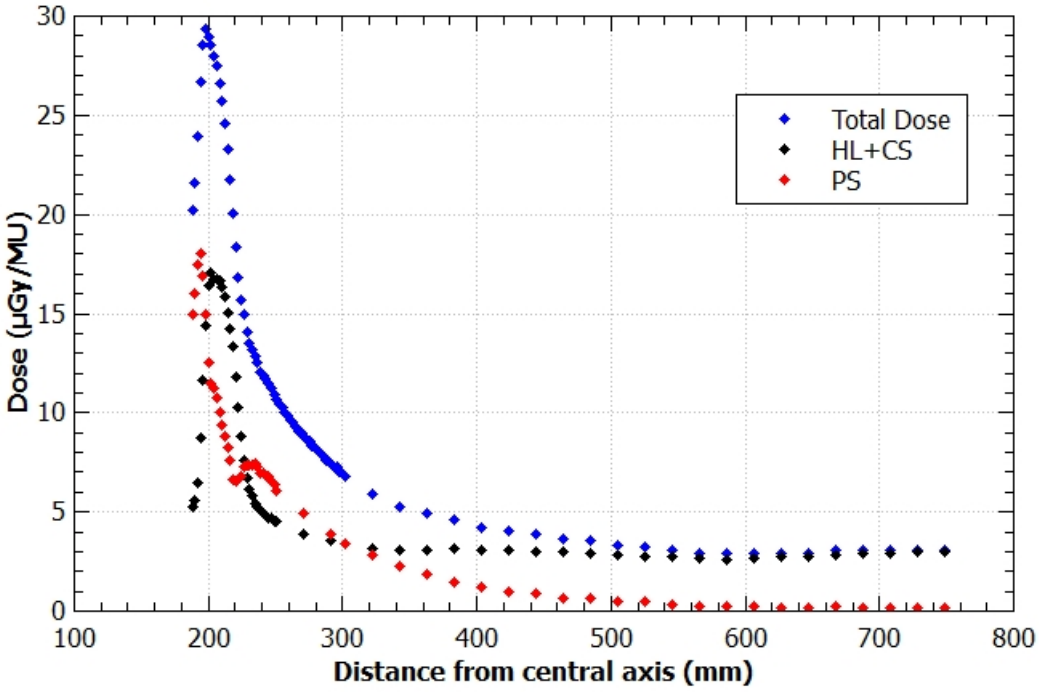

Figure 5.7 Separated Scatter Components at Collimator 0°, depth 1.5 cm, MLCs 10 cm x 10 cm, Field size 10 cm x 10 cm. Maximum uncertainty for Total Dose and HL+CS is 6% (95% confidence interval). Maximum uncertainty for PS is 8.5% (95% confidence interval)

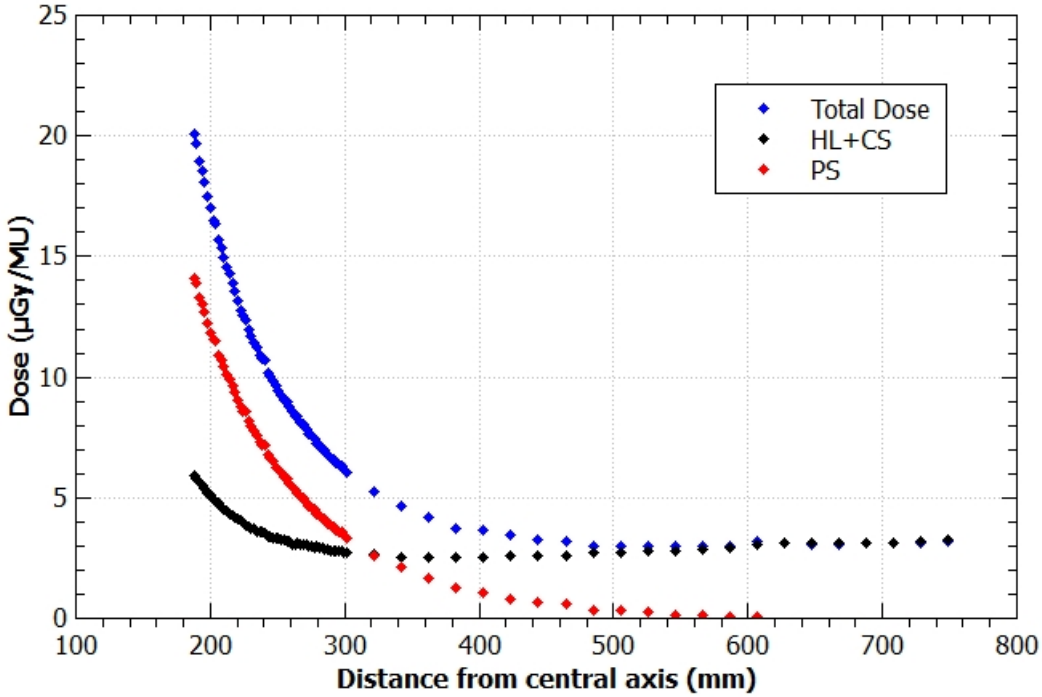

Figure 5.8 Separated Scatter Components at Collimator 45°, depth 1.5 cm. Maximum uncertainty for Total Dose and HL+CS is 6% (95% confidence interval). Maximum uncertainty for PS is 8.5% (95% confidence interval)

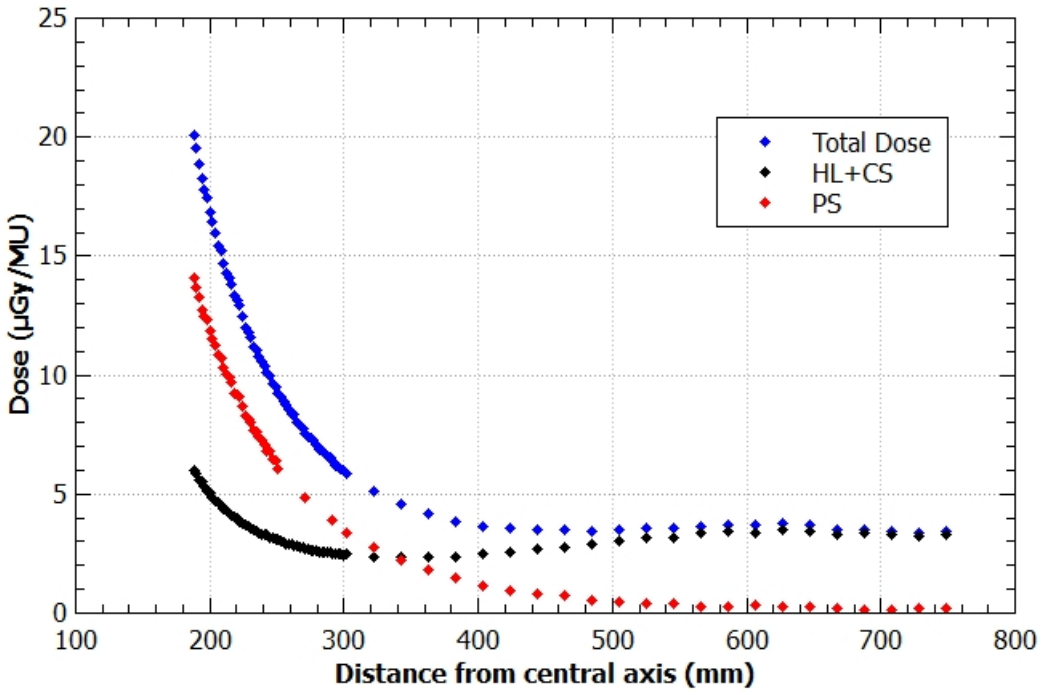

Figure 5.9 Separated Scatter Components at Collimator 270°, depth 1.5 cm. Maximum uncertainty for Total Dose and HL+CS is 6% (95% confidence interval). Maximum uncertainty for PS is 8.5% (95% confidence interval)

The scattered radiation from the head leakage and collimator scatter alone, is demonstrated in Figure 5.10.

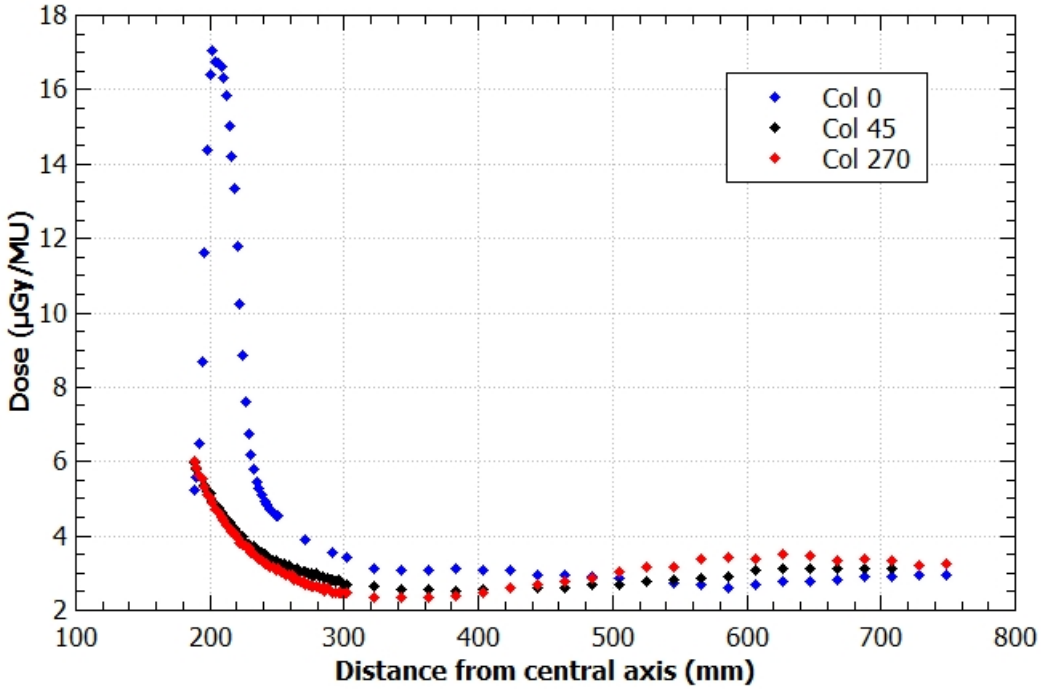

Figure 5.10 Collimator Scatter + Head Leakage at depth 1.5 cm, Field size 10 cm x 10 cm, MLCs 10 cm x 10 cm. Maximum uncertainty for 6% (95% confidence interval)

To separate head leakage from collimator scatter and phantom scatter, the MLCs were closed, at collimator angle 45° and 270°, to block any scatter from the jaws and the phantom. Figure 5.11 and Figure 5.12 shows the head leakage alone, at collimator angle 45° and 270°. The dose is highest at the shallowest depth of 5 mm.

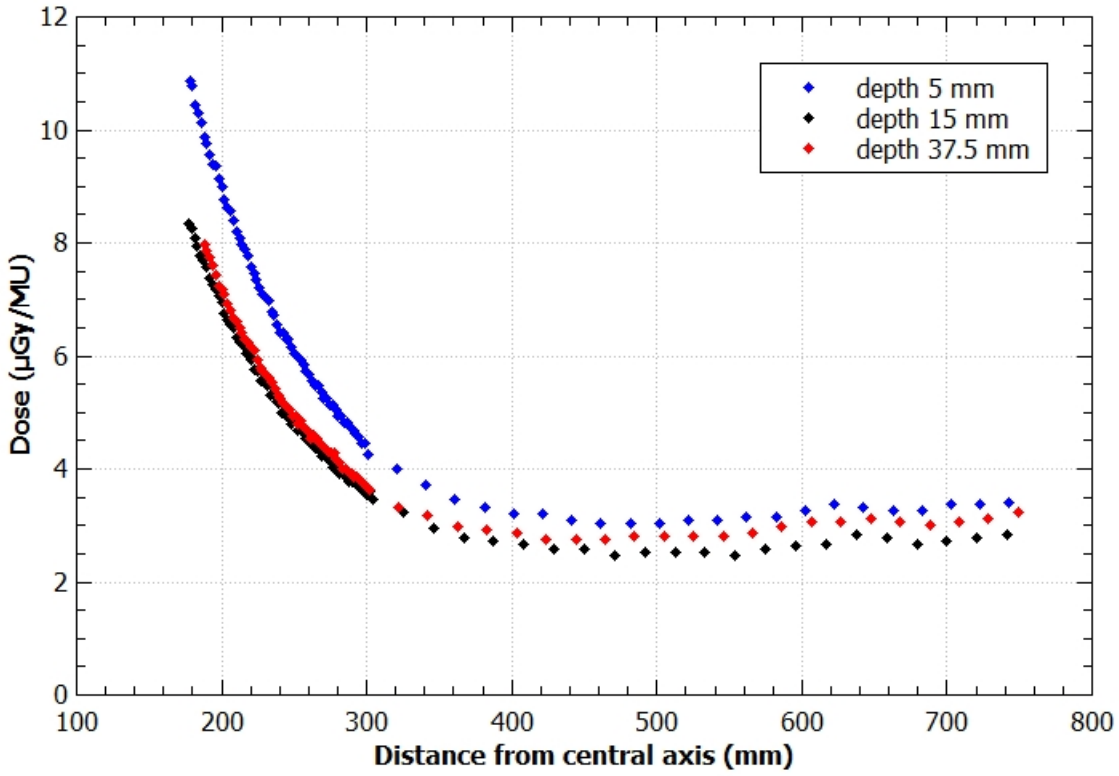

Figure 5.11 Head Leakage: Out-of-field dose profile showing the effect of closing the MLCs at collimator 45°, Field size of 10 cm x 10 cm. Maximum uncertainty 6% (95% confidence interval)

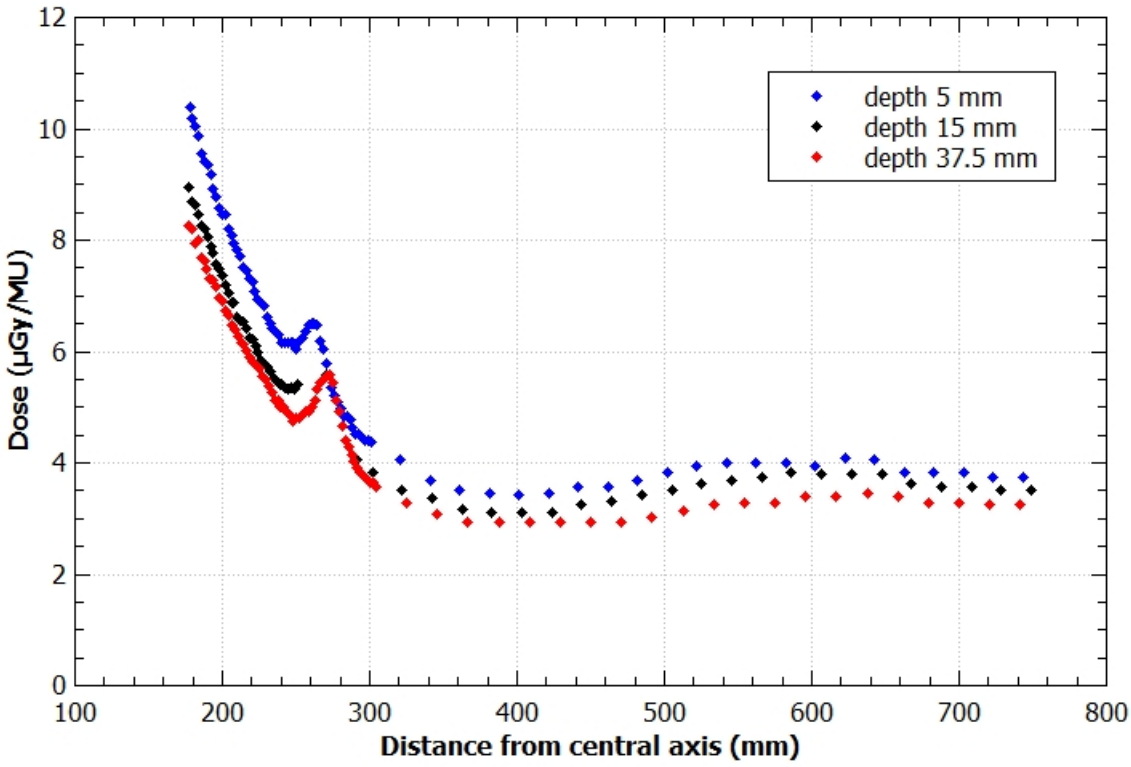

Figure 5.12 Head Leakage: Out-of-field dose profile showing the effect of closing the MLCs at collimator 270°, Field size 10 cm x 10 cm. Maximum uncertainty 6% (95% confidence interval)

The difference between the total scattered radiation and scattered radiation from the head leakage and collimator scatter, at collimator angle 0°, 45° and 270°, gives the phantom scatter shown in Figure 5.13.

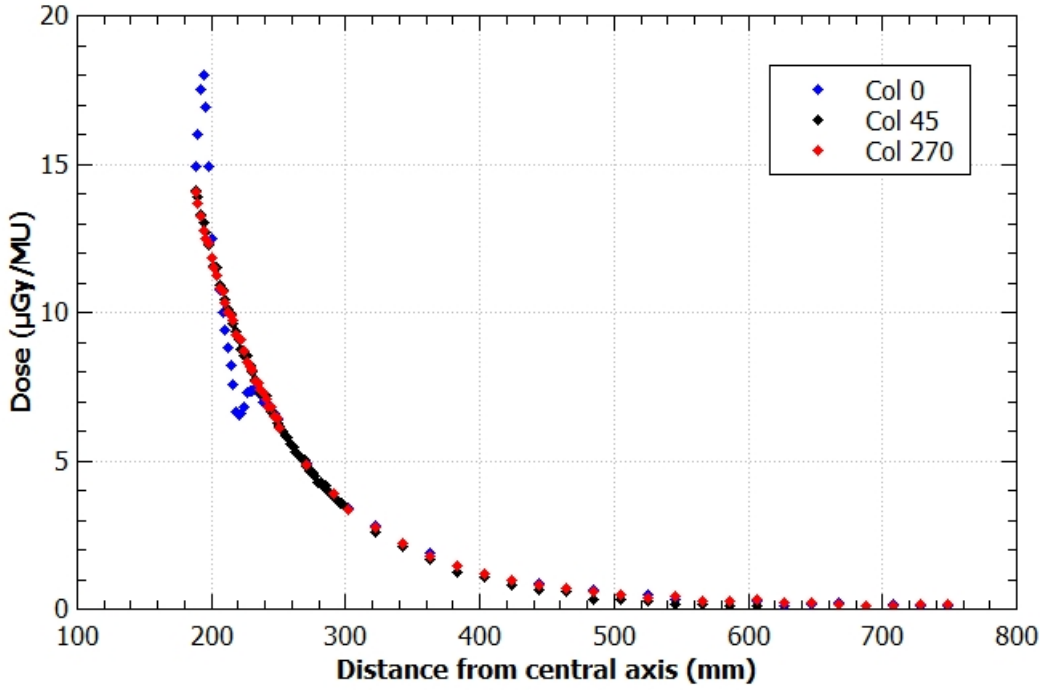

Figure 5.13 Phantom (water) Scatter at depth 1.5 cm, MLCs 10 cm x 10 cm, Field size 10 cm x 10 cm. Maximum uncertainty for Phantom Scatter is 8.5% (95% confidence interval)

Figure 5.13 shows the phantom scatter is greatest close to the field edge and there is no significant change with collimator angle, because the amount of patient scatter depends only on the size of the irradiated volume and the distance from the edge of that volume.

The difference between the scattered radiation from the head leakage and collimator scatter and the head leakage alone, will give the amount of collimator scatter. Since there is very little difference between the scattered radiation from the head leakage and collimator scatter and the head leakage alone, this means that the collimator scatter is negligible.

5.3.3 Contribution of Phantom Scatter

To further examine the effect of the phantom scatter, out-of-field dose profiles at a depth 15 mm and 37.5 mm showed the total scatter contribution to be much greater with the phantom than without.

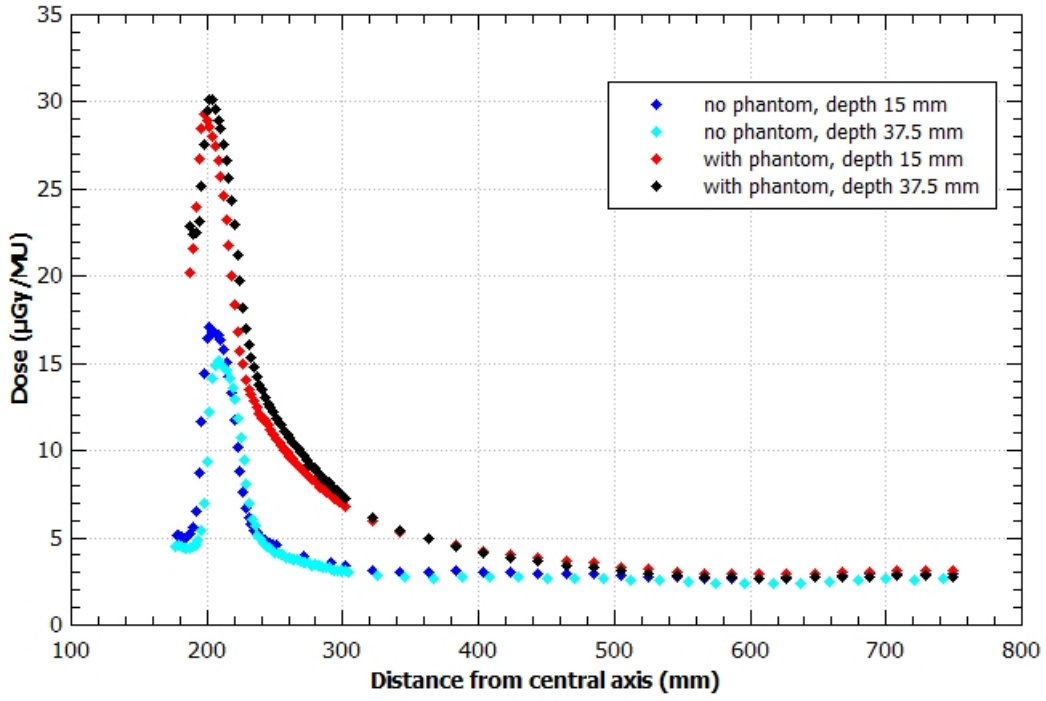

Figure 5.14 Effect of Phantom Scatter: Total Scatter Contribution compared with Head Leakage and Collimator Scatter. Conditions: Col 0°, MLC 10 cm x 10 cm and Field size 10 cm x 10 cm. Maximum uncertainty 6% (95% confidence interval)

Figure 5.14 shows that there is very little depth dependence. At a distance of 20 cm from central axis there is a peak which is solely a result of head leakage and collimator scatter, as at distances beyond 20 cm from central axis the dose drops off exponentially.

5.3.4 Effect of Varying Depths

The Total Scatter contribution compared with Head Leakage and Collimator Scatter at varying depths, at collimator 0°, 45° and 270° is examined below.

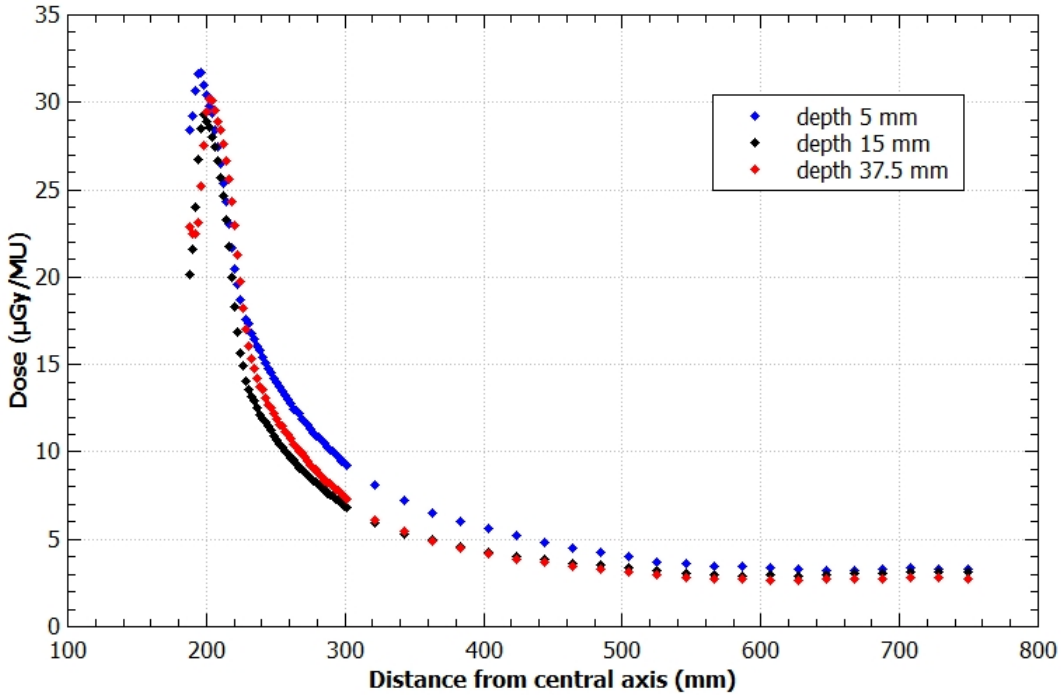

Figure 5.15 Effect of Depth: Total Scatter Contribution. Conditions: Col 0°, MLC 10 cm x 10 cm and Field size 10 cm x 10 cm. Maximum uncertainty 6% (95% confidence interval)

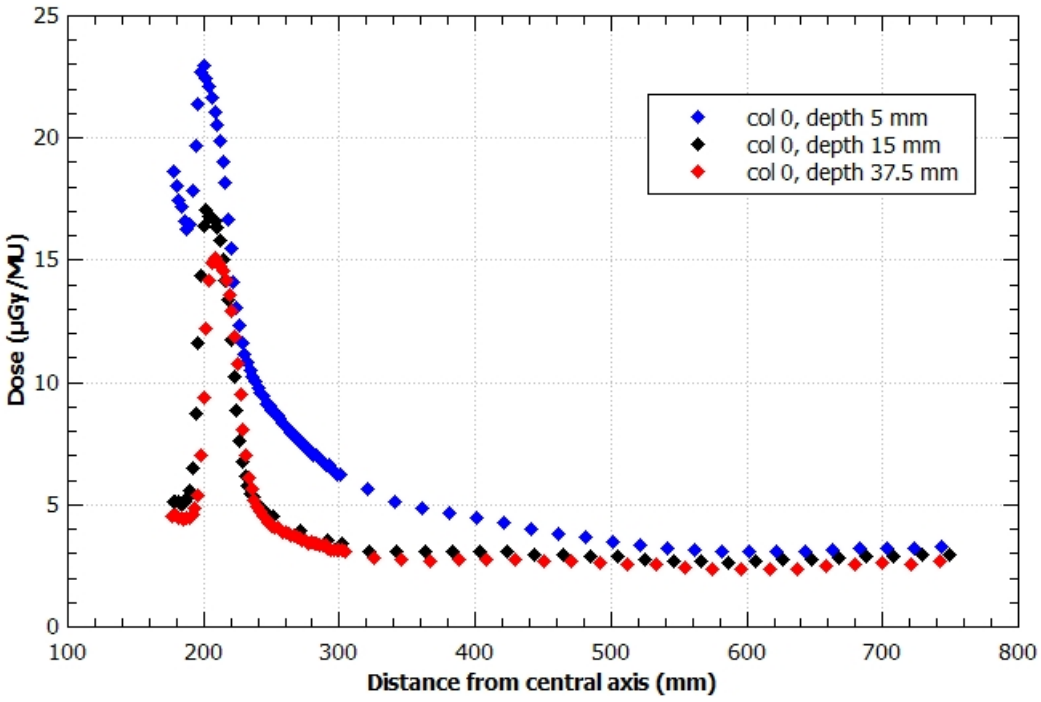

Figure 5.16 Effect of Depth: Head Leakage + Collimator Scatter Contribution. Conditions: Col 0°, MLC 10 cm x 10 cm and Field size 10 cm x 10 cm. Maximum uncertainty 6% (95% confidence interval)

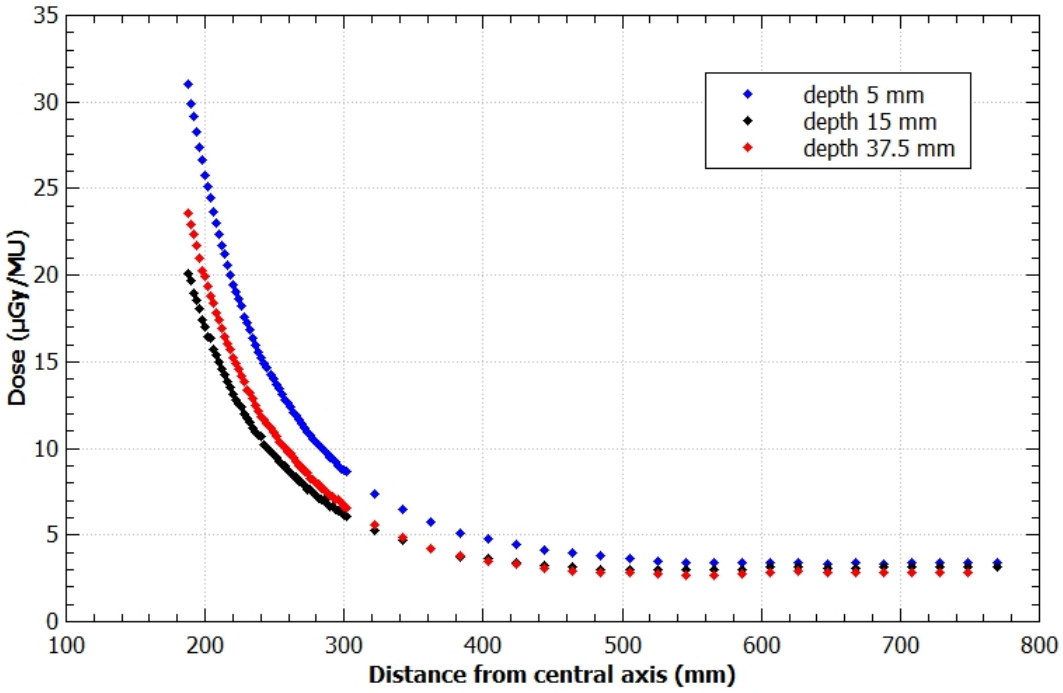

Figure 5.17 Effect of Depth: Total Scatter Contribution. Conditions: Col 45°, MLC 10 cm x 10 cm and Field size 10 cm x 10 cm. Maximum uncertainty 6% (95% confidence interval)

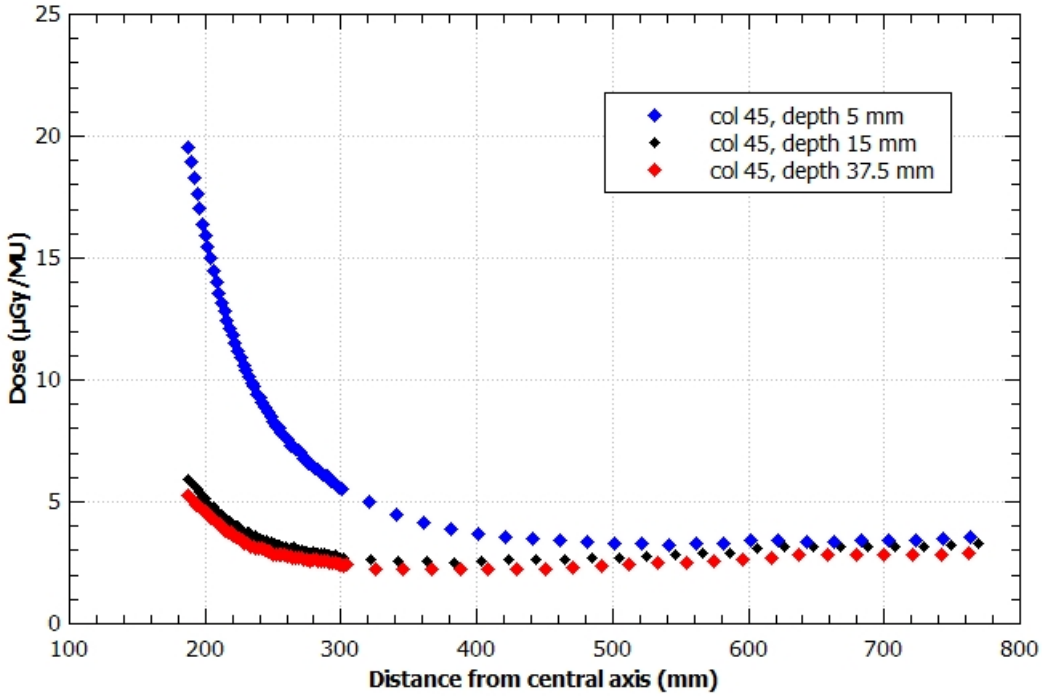

Figure 5.18 Effect of Depth: Head Leakage + Collimator Scatter Contribution. Conditions: Col 45°, MLC 10 cm x 10 cm and Field size 10 cm x 10 cm. Maximum uncertainty 6% (95% confidence interval)

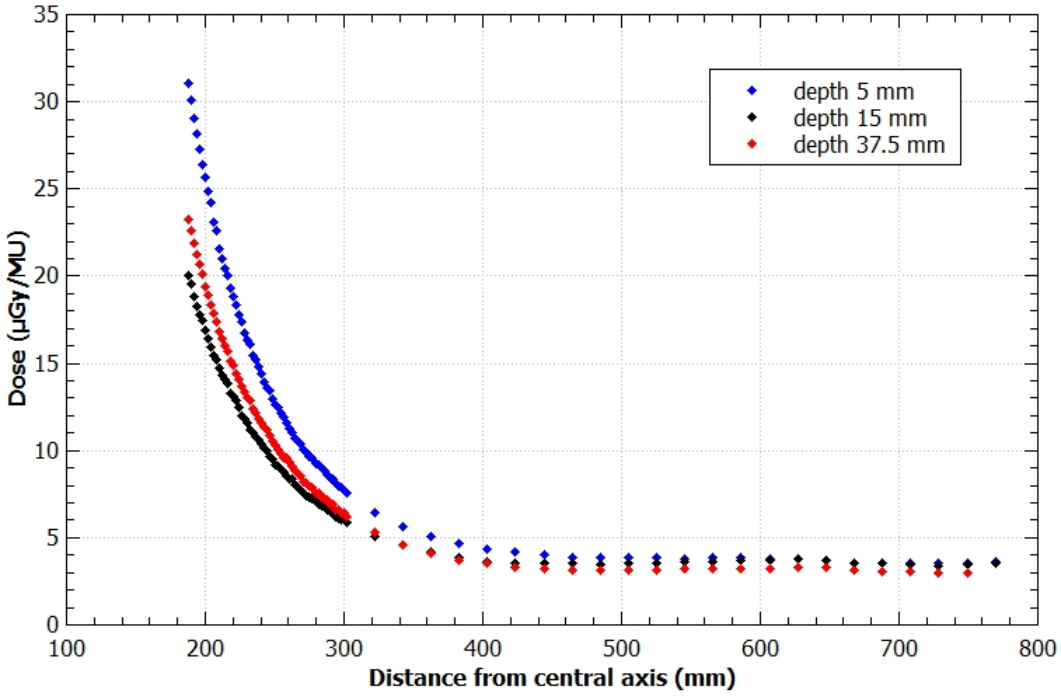

Figure 5.19 Effect of Depth: Total Scatter Contribution. Conditions: Col 270°, MLC 10 cm x 10 cm and Field size 10 cm x 10 cm. Maximum uncertainty 6% (95% confidence interval)

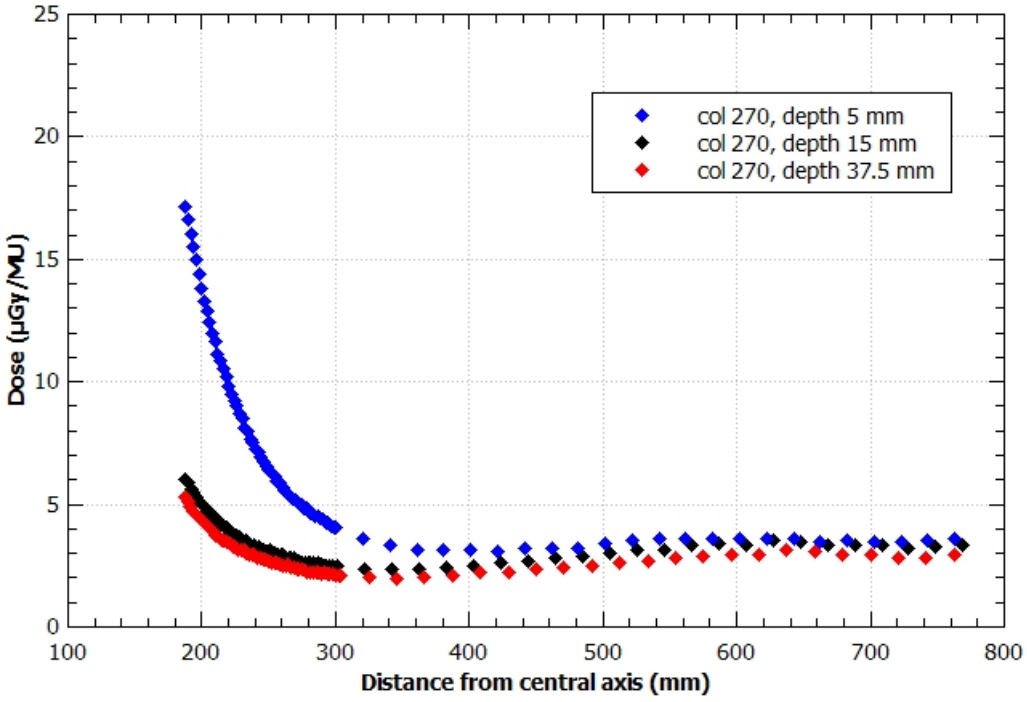

Figure 5.20 Effect of Depth: Head Leakage + Collimator Scatter Contribution. Conditions: Col 270°, MLC 10 cm x 10 cm and Field size 10 cm x 10 cm. Maximum uncertainty 6% (95% confidence interval)

The Total Scatter contribution compared with Head Leakage and Collimator Scatter at varying depths, at collimator 0°, 45° and 270° was successfully examined. The effect of varying depths from 5 mm, 15 mm and 37.5 mm showed that the dose is higher at shallower depths than d_{max}, which is probably due to electrons.

5.3.5 Effect of Varying MLC Field Size

The Total Scatter contribution, at depth of 5 mm, with varying MLC field sizes is shown in Figure 5.21 below.

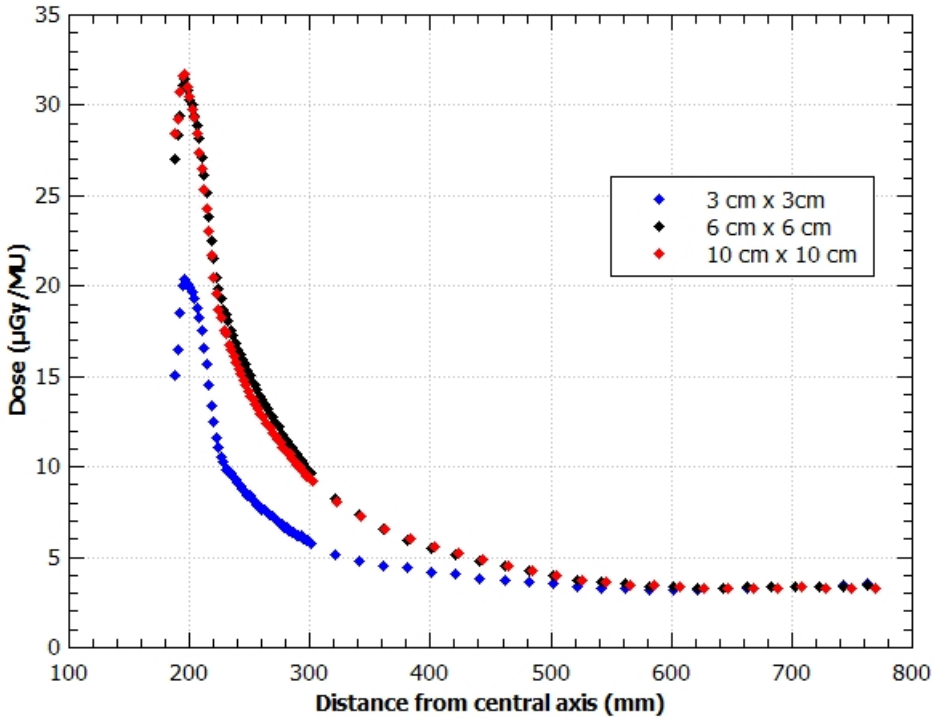

Figure 5.21 Effect of MLC Field Size: Total Scatter Contribution. Conditions: Collimator 0°, depth 5 mm, Field size 10 cm x 10 cm. Maximum uncertainty 6% (95% confidence interval)

The total scatter contribution, at a depth of 5 mm, is smaller for the 3 cm x 3 cm MLC field size. As the MLC field size is increased, the contribution from scatter increases. The 6 cm x 6 cm MLC field size appears to have a larger contribution than the 10 cm x 10 cm MLC field size. This is an indication of the effect of setup uncertainties on the results, which has been accounted for.

5.3.6 Effect of Varying Focus to Source Distance (FSD)

The Total Scatter contribution, at depths of 5 mm, 15 mm and 37.5 mm, with FSD of the pelvis phantom moved 5 cm up, at collimator 0° is demonstrated in Figure 5.22.

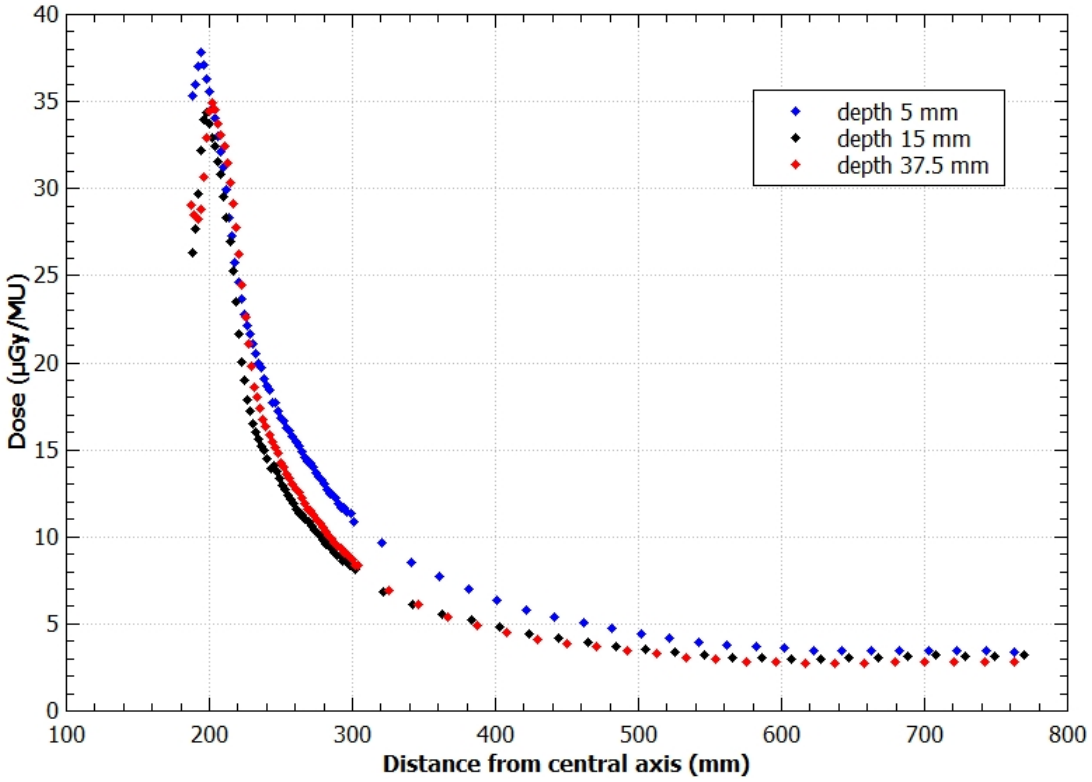

Figure 5.22 Effect of FSD: Total Scatter Contribution. Conditions: Collimator 0°, MLC size 10 cm x 10 cm, Field size 10 cm x 10 cm, pelvis phantom moved 5 cm up. Maximum uncertainty 6% (95% confidence interval)

The total scatter contribution, at depth of 5 mm, with FSD of the pelvis phantom moved 5 cm up compared with original position, at collimator 0° is demonstrated in Figure 5.23.

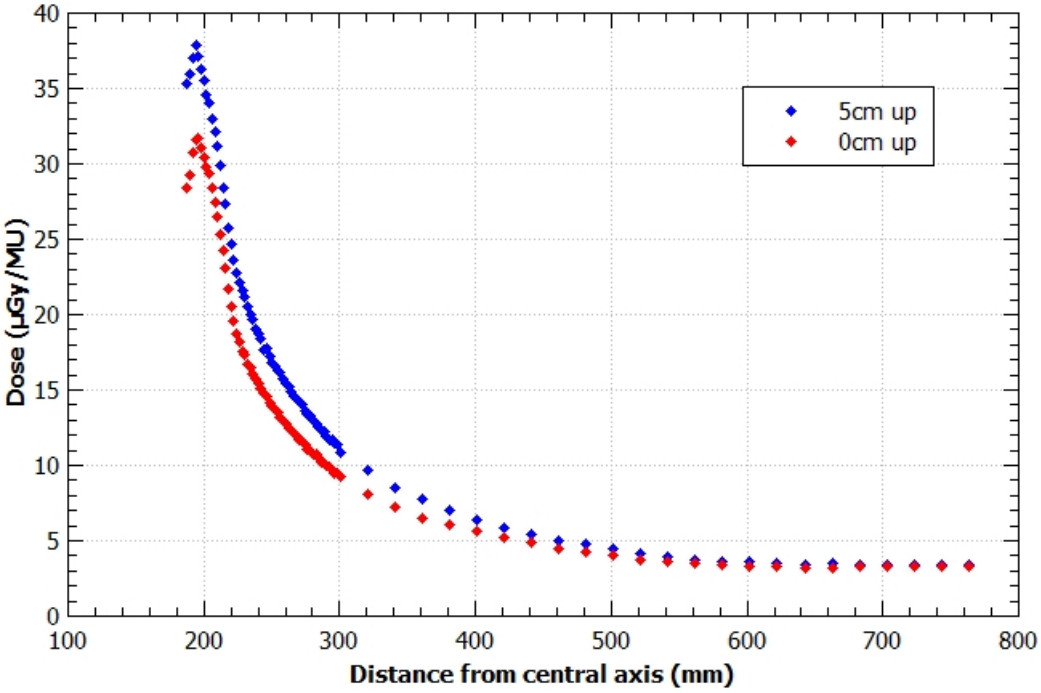

Figure 5.23 Effect of FSD:Total Scatter Contribution. Conditions: Collimator 0°, MLC size 10 cm x 10 cm, Field size 10 cm x 10 cm, FSD of the pelvis phantom moved 5 cm up compared with original position. Maximum uncertainty 6% (95% confidence interval)

5.4 Discussion/Conclusion

The out-of-field dose components and the relative contributions of leakage and the two components of scatter were effectively examined.

Firstly, out-of-field dose profile measurements from a 6 MV photon beam as a function of distance from central axis, at depth of 3.75 cm and 11.25 cm were found to be in good agreement with Kry et al.(2006) [26] measured and simulated Monte Carlo results. The agreement with published data verified that the measured methods were appropriate.

The total scattered radiation from head leakage, collimator scatter and phantom scatter was examined at a gantry angle 0°, at collimator angle 0°, 45° and 270°, with a field size of 10 cm x 10 cm and MLC size of 10 cm x 10 cm, with the phantom scatter. The total dose was greatest at collimator 0° and the peak observed at approximately 20 cm away from central axis was concluded to be a result of the treatment head geometry, namely the leakage radiation penetrating through the collimators. This leakage radiation is not observed at collimator angle 45° and 270° due to the components within the LINAC. By changing the collimator angle the high energy leakage radiation is blocked and the collimators move to reduce the gap for leakage radiation to pass through, thus reducing the shielding effect. Therefore, at collimator angle 45° and 270°, head leakage and collimator scatter are not the dominant source of out-of-field dose. At distances of greater than 30 cm from central axis, head leakage and collimator scatter dominate over phantom scatter.

The scattered radiation from the head leakage and collimator scatter alone, was examined at gantry angle 0°, at collimator angle 0°, 45° and 270°, with a field size of 10

cm x 10 cm and MLC size of 10 cm x 10 cm. The scattered radiation dose was greatest at collimator 0° and the peak at approximately 20 cm away from central axis was concluded to be a production of the treatment geometry, namely the leakage radiation penetrating through the collimators. At collimator angle 45° and 270°, phantom scatter dominates closest to the central axis, head leakage and collimator scatter dominate at distances greater than 30 cm from central axis. Therefore, the scattered radiation is highest closest to the central axis and decreases exponentially with increasing distance.

Comparing the total scattered radiation with the scattered radiation from the head leakage and collimator scatter alone, at collimator angle 0°, the maximum dose is 30 μGy/MU and 17 μGy/MU respectively. Therefore, the total scattered dose is much greater than the scattered radiation from the head leakage and collimator scatter alone. As expected, the presence of the phantom results in an overall increase in the total scattered radiation and this effect is most prominent closer to the central axis.

By closing the MLCs, at collimator angle 45° and 270°, to block any scatter from the jaws and removing the phantom, head leakage can be separated from collimator scatter and phantom scatter. The out-of-field dose will be only a result of head leakage. The head leakage dose, at collimator angle 45° and 270° is highest at the shallowest depth of 5 mm. Closing the MLCs at collimator angle 270°, there is a peak at approximately 26 cm from central axis which represents the head leakage, due to the change in collimator location i.e. inherent shielding within the LINAC.

Comparing the total scattered radiation with the scattered radiation from the head leakage and collimator scatter alone, at collimator angle 0°,45° and 270°, at depths of 5 mm, 15 mm and 37.5 mm, the dose profiles show the dose is highest at the shallowest depth of 5 mm, which is lower than d_{max}. The high dose at shallow depths is probably due to

electrons which have been scattered at the surface. At depths of 5 mm, 15 mm and 37.5 mm, the total scattered radiation is greater than the scattered radiation from the head leakage and collimator scatter alone. The peak observed at approximately 20 cm away from central axis, is a result of head leakage which must be of high energy, as the peak is shifted by the same amount when phantom scatter is considered.

Examining the effect of varying depths from 5 mm, 15 mm and 37.5 mm, at collimator angle 0°, 45° and 270°, on the out-of-field dose profiles with and without phantom scatter, shows that the dose is highest at shallower depths than d_{max}, which is probably due to electrons. This is important to note as the sensitive region of the eye lens where radiation becomes of critical concern is between 2.8 - 3.8 mm and CIEDs which are inserted just beneath the skin at depths between 5 - 10 mm are also shallow and therefore will be adversely affected by the high doses near the surface. Comparing the total scattered radiation with the scattered radiation from the head leakage and collimator scatter alone, at collimator angle 0°, the maximum dose, at the shallowest depth of 5 mm is 32 μGy/MU and 23 μGy/MU respectively. Therefore, the total scattered dose is much greater than the scattered radiation from the head leakage and collimator scatter alone. As expected, the presence of the phantom results in an overall increase in the total scattered radiation.

Examining the effect of varying MLC field sizes from 3 cm x 3 cm, 6 cm x 6 cm and 10 cm x 10 cm, at collimator angle 0°, with phantom scatter showed that the total scattered radiation dose increases with increasing field size. As MLC field size increases, this directly increases the size of the irradiated volume. The larger the MLC field size, the greater the phantom scatter. Therefore, out-of-field dose depends on MLC field size.

Examining the effect of varying the FSD at collimator angle 0° showed that the total

scattered radiation dose increases as the position of the phantom is moved up by 5 cm relative to the height of the water tank. Thus, as the FSD is increased, the total scattered radiation dose is increased due to greater internal phantom scatter.

Overall, the total scattered radiation dose and the head leakage and collimator scatter contribution alone were successfully separated and characterised. The peak at approximately 20 cm from central axis at collimator 0° is a result of the treatment head geometry, namely the leakage penetration through the Y-jaw of the secondary collimator before passing through the gap between the lateral edge of the MLC and the primary collimator. The dominant source of out-of-field dose close to the beam edge, was found to be internal patient scatter. The out-of-field dose depends on the distance from central axis. Therefore, the further away from central axis, the smaller the out-of-field dose.

Conclusively, out-of-field dose is primarily highest closest to the treatment field where phantom scatter dominates, while further away from the field edge, at distances greater than 20 cm, head leakage dominates. Therefore, total scattered radiation is dependent on the distance from central axis, depth of measurement, MLC field size and shape and the total delivered dose. Hence, the out-of-field dose could be reduced by increasing distance from the field edge, increasing depth of measurement and decreasing MLC field size. The relative total scattered radiation contributions would also vary with beam energy, MU requirements of the treatment and internal components within the LINAC. The contributions of head leakage and collimator scatter alone are also dependent on linear accelerator and collimator design [43]. Finally, strong correlation of measurements was seen between experimental measurements and other studies [26, 43]. Subtle variations were attributed to positional misalignment of the detectors, reproducibility of the set-up and different linear accelerator used.

Chapter 6

Out-of-Field Dose to the Eye Lens and Chest for Clinical VMAT Treatments

For the purpose of this study, three VMAT patient plans of the prostate target volume were used. The prostate target volume is approximately 7 cm in diameter, however this varies from patient to patient. The dose distribution will be strongly dependent on the Planning Target Volume (PTV) location, and the primary beam energy. The aim of this chapter is to measure the out-of-field dose to the eye lens and chest (including patients with pacemakers and ICDs) for patients undergoing VMAT of the prostate.

6.1 Materials

An anthropomorphic (anthro human, morphic shape, form or structure of human beings) torso and head phantom was used for all irradiation VMAT plans. The positioning of the phantom was extremely important and thus had to be kept consistent throughout all experiments. The Radiology Support Services, INC, Long Beach, CA USA built this phantom from a human skeleton embedded in tissue-equivalent polyurethane and cut it into 35 slices with a thickness of 25 mm each.

A Roos ionisation chamber and a 0.6 cm^3 cylindrical ionisation chamber were used for the comparison between the amount of wax needed to obtain equivalent depths. As for the out-of-field dose measurements the characteristics of both the Roos chamber and cylindrical chamber were taken into account in choosing which detector to use. Parallel plate chambers are much better for near-surface measurements because of their good spatial resolution in the depth direction, however they exhibit large angular dependence. This was not a problem for the PDD measurements with gantry 0 in Chapter 4, however the VMAT patient plans are delivered in arcs and a parallel plate chamber would therefore be unsuitable. Therefore, a 0.6 cm^3 cylindrical ionisation chamber that has good azimuthal angular independence was used, as long as the chamber's long axis was aligned parallel to the axis of gantry rotation, the arc delivery was not a problem.

6.2 Methodology

A comparison was made between PDDs measured with both the Roos chamber and the 0.6 cm^3 cylindrical chamber in order to determine how much wax to use over the top of the 0.6 cm^3 cylindrical ionisation chamber. Once this appropriate thickness of wax was determined, the 0.6 cm^3 cylindrical chamber was placed along the length of the phantom at the location of the eye lens and chest to measure the out-of-field dose. The ideal chamber positions were found on the phantom and were kept the same for all experiments. An image of the full phantom is shown in Figure 6.1; the areas measured with the ionisation chamber are marked.

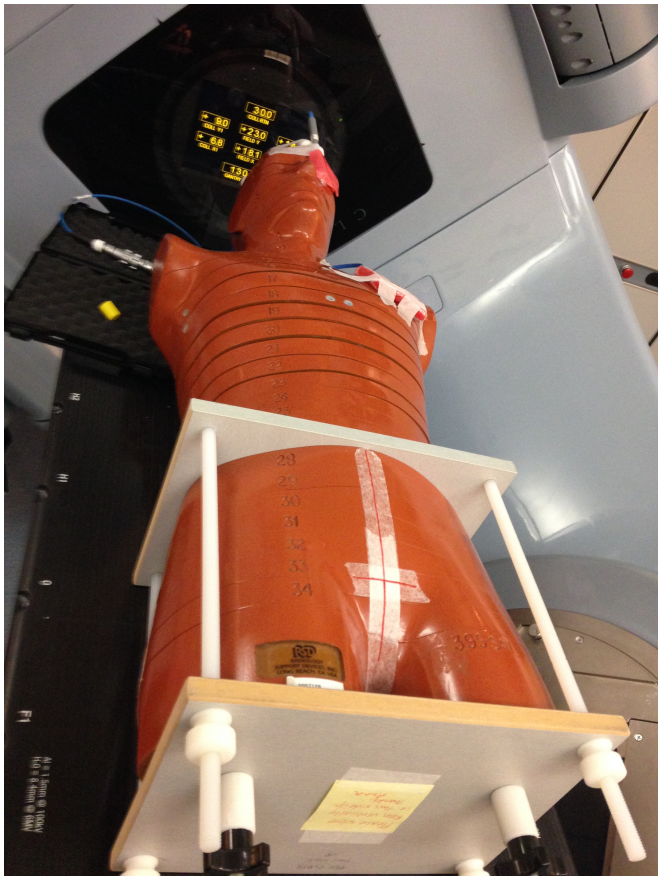

Figure 6.1 Full anthropomorphic phantom with the location of the ionisation chambers marked

To measure the dose to the critical regions of interest (the eye lens and chest), VMAT patient plans were delivered. The VMAT plans delivered two arc rotations with different MU at each rotation. The table below shows the arc rotation and the number of MUs delivered at the location of the eye lens and chest. The dose was measured on a RANDO anthropomorphic phantom with a 0.6 cm^3 cylindrical chamber placed over the eye lens and CIED region for a range of patient treatment fields. The ionisation chamber was encapsulated by wax to represent the eye lens and CIED beneath the chest. The anthropomorphic phantom was positioned in the supine position as close as possible to the

gantry head to represent realistic patient positioning. The experimental setup is shown in the Figure 6.2.

Figure 6.2 Positioning of the ionisation chambers on the anthropomorphic phantom

The proportion of patient scatter contributing to the total dose was determined by scanning with and without scatter material in the field. This was performed by adding and removing the pelvic region of the phantom from beneath the beam. Tables 6.1 and 6.2 show the amount of MUs and dose delivered for each arc rotation with and without the pelvic phantom.

The dose to the eye lens and chest was calculated by removing the phantom from the beam and irradiating air to determine the contribution of patient scatter. For this reason, the maximum and minimum reading for regions of interest at arc 1 and arc 2 with and without patient scatter was recorded. Addition of the maximum values gave the total dose for both arcs, which was then multiplied by 35 to obtain the total dosage to the eye lens and chest, for 70 Gy in 35 fractions, as this is the average total prescribed dose that a prostate patient receives in a treatment.

Patient	Phantom	Arc	MU	Dose(cGy)
1	Yes	1	371	0.162±0.005
1	Yes	2	312	0.147±0.004
1	No	1	371	0.154±0.005
1	No	2	312	0.137±0.004
2	Yes	1	199	0.062±0.002
2	Yes	2	339	0.115±0.003
2	No	1	199	0.062±0.002
2	No	2	339	0.114±0.003
3	Yes	1	335	0.131±0.004
3	Yes	2	443	0.189±0.006
3	No	1	335	0.126±0.004
3	No	2	443	0.181±0.005

Table 6.1 MU and dose per fraction delivered to the eye lens for three separate patient plans

Patient	Phantom	Arc	MU	Dose(cGy)
1	Yes	1	371	0.207±0.006
1	Yes	2	312	0.168±0.005
1	No	1	371	0.198±0.006
1	No	2	312	0.154±0.005
2	Yes	1	199	0.044±0.001
2	Yes	2	339	0.080±0.002
2	No	1	199	0.043±0.001
2	No	2	339	0.080±0.002
3	Yes	1	335	0.142±0.004
3	Yes	2	443	0.198±0.006
3	No	1	335	0.136±0.004
3	No	2	443	0.187±0.006

Table 6.2 MU and dose per fraction delivered to the chest for three separate patient plans

6.3 Results

6.3.1 Comparison: Roos chamber and Cylindrical chamber

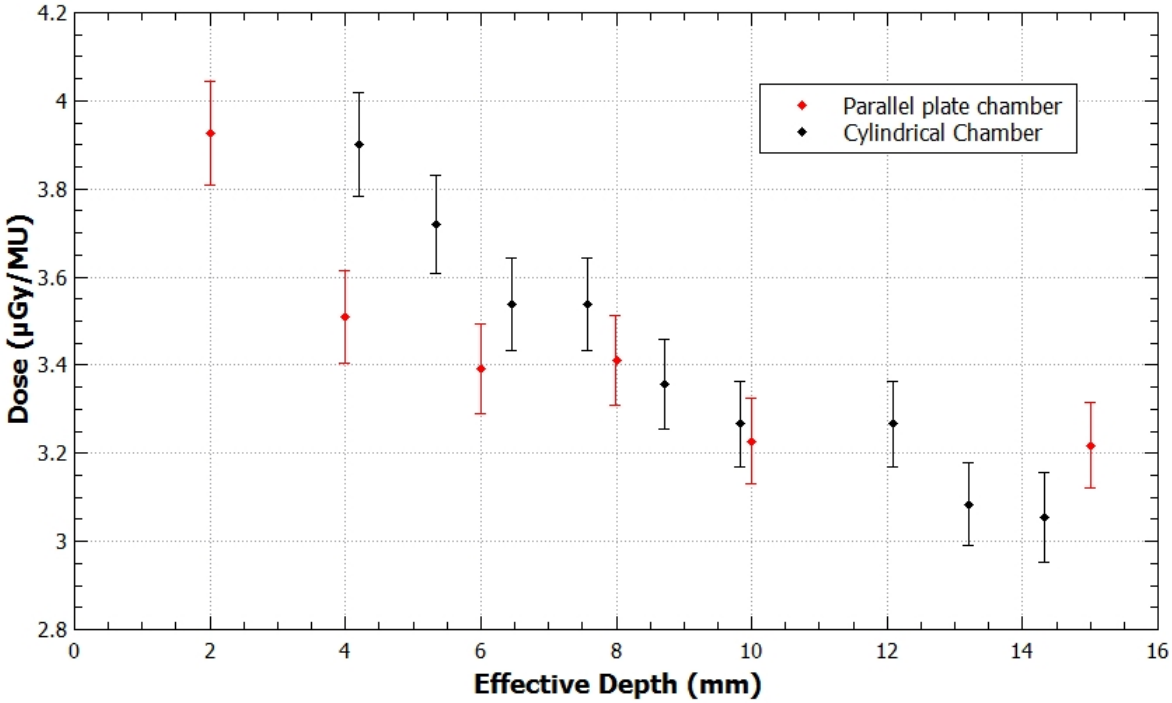

Figure 6.3 Out-of-Field Depth Dose Comparison between Roos and 0.6cm^3 Cylindrical Chamber, at the location of the eye lens (76 cm from central axis), with 10 cm x 10 cm field size.

Figure 6.3 shows that dose near-surface measured with the Roos and 0.6 cm^3 cylindrical chambers agree to within 3%, for depths of 6 mm and greater. This confirmed that the 0.6 cm^3 cylindrical ionisation chamber could be used for measuring the dose to the eye lens and chest, even though it is inherently less suitable for near-surface doses compared to a Roos chamber. As discussed previously, the main advantage of the cylindrical chamber is its angular independence, which was essential for VMAT measurements.

Treatment	Eye Lens (cGy)	Error (cGy)	CIED (cGy)	Error (cGy)
1	10.20	0.31	12.30	0.37
2	6.20	0.19	4.30	0.14
3	10.80	0.32	11.30	0.34
Average	9.00	0.27	9.30	0.28
Maximum	10.80	0.32	12.30	0.37
Recommended Limits	50	-	100-200	-

Table 6.3 VMAT Results (70 Gy, 35 fractions)

6.3.2 Anthropomorphic Phantom Measurements

A typical VMAT prostate plan delivering 70 Gy in 35 fractions to isocentre, resulted in a maximum of 11 cGy and 12 cGy to the eye lens and chest regions respectively, both of which are below the recommended limits.

From Tables 6.1 and 6.2, the general trend between the MU and dose delivered to obtain an estimate of other VMAT prostate plans based on MU is shown below.

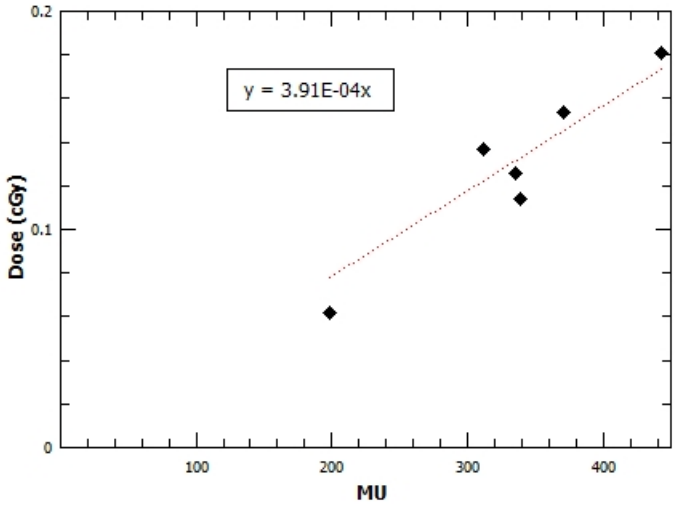

Figure 6.4 MU and Dose to the Eye Lens

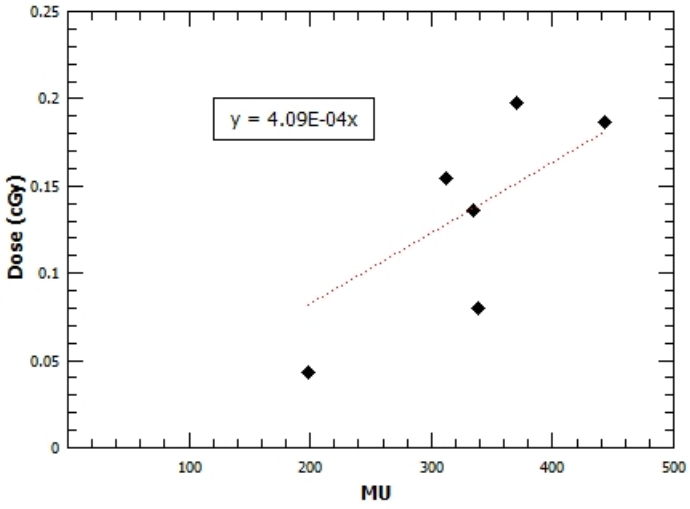

Figure 6.5 MU and Dose to the Chest

6.4 Discussion/Conclusion

The out-of-field dose to the eye lens and the chest were measured for patient plans of VMAT of the prostate. Conclusively, the dose to the eye lens and chest outside the radiation field were measured to be well below the recommended thresholds conveyed by ICRP [1] and EviQ [3].

Removal of the phantom from the beam reduced the dose to the eye lens and chest by approximately 1-2%, showing that patient scatter is insignificant for the eye lens and chest. This is due to internal patient scatter being the dominant source of radiation dose for a distance of only 10 cm from the field edge, after which head leakage and collimator scatter predominates. This would be further be influenced by the field size and MU demand of VMAT. The relative contributions of different components of scatter and leakage are likely to vary with field size, beam energy, MU requirements of VMAT and

depth of measurement. Under the conditions tested, the maximum dose received by the eye lens was 10.8±0.3 cGy and the maximum dose received by the chest was 12.3±0.4 cGy.

Overall, the results showed that the dose to the eye lens for a clinical VMAT prostate treatment were below the recommended thresholds (11 cGy compared to 50 cGy) [1]. For the eye lens dose (with 0.00039 cGy/MU), to arrive at the recommended limit of 50 cGy, a 35 fraction plan would need 3500 MU in a single fraction. This is well above the modulation factor expected from a clinical prostate plan. The maximum dose to the chest was below the recommended threshold as well (12 cGy compared to 200 cGy) [3], this confirmed the results of the 2017 HRS International expert consensus statement, which stated that the risk of failure of the CIED device is low, as there is no evidence of damage up to 5 Gy [35]. This is positive for the introduction of VMAT for prostate treatments at St George Cancer Care Centre.

Notably, for patients whose the dose to the eye lens or chest is of critical concern, or whose treated volume is close to the area at risk, the dose should be measured either in-vivo or in the phantom. Traditionally, eye lens doses have been measured in-vivo using MV photon detectors with water-equivalent build-up of 10 mm or more, however this study has shown that out-of-field doses are highest at the surface and fall off with depth. It is therefore recommended that *in-vivo* detectors have a 2 mm build up for estimating dose to the radiosensitive cells of the eye, particularly when used close to the field edge.

Chapter 7

Conclusion

In this thesis study, we have successfully evaluated the out-of-field doses to the critical structure of the eye lens and the critical region of the chest (including patients with CIEDs) for patients undergoing VMAT of the prostate at St George Cancer Care Centre. The significant results and findings from this study include:

I. We have developed a set of reliable methods and procedures to accurately measure the challenging out-of-field doses and quantitatively characterise their individual dose components from a Varian iX 6 MV VMAT treatment.

   Head leakage and collimator scatter have effectively been separated from patient scatter. Results showed that at distances close to the field edge phantom scatter was a dominant source of out-of-field, while at distances greater than 20 cm head leakage was the dominant source of out-of-field dose. This conclusion was seen across all the examined cases for different collimator angles, depths of measurement and field sizes.

II. The out-of-field doses to the eye lens and chest region (including patients with CIEDs) have been accurately measured with an anthropomorphic phantom.

    Using clinical patient VMAT plans the maximum dose received by the eye lens was found to be 10.8±0.3 cGy, and the maximum dose received to the chest was found to be 12.3±0.4 cGy. It was successfully concluded that the doses to the eye lens and chest were well below the threshold doses of 50 cGy for eye lens and 200 cGy for CIEDs [1, 3].

Conclusively, it can be said that VMAT patients of the prostate will not be at risk of cataracts or CIED failure as the out-of-field dose is minimal and will not be a harm to them. This is extremely important clinically for patients where the dose to the eye lens or CIED device is of critical concern. It is safe to undergo VMAT prostate planning without the risk of affecting these critical regions. Oncologists can safely administer dose without risk and be ensured of the safety and well-being of their prostate patients. Note that these conditions only apply for 6 MV photon beams. Treatments using photon beams of energies greater than 10 MV will produce neutron contamination which is known to be more damaging to CIEDs than photons [3, 35].

For physicists it is still a challenge to examine other sites especially where the treated volume is close to the area at risk. In such cases the dose should be measured *in-vivo* or in phantom initially before the patient undergoes treatment as the risk is still unknown. Although treatment planning systems may be able to estimate the dose outside the region of interest they are not able to give an accurate representation of the dose at greater distances from the field edge. In fact most planning systems do not accurately model photon or electron leakage/scatter from the LINAC head. This work has shown that the

dose at the surface may be higher than predicted by most planning systems.

Traditionally, eye lens doses have been measured *in-vivo* using MV photon detectors with water-equivalent build-up of 10 mm or more, however this study has shown that the out-of-field doses are highest at the surface and fall off with depth. Therefore, it is recommended that *in-vivo* detectors have a 2 mm build up for estimating dose to the radiosensitive cells of the eye, particularly when used close to the field edge.

7.1 Future Work

An initial aim of this project was to develop a model for predicting the out-of-field dose to the eye lens and CIED for patients undergoing VMAT of the prostate. This model would be used by radiation oncologists and physicists to look up the dose for different cases, therefore allowing the radiation oncologists to provide the best outcome for the patients. Future developments could involve developing a model for predicting the out-of-field dose for patients with head & neck cancer where the treatment area is close to the area at risk, since there is a clinical need for predicting and minimising out-of-field doses in order to reduce the risk of cataracts or heart failure for patients undergoing radiotherapy.

Future developments and prospects leading on from the findings of this thesis will primarily be in terms of improved awareness of the contributors of out-of-field leakage and how they can be monitored.

Bibliography

[1] International Commission On Radiological Protection (ICRP), "Statement on Tissue Reactions," Tech. Rep., 2011.

[2] R. Behrens, G. Dietze, and M. Zankl, "Dose conversion coefficients for electron exposure of the human eye lens," *Physics in Medicine and Biology*, vol. 54, no. 13, pp. 4069–4087, 2009. [Online]. Available: http://stacks.iop.org/0031-9155/54/i=13/a=008?key=crossref.1aabb4f0d5a74a7c003279bfa24b37dc

[3] eviQ Cancer Treatments Online, "Supporting Document Implantable Cardioverter Defibrillators (ICDs) in Patients Receiving Radiation Therapy," eviQ Cancer Treatments Online, Tech. Rep., 2015.

[4] Australian Institute of Health and Welfare (AIHW), "Cancer in Australia 2017," Australian Institute of Health and Welfare (AIHW), Canberra, Tech. Rep., 2017.

[5] A. G. C. Australia:, "All Cancers in Australia," 2017. [Online]. Available: https://canceraustralia.gov.au/affected-cancer/what-cancer/cancer-australia-statistics

[6] Jacob Van Dyk, "The modern technology of radiation oncology: A compendium for medical physicists and radiation oncologists," *Medical Physics Publishing*, no. First Edition, 1999.

[7] Australian Institute of Health and Welfare (AIHW), "Cancer mortality trends and projections: 2014 to 2025," 2014. [Online]. Available: https://www.aihw.gov.au/reports/cancer/cancer-mortality-trends-and-projections-2014-to-2025/contents/all-cancers-combined

[8] Cancer Council Australia, "Understanding Prostate Cancer," Cancer Council Australia, Sydney, Tech. Rep., 2016. [Online]. Available: cancer.org.au

[9] M. Stovall, C. R. Blackwell, J. Cundiff, D. H. Novack, J. R. Palta, L. K. Wagner, E. W. Webster, and R. J. Shalek, "Fetal Dose from Radiotherapy with Photon Beams: Report of AAPM Radiation Therapy Committe Task Group No.36," *Medical Physics*, vol. 22, no. 1, pp. 63–82, 1995.

[10] Faiz M. Khan PhD, *The Physics of Radiation Therapy*, fourth edi ed. Library of Congress Cataloging in Publication Data, 2010.

[11] M.N. Simmons, R. K. Berglund, and S. Jones, "A practical guide to prostate cancer diagnosis and management," *Cleveland Clinic Journal of Medicine*, vol. 78, no. 5, pp. 321–331, 2011.

[12] M. Lehman, A. J. Hayden, J. M. Martin, D. Christie, A. B. Kneebone, M. Sidhom, M. Skala, and K.-h. Tai, "FROGG high-risk prostate cancer workshop : Patterns of practice and literature review Part I : Intact prostate," *Journal of Medical Imaging and Radiation Oncology*, vol. 58, pp. 257–265, 2014.

[13] S. F. Kry, B. Bednarz, R. M. Howell, L. Dauer, D. Followill, E. Klein, H. Paganetti, B. Wang, C.-S. Wuu, and X. Xu, "AAPM TG 158 Measurement and calculation of doses outside the treated volume from external-beam radiation therapy," *Medical Physics*, vol. 44, no. 10, pp. e391–e429, 2017.

[14] D. Palma, E. Vollans, and E. al., "Volumetric modulated arc therapy for delivery of prostate radiotherapy: comparison with intensity-modulated radiotherapy

and three-dimensional conformal radiotherapy." *International Journal of Radiation Oncology Biology Physics*, vol. 72, no. 4, pp. 996–1001, 2008.

[15] D. Wolff, F. Stieler, and E. al., "Volumetric modulated arc therapy (VMAT) vs. serial tomotherapy, step-and-shoot IMRT and 3D-conformal RT for treatment of prostate cancer." *Radiotherapy Oncology*, vol. 93, no. 2, pp. 226–233, 2009.

[16] C. L. Tsai, J. K. Wu, H. L. Chao, Y. C. Tsai, and J. C. Cheng, "Treatment and dosimetric advantages between VMAT, IMRT and helical tomotherapy in prostate cancer," *Medical Dosimetry*, vol. 36, no. 3, pp. 264–271, 2011.

[17] F. Kjaer-Kristoffersen, L. Ohlhues, J. Medin, and S. Korreman, "RapidArc Volumetric Modulated Therapy Planning for prostate cancer patients," *Acta Oncologica (Stockholm, Sweden)*, vol. 48, no. 2, pp. 227–232, 2009.

[18] C. R. Ramsey, R. Seibert, S. Mahan, D. Desai, and D. Chase, "Out-of-field dosimetry measurement for a helical tomotherapy system." *Journal of Applied Clinical Medical Physics*, vol. 7, no. 3, pp. 1–11, 2006.

[19] M.Mehta, P.Hoban, and T. R. Mackie, "Comissioning and Qaulity Assurance of RapidArc Radiotherapy Delivery System: In Regard to Ling et al (Int J Radiat Oncol Biol Phys 2008; 72;575-581): Absence of Data Does Not Consitute Proof; The Proof is in Tasting the Pudding," *International Journal of Radiation Oncology Biology Physics*, vol. 75, no. 1, pp. 4–6, 2009.

[20] C. Cozzarini, C. Fiorino, N. D. Muzio, F. Alongi, S. Broggi, M. Cattaneo, F. Montorsi, and P. Rigatti, "Significant Reduction of acute toxicity following pelvic irradiation with Helical Tomotherapy in patients with localise prostate cancer," *Radiation and Oncology*, vol. 84, no. 2, pp. 164–170, 2007.

[21] M. T. Davidson, S. J. Blake, and E. al, "Assessing the role of volumetric modulated arc therapy (VMAT) relative to IMRT and helical tomotherapy in the management

of localized, locally advanced, and post-operative prostate cancer," *International Journal Radiation Oncology Biology Physics*, vol. 80, no. 5, pp. 1550–1558, 2011.

[22] A. R. Blais, E. Lederer, M. Oliver, and K. Leszczynski, "Static and rotational step-and-shoot IMRT treatment plans for the prostate: A risk comparison study," *Medical Physics*, vol. 39, no. 2, p. 1069, 2012.

[23] S. Yoo, Q. J. Wu, and E. al, "Radiotherapy treatment plans with RapidArc for prostate cancer involving seminal vesicles and lymph nodes," *International Journal of Radiation Oncology Biology Physics*, vol. 76, no. 3, pp. 935–942, 2010.

[24] E. B. Podgorsak, *Radiation Oncology Physics : A Handbook for Teachers and Students*, E. B. Podgorsak, Ed. IAEA Library Cataloguing in Publication Data, 2005.

[25] S. F. Kry, M. Salehpour, D. S. Followill, M. Stovall, D. A. Kuban, R. A. White, and I. I. Rosen, "Out-of-field photon and neutron dose equivalents from step-and-shoot intensity-modulated radiation therapy," *International Journal of Radiation Oncology Biology Physics*, vol. 62, no. 4, pp. 1204–1216, 2005.

[26] S. F. Kry, U. Titt, F. Pönisch, D. Followill, O. N. Vassiliev, R. A. White, R. Mohan, and M. Salehpour, "A Monte Carlo model for calculating out-of-field dose from a Varian 6 MV beam," *International Journal of Medical Physics*, vol. 33, no. 11, pp. 4405–4413, 2006.

[27] S. B. Scarboro, D. S. Followill, and E. al, "Variations in photon energy spectra of a 6 MV beam and their impact on TLD response," *Medical Physics*, vol. 38, no. 5, pp. 2619–2628, 2011.

[28] Australian Institute of Health and Welfare (AIHW), "Cancer in nearly one third of older Australians," Australian Institute of Health and Welfare (AIHW), Canberra, Australia, Tech. Rep., 2005.

[29] F. Vanhavere, E. Carinou, G. Gualdrini, I. Clairand, M. S. Merce, M. Ginjaume, D. Nikodemova, J. Jankowski, J.-M. Bordy, A. Rimpler, S. Wach, P. Martin, L. Struelens, S. Krim, C. Koukorava, P. Ferrari, F. Mariotti, E. Fantuzzi, L. Donadille, C. Itié, R. N., A. Carnicer, M. Fulop, J. Domienik, M. Brodecki, J. Daures, I. Barth, and P. Bilski, *Optimization of Radiation Protection of Medical Staff*, European Radiation Dosimetry Group, Ed., 2012, no. April.

[30] R. E. Shore, K. Neriishi, and E. Nakashima, "Epidemiological Studies of Cataract Risk at Low to Moderate Radiation Doses : (Not) Seeing is Believing," *Radiation Research*, vol. 174, pp. 889–894, 2010.

[31] H. Yan, F. Guo, D. Zhu, S. Stryker, S. Trumpore, K. Roberts, S. Higgins, R. Nath, Z. Chen, and W. Liu, "On the use of bolus for pacemaker dose measurement and reduction in radiation therapy," *Journal of Applied Clinical Medical Physics*, vol. 19, no. 1, pp. 125–131, 2017.

[32] C. Camara, P. Peris-Lopez, and J. E. Tapiador, "Security and privacy issues in implantable medical devices: A comprehensive survey," *Journal of Biomedical Informatics*, vol. 55, pp. 272–289, 2015. [Online]. Available: http://dx.doi.org/10.1016/j.jbi.2015.04.007

[33] J. R. Marbach, M. R. Sontag, and E. al, "Management of radiation oncology patients with implanted cardiac pacemakers: report of AAPM Task Group No. 34." *Medical Physics*, vol. 21, no. 1, pp. 85–90, 1994.

[34] U.S Food and Drug Administration (FDA), "Interference between CT and Electronic Medical Devices," U.S Food and Drug Administration, Silver Spring, Tech. Rep., 2008. [Online]. Available: https://www.fda.gov/radiation-emittingproducts/radiationsafety/electromagneticcompatibilityemc/ucm489704.htm

[35] J. H. Indik, J. R. Gimbel, H. Abe, R. Alkmim-teixeira, U. Birgersdotter-green, G. D. Clarke, T.-m. L. Dickfeld, J. W. Froelich, J. Grant, D. L. Hayes, H. Heidbuchel, S. F. Idriss, E. Kanal, R. Lampert, C. E. Machado, J. M. Mandrola, S. Nazarian, K. K. Patton, M. A. Rozner, R. J. Russo, W.-K. Shen, J. S. Shinbane, W. S. Teo, W. Uribe, A. Verma, B. L. Wilkoff, and P. K. Woodard, "2017 HRS expert consensus statement on magnetic resonance imaging and radiation exposure in patients with cardiovascular implantable electronic devices," Tech. Rep. 7, 2017.

[36] M. Rodriguez, S. Griffin, L. DeWerd, and R. Jeraj, "Characterization of the ADII-33 diamond detector," *Medical Physics*, vol. 34, no. 1, pp. 215–221, 2007.

[37] B. Wang and X. Xu, "Measurements of non-target organ doses using MOSFET dosimeters for selected IMRT and 3D CRT radiation treatment procedures," *Radiation Protection Dosimetry*, vol. 128, no. 3, pp. 336–342, 2008.

[38] A. B. Rosenfeld, "MOSFET dosimetry on modern radiation oncology modalities," *Radiation Protection Dosimetry*, vol. 101, no. 1-4, pp. 393–398, 2002.

[39] M. Buston, P. Yu, T. Cheung, and P. Metcalfe, "Radiochromic film for medical radiation dosimetry," *Materials Science and Engineering*, vol. 41, no. 3, pp. 61–120, 2003.

[40] V. Rudat, A. Nour, A. Alaradi, A. Mohamed, and S. Altuwaijri, "In vivo surface dose measurement using gafchromic film in breast cancer radiotherapy: Comparison of 7-field IMRT, tangential IMRT and tangential 3d-CRT," *Radiation Oncology*, vol. 9, no. 156, pp. 1–9, 2014.

[41] S. Chiu-Taso and M. Chan, "Use of new radiochromic devices for peripheral dose measurement: potential in-vivo dosimetry application," *Biomedical Imaging & Intervention Journal*, no. 5, pp. 1–12, 2009.

[42] F. V. D. Heuvel, G. Defraene, W. Crijns, and R. Bogaerts, "Out-of-field contributions for IMRT and volumetric modulated arc therapy measured using gafchromic films and compared to calculations using a superposition / convolution based treatment planning system," *Radiotherapy and Oncology*, vol. 105, pp. 127–132, 2012.

[43] J. D. Ruben, C. M. Lancaster, P. Jones, and Ryan L. Smith, "A comparison of out-of- field dose and its constituent components for intensity-modulated radiation therapy versus conformal radiation therapy: implications for carcinogenesis." *International Journal Radiation Oncology Biology Physics*, vol. 81, no. 5, pp. 1458–1464, 2011.

[44] I. Das and C. Cheng, "Accelerator beam data commissioning equipment and procedures: report of the TG-106 of the Therapy Physics Committee of the AAPM," *Medical Physics*, vol. 35, no. 9, pp. 4186–4215, 2008.

[45] R. M. Howell, S. B. Scarboro, S. F. Kry, and D. Z. Yaldo, "Accuracy of out-of-field dose calculations by a commercial treatment planning system." *Physics in medicine and biology*, vol. 55, no. 23, pp. 6999–7008, 2010. [Online]. Available: http://www.pubmedcentral.nih.gov/articlerender.fcgi?artid=3152254{\&}tool=pmcentrez{\&}rendertype=abstract

[46] A. Joosten, F. Bochud, S. Baechler, F. Levi, R.-O. Mirimanoff, and R. Moeckli, "Variability of a peripheral dose among various linac geometries for second cancer risk assessment." *Physics in medicine and biology*, vol. 56, pp. 5131–5151, 2011.

[47] A. Joosten, O. Matzinger, W. Jeanneret-Sozzi, F. Bochud, and R. Moeckli, "Evaluation of organ-specific peripheral doses after 2-dimensional, 3-dimensional and hybrid intensity modulated radiation therapy for breast cancer based on Monte Carlo and convolution/superposition algorithms: Implications for

secondary cancer risk asses," *Radiotherapy and Oncology*, vol. 106, no. 1, pp. 33–41, 2013. [Online]. Available: http://dx.doi.org/10.1016/j.radonc.2012.11.012

[48] J. Y. Huang and D. S. Followill, "Accuracy and sources of error of out-of field dose calculations by a commercial treatment planning system for intensity-modulated radiation therapy treatments," *Journal of Applied Clinical Medical Physics*, vol. 14, no. 2, pp. 186–197, 2013.

[49] P. H. Van Der Giessen, "Peridose, a software program to calculate the dose outside the primary beam in radiation therapy," *Radiotherapy and Oncology*, vol. 58, no. 2, pp. 209–213, 2001.

[50] M. Stovall and R. E. Weathers, "Dose reconstruction for therapeutic and diagnostic radiation exposures: use in epidemiological studies," *Radiation Research*, vol. 166, no. 1 Pt 2, pp. 141–157, 2006.

[51] P. J. Taddei, W. Jalbout, R. M. Howell, N. Khater, F. Geara, K. Homann, and W. D. Newhauser, "Analytical model for out-of-field dose in photon craniospinal irradiation." *Physics in medicine and biology*, vol. 58, no. 21, pp. 7463–79, 2013. [Online]. Available: http://www.ncbi.nlm.nih.gov/pubmed/24099782

[52] R. Hughes and R. Prael, "MCNPX-The LAHET/MCNP Code Merger," Los Alamos, NM, Los Alamos National Laboratory, 1997.

[53] Team-X5MC, "MCNP-A General Monte Carlo N Particle Transport Code," Los Alamos, NM, Los Alamos National Laboratory, 2003.

[54] S. Agnostinelli and J. Allison, "Geant4a simulation toolkit," *Nuclear Instruments and Methods in Physics Research Section A: Accelerators, Spectrometers, Detectors and Associated Equipment*, vol. 506, no. 3, pp. 250–303, 2003.

[55] I. Kawrakow, "Accurate condensed history Monte Carlo simulation of electron transport. I. EGSnrc, the new EGS4 version," *Medical Physics*, vol. 27, no. 3, pp. 485–498, 2000.

[56] S. F. Kry, U. Titt, D. Followill, F. Pönisch, O. N. Vassiliev, R. A. White, M. Stovall, and M. Salehpour, "A Monte Carlo model for out-of-field dose calculation from high-energy photon therapy." *Medical physics*, vol. 34, no. 9, pp. 3489–3499, 2007.

[57] B. Bednarz and X. G. Xu, "Monte Carlo modeling of a 6 and 18 MV Varian Clinac medical accelerator for in-field and out-of-field dose calculations : development and validation," *Physics in medicine and biology*, vol. 54, pp. 43–57, 2009.

[58] S. S. Almberg, J. Frengen, and T. Lindmo, "Monte Carlo study of in-field and out-of-field dose distributions from a linear accelerator operating with and without a flattening-filter," *Medical Physics*, vol. 39, no. 8, pp. 5194–5203, 2012.

[59] International Atomic Energy Agency Vienna, *Absorbed Dose Determination in External Beam Radiotherapy*, 2000.

[60] C. P. Ratcliffe and B. Ratcliffe, *Doubt-Free Uncertainty In Measurement An Introduction for Engineers and Students*, 2015.

[61] M. Stovall, S. S. DOnaldson, R. E. Weathers, L. L. Robison, A. C. Mertens, J. F. alck Winther, J. H. Olsen, and J. D. Boice, "GENETIC EFFECTS OF RADIOTHERAPY FOR CHILDHOOD CANCER : GONADAL DOSE RECONSTRUCTION," *International Journal of Radiation Oncology Biology Physics*, vol. 60, no. 2, pp. 542–552, 2004.

[62] R. M. Howell, S. B. Scarboro, P. J. Taddei, S. Krishnan, S. F. Kry, and W. D. Newhauser, "Methodology for determining doses to in-field, out-of-field and par-

tially in-field organs for late effects studies in photon radiotherapy," *Physics in medicine and biology*, vol. 55, no. 23, p. 7009, 2010.

[63] R. M. Howell, M. S. Ferenci, N. E. Hertel, and G. D. Fullerton, "Investigation of secondary neutron dose for 18 MV dynamic MLC IMRT delivery," *Medical physics*, vol. 32, no. 3, pp. 786–793, 2005.

[64] ICRU Report 38, "Dose and volume specification for reporting intracavitary therapy in gynecology," *Journal of the ICRU,*, 1985.

[65] G. Tang, M. A. Earl, and E. al, "Comparing Radiation Treatments Using Intensity Modulated Beams, Multiple Arcs, and Single Arcs," *International Journal of Radiation Oncology Biology Physics*, vol. 76, no. 5, pp. 1554–1562, 2010.

[66] S. MacDonald, S. Ahmad, S. Kachris, B. Vogds, M. DeRouen, A. Gittleman, K. DeWyngaert, and M. Vlachaki, "Intensity modulated radiation therapy versus three-dimensional conformal radiation therapy for the treatment of high grade glioma: a dosimetric comparison." *Journal of Applied Clinical Medical Physics*, vol. 8, no. 2, pp. 47–60, 2007.

[67] M. L. Taylor, L. N. McDermott, P. N. Johnston, M. Haynes, T. Ackerly, T. Kron, and R. D. Franich, "Stereotactic fields shaped with a micro-multileaf collimator: systematic characterization of peripheral dose." *Physics in medicine and biology*, vol. 55, no. 3, pp. 873–881, 2010. [Online]. Available: http://www.ncbi.nlm.nih.gov/pubmed/20071767

[68] K. Kase and X. Mao, "Neutron fluence and energy spectra around the Varian Clinac 2100C/2300C medical accelerator," *Health Physics*, vol. 74, no. 1, pp. 38–47, 1998.

[69] J. D. Ruben, S. Davis, C. Evans, P. Jones, F. Gagliardi, M. Haynes, and A. Hunter, "Second Malignant Tumors THE EFFECT OF INTENSITY-MODULATED RA-

DIOTHERAPY ON RADIATION-INDUCED SECOND MALIGNANCIES," *International Journal of Radiation Oncology Biology Physics*, vol. 70, no. 5, pp. 1530–1536, 2008.

[70] J. Lambert, T. Nakano, S. Law, J. Elsey, D. Mckenzie, and N. Suchowerska, "In vivo dosimeters for HDR brachytherapy: a comparison of a diamond detector, MOSFET, TLD, and scintillation detector," *Medical Physics*, vol. 34, no. 5, pp. 1759–1765, 2007.

[71] A. Wroe, A. Rosenfeld, and R. Schulte, "Out-of-field dose equivalents delivered by proton therapy of prostate cancer," *Medical Physics*, vol. 34, no. 9, pp. 3449–3456, 2007.

[72] C. Lafond and M. Oliver, "Evaluation And Analyze Of Out-of-field Doses In Head and Neck Radiation Therapy For Different Delivery Techniques: From 3DCRT To VMAT," *International Journal of Radiation Oncology Biology Physics*, vol. 81, no. 2, p. S907, 2011.

[73] P. Metcalfe, T. Kron, and P. Hoban, *The Physics of Radiotherapy X-rays and Electrons*. Madison, Wisconsin: Medical Physics Publishing, 2007.

[74] S. Gotoh, Y. Kawaharada, S. Suda, and M. Uetani, "Peripheral Organ Dose Evaluation using a Human Body Phantom in Intensity Modulated Radiation Therapy for Lung Cancer with Helical Type Accelerator," *Acta Medica Nagasakiensia*, vol. 55, no. 2, pp. 61–67, 2011.